

Electron Pulses probing Plasma Dynamics and aligned Molecules

Peter Reckenthäler



München, den 4. September 2009

Electron Pulses probing Plasma Dynamics and aligned Molecules

Dissertation
an der Fakultät für Physik
der Ludwig-Maximilians-Universität in München

von

Peter Reckenthäler
aus Trier

München, den 4. September 2009

Erstgutachter: Prof. Dr. Ferenc Krausz
Zweitgutachter: Prof. Dr. Eberhard Riedle
Tag der mündlichen Prüfung: 29. Oktober 2009

Zusammenfassung

Aufgrund ihrer kleinen De-Broglie-Wellenlänge sind Elektronen sehr gut für die Strukturanalyse mit einer Auflösung im atomaren Bereich geeignet. Die Synchronisation von ultrakurzen Elektronenpulsen mit ultrakurzen Laserpulsen bietet weiterhin die Möglichkeit, Vorgänge wie Konformationsänderungen von Molekülen oder Phasenübergänge in Festkörpern mit präziser Orts- und Zeitauflösung zu untersuchen. Zusätzlich reagieren Elektronen aufgrund ihrer Ladung hochsensitiv auf elektrische und magnetische Felder.

In den in dieser Arbeit vorgestellten Experimenten werden beide Eigenschaften ausgenutzt. Ihre Eigenschaft, auf äußere Felder zu reagieren, wird zur Untersuchung ultraschneller Plasmadynamik verwendet. Diese Art der Untersuchung ermöglicht es, Plasmaeigenschaften zu beleuchten, die anderen Methoden nicht zugänglich sind.

Die extrem hohe räumliche Auflösung, kombiniert mit einer Zeitauflösung von einigen Pikosekunden, ermöglicht die erste Demonstration zeitaufgelöster Elektronenbeugung von transient ausgerichteten Molekülen. Dabei wird der ultraschnelle Zerfall des erzeugten Rotationswellenpakets gemessen. Zeitaufgelöste Elektronenbeugung an ausgerichteten Molekülen stellt einen bedeutenden Schritt auf dem Weg hin zu dreidimensionaler Strukturaufklärung hochkomplexer Moleküle dar.

Die Raumladung innerhalb der Elektronenpulse führt zur schnellen zeitlichen Verbreiterung der Pulse, typischerweise in den Pikosekundenbereich. Um diese Einschränkung zu überwinden, wurde eine Einzelelektronenquelle konstruiert. Erste zeitaufgelöste Experimente zum Photoemissionsprozess zeigen eine verbesserte Zeitauflösung von einigen hundert Femtosekunden.

Abstract

Ultrashort electron pulses are very attractive for the investigation of dynamics with ultrahigh spatial and temporal resolution. Due to their small de Broglie wavelength they allow for atomic-scale resolution in diffraction experiments. Synchronized with ultrashort laser pulses, they can probe ultrafast processes such as conformational changes in molecules or phase transitions in solids. In addition, being charged particles, they are a very sensitive probe for electric and magnetic fields.

In this thesis, both features are used. Taking advantage of the ability to probe electric and magnetic fields, the ultrafast dynamics of optical-field-ionized (OFI) plasmas are investigated with picosecond resolution. New features of OFI-plasmas are observed which are not accessible to other methods such as a cloud of electrons separating from the plasma core far beyond the Debye length.

Using the ultrahigh spatial resolution combined with picosecond temporal resolution, transient molecular alignment is observed for the first time using time-resolved electron diffraction. Diiodotetrafluoroethane ($C_2F_4I_2$) molecules are aligned selectively using an optically induced dissociation reaction. The ultrafast dephasing of the alignment is measured with few-picosecond resolution. Electron diffraction from aligned molecules opens a way for three dimensional structure determination of complex molecules.

Due to the Coulomb-repulsion electron pulses broaden in time and therefore producing femtosecond pulses remains a challenge. To overcome this limitation, an electron-source using single-electron pulses was constructed. Experiments capturing images of an electron cloud photo-emitted from a surface are presented. The achieved femtosecond resolution allows to study the development of cloud expansion and velocity spread within dense electron packets from surfaces.

Contents

Zusammenfassung	vii
Abstract	ix
Contents	ix
1 Introduction	1
1.1 Summary	5
2 Molecular structure and dynamics	9
3 Real-time observation of optical-field-ionized plasmas	13
3.1 Introduction	13
3.2 OFI-plasma in gas jets	14
3.2.1 Experimental setup	14
3.2.2 Experimental results	16
3.2.3 Theoretical description	19
3.2.4 Numerical simulation	23
3.3 Low density OFI-plasma	26
3.3.1 Experimental results	26
3.3.2 Theoretical description	28
3.3.3 Numerical simulation	29
3.4 Limitations	30
3.5 Conclusions	32
	ix

4	Time-resolved electron diffraction from selectively aligned molecules	34
4.1	Introduction	34
4.2	Theoretical basics for static and time-resolved electron diffraction .	37
4.2.1	Static gas-electron-diffraction (GED)	37
4.2.2	Time-resolved gas-electron-diffraction	40
4.3	Experimental methods	41
4.3.1	Experimental setup	41
4.3.2	Calculation of the alignment decay time	44
4.4	Experimental results	44
4.4.1	Static electron diffraction	44
4.4.2	Time-resolved electron diffraction	47
4.4.3	Time-resolved observation of transient alignment	49
4.5	Conclusions	53
5	Single-electron source – from picoseconds to femtoseconds	55
5.1	Proposed method for measuring the duration of electron pulses	56
5.1.1	Theoretical basics	57
5.1.2	Proposed experiment	59
5.1.3	Numerical results	60
5.1.4	Experimental considerations	62
5.2	The MHz-electron source	63
5.3	Time-resolved visualization of photoemission from a solid	64
5.3.1	Experimental setup	65
5.3.2	Experimental results	69
5.4	Conclusions	70
6	Conclusions and outlook	72
A	Chamber for MHz-experiments	76
B	Diffraction patterns	78
	Bibliography	80
	Danksagung	95

Curriculum Vitae

97

1. Introduction

Due to the short de Broglie wavelength of electrons, electron diffraction is a very successful technique for the determination of static structures ranging from the structures of isolated molecules to structures of solids. However, for a full description of dynamical processes such as chemical reactions or phase transitions, real-time investigation of the underlying elementary processes is necessary.

The microscopic steps of chemical or biological transformations are on the femtosecond ($1 \text{ fs} = 10^{-15} \text{ s}$) time-scale and above. Tens to hundreds of femtoseconds are the time-scale of molecular vibrations which is the natural scale for making or breaking of chemical bonds. This is consistent with the millielectronvolt-scale spacing of molecular vibrational energy levels. The typical time-scale for electronic motion is the attosecond ($1 \text{ as} = 10^{-18} \text{ s}$) regime, while faster processes in the zeptosecond ($1 \text{ zs} = 10^{-21} \text{ s}$) regime are predicted to occur within nuclei [1].

With the development of femtosecond laser systems in the past decades (for a review see [2]) ultrashort laser pulses enabled the time-resolved study of ultrafast molecular dynamics on the natural time scale of their vibrations. In 1999 Ahmed H. Zewail was awarded the nobel prize in Chemistry for pioneering this field called “Femtochemistry” [3].

The advance of attosecond physics [1] improved the time-resolution to the time regime of electronic dynamics. Pulses shorter than 100 attoseconds have been demonstrated [4]. Attosecond time resolution enabled the real-time observation of electronic processes, e.g. in atoms [5] and solids [6]. With attosecond pulses it was possible to directly measure the light-field of a few-cycle laser pulse [7] and to reconstruct the charge distribution in a diatomic molecule [8].

However, the relation between the spectroscopic observables and structure is only easily understood for small systems of not more than a few atoms, but it becomes

more difficult or even unsolvable for more complex systems. By replacing the interrogating laser pulse with an ultrashort electron pulse, the sub-Angstrom spatial resolution of electron diffraction can be combined with ultrahigh time-resolution. Ultrafast electron diffraction, crystallography and microscopy have been very successful in the investigation of the time-resolved structures of isolated molecules, materials and biological systems [9].

The investigation of isolated molecules in the gas phase with gas electron diffraction (GED) is, however, still hampered by the random orientation of the molecules. This leads to diffraction rings as opposed to the Bragg-spots which are obtained by diffraction from single crystals. Because of this “smearing”, only one-dimensional information can be retrieved from such diffraction patterns, i.e. the bond distances of the molecules of interest. The bond angles cannot directly be extracted from the experimental diffraction patterns. A further complication comes from the fact that lighter atoms scatter less than heavier atoms. This can lead to incomplete structures being obtained because of the uncertainty in the positions of the light atoms such as hydrogen. Also, molecular vibration adds a complication: The average interatomic distances can depend on the vibrational amplitudes. Due to bending the distances may appear smaller; this is known as the shrinkage effect [10]. The effect gets more severe if the molecules are bigger and have low-frequency/large-amplitude torsion angles. Molecular structure analysis with electron diffraction in the gas phase usually is a combination of theoretical modeling and experiment. An example is the SARACEN-method (Structure Analysis Restrained by Ab initio Calculations for Electron diffraction, [11]): Ab initio calculations are used to generate a theoretical model for the molecule in question, which is refined by the experimental diffraction pattern. This combination of theory and experiment becomes more difficult with growing molecular size. Structure determination using GED is therefore limited to rather small molecules up to a few tens of atoms. The structure determination of the phosphinyl radical $\dot{P}R_2$ [$R = CH(SiMe_3)_2$] (57 atoms) [12] is an example of one of the biggest structures determined with GED.

In the case of ultrafast electron diffraction (UED [9]) the situation is even more challenging. Because of the Coulomb repulsion of the electrons within the electron pulse (“space-charge”) the number of electrons per pulse has to be kept small to achieve short pulses which are required for a high temporal resolution. With ~ 1000 electrons per pulse, the electron pulse duration is ~ 1 ps [9]. Therefore, the electron

flux is lower as compared to the continuous GED machines. This limitation of the electron flux reduces the range of accessible scattering angles in the diffraction experiment which again limits the spatial resolution.

The limitations of electron diffraction in the gas phase due to the random molecular orientations can be overcome by aligning the molecules. It has been shown theoretically that electron diffraction from aligned molecules reveals not only the interatomic distances but also the bond angles [13, 14]. Molecules can be aligned using ultrashort laser pulses actively [15] or selectively through a dissociation reaction [13]. Both alignment techniques provide samples of transiently aligned molecules which are free from external fields. The molecules can be observed free from external perturbations.

Electron diffraction from transiently aligned molecules requires the electron pulses to be short enough to capture the diffraction pattern while the molecules are aligned. Due to the molecular rotations the alignment vanishes while the molecules continue to rotate randomly. This rotational dephasing of the corresponding rotational wavepacket happens in approximately one picosecond for heavy diatomic molecules like I_2 and in about 200 fs for light diatomic molecules like N_2 ¹

Approaches to shorten electron pulses to the femtosecond regime include using a very short electron source to reduce space-charge induced broadening [19] or eliminating space-charge using single-electron pulses at MHz repetition rate [20]. However, femtosecond resolution has up to now only been achieved in solid state experiments [21, 22], while gas phase experiments are still limited to the picosecond regime [9]. With femtosecond temporal resolution electron diffraction from transiently aligned molecules could allow for three dimensional structure reconstruction even for molecules of high complexity. Additionally, photochemical reactions, as for example the ring opening reaction of 1,3-cyclohexadiene, which has been studied using UED with picosecond resolution [23], could be resolved in much more detail.

The electron charge is a challenge on the way to produce femtosecond electron pulses. However, on the other hand it opens the way for a different use of ultrashort electron pulses: Electrons are an ideal probe for electric and magnetic fields. An

¹The dephasing in the case of selective alignment can be approximated by an exponential decay [16]. Using the rotational constant B , the dephasing time t_d can be calculated according to $t_d = 1/\sqrt{36\pi k_B \tau_{rot} cB/\hbar}$, where k_B is the Boltzmann constant, τ_{rot} the rotational temperature and c the speed of light. The rotational constants are $B = 0.037 \text{ cm}^{-1}$ for I_2 [17] and $B = 1.989 \text{ cm}^{-1}$ for N_2 [18].

interesting subject to study with this tool are optical-field-ionized (OFI) plasmas. OFI plasmas are just in the boundary area between atomic or molecular physics where quantum effects play the major role and plasma physics where electrons are free and quantum effects are less important [24]. With optical-field ionization, atoms or molecules are ionized by a laser field, and the plasma electrons respond nearly classically to the force exerted by the electric field [24]. Studying OFI-plasmas in detail can provide knowledge to help improving the setting of parameters for optimizing particular applications. Examples are X-ray lasers and soft X-ray sources as well as plasma electron and ion accelerators.

In the course of this thesis a series of ultrafast experiments is presented which make use of the short electron wavelength as well as of the electron charge. Taking advantage of the sensitivity of electrons to electromagnetic fields, OFI-plasmas are investigated with picosecond temporal resolution. Originally these experiments were aimed at finding the spatio-temporal overlap of electron and laser pulses in UED-experiments. However, they turned out to be a new method, viz. deflectometry, which is capable of capturing images of the ultrafast evolution of the OFI-plasmas. For this purpose, a kHz electron source was constructed based on a commercial kHz fs-laser system. Using this kHz-electron source an expanding cloud of hot plasma electrons is observed leaving the positive core of ions traveling far beyond the Debye length. Time-varying magnetic fields deflect electrons creating moving lobes along the laser line. The method can have important implications being applied to improve parameters for many applications of OFI-plasmas.

Based on this kHz-electron source, an ultrafast electron diffraction (UED) apparatus was developed which allows for the time-resolved investigation of photochemical reactions with Angstrom spatial and picosecond temporal resolution. Using this UED-system the two-step dissociation reaction of 1,2-diodotetrafluoroethane ($C_2F_4I_2$) was investigated. The main success of this experiment is the first demonstration of transient molecular alignment with UED. The alignment decay was followed with picosecond temporal resolution. These experiments may open a route for a new way of structure determination of complex isolated molecules.

The main limitation of the UED-experiment from aligned molecules is the temporal resolution of picoseconds, which is comparable to state-of-the-art gas phase studies [9]. Within a few picoseconds the alignment gets lost due to molecular rotations. Shorter electron pulses are necessary to improve the temporal resolution

and to observe the alignment closer to the optimum. To shorten the electron pulse duration to the femtosecond regime, an ultrahigh vacuum chamber was designed and constructed. The ultrahigh vacuum system allows to apply very high acceleration fields which are required to produce short electron pulses (see chapter 5 for more detail). The electron source housed in this chamber is based on a long cavity MHz oscillator [25]. In this system it is possible to overcome space-charge limitations by using single-electron pulses allowing for a significant improvement in time-resolution.

To measure the duration of these ultrashort electron pulses and prove the femtosecond resolution, a very general method for pulse duration measurement is presented theoretically. The experiments making use of the MHz electron source are aimed to demonstrate this method experimentally. First experiments are carried out which already show femtosecond resolution. In these experiments the high temporal resolution allows to investigate the photo emission process of electrons from a copper surface. The cloud expansion of the photo-emitted electrons is followed with a temporal resolution below 400 fs. In addition, these experiments constitute a feasible method to establish the spatio-temporal overlap of the electron and laser pulses in pump-probe experiments even for laser pulses of pulse energy below 100 nJ.

1.1. Summary

The thesis is structured according to the following scheme:

Chapter 2: This chapter gives an overview summarizing experimental techniques for the study of molecular structure and dynamics. Important spectroscopic methods are addressed. The chapter discusses the differences between spectroscopic and diffractive methods and emphasizes the wide applicability of ultrashort electron pulses.

Chapter 3: This chapter focuses on the application of ultrashort electron pulses in deflectometry. Even though the experiments were first aimed only to find the temporal and spatial overlap of the fundamental laser pulses and the electron pulses they turned out to be additionally a new method to visualize and follow the evolution of OFI-plasmas.

Images of the plasma evolution are taken with picosecond time steps. By this method new features of OFI-plasmas have been discovered, which have not been seen before. The results of this chapter are published in [26, 27]. These experiments were carried out at the Max-Planck-Institut für Quantenoptik. The use of the laser system was kindly provided by the group of Prof. Dr. Kompa. It is a commercial kHz titanium-sapphire laser system which allowed for the construction of a picosecond electron source.

Chapter 4: The goal of the experiments presented in this chapter is to carry out time-resolved diffraction experiments which for the first time show transient molecular alignment using the method of selective alignment. The results of this chapter are published in [28]. The experiments were carried out using the same apparatus as used for the OFI-plasma experiments. However, the setup had to be substantially modified: To establish a gas jet containing rotationally cool molecules a seeding setup was built. To be able to study photoinduced molecular reactions the fundamental pulses were converted into the 3rd-harmonic. To record diffraction patterns the main electron beam has to be blocked and for this purpose a movable beam block had to be constructed.

Chapter 5: To record sufficient signal in time-resolved diffraction experiments using kHz systems usually thousands of electrons per pulse have to be used. Therefore time resolution is limited to the picosecond regime due to repulsion of the pulse electrons. The theory and the experiments presented in Chapter 5 are based on a MHz-laser system allowing for single-electron experiments which promise to have femtosecond time-resolution. In the first part of this chapter a very general method for the measurement of electron pulse durations is proposed and analyzed theoretically. In the second part, first experimental results are presented. These experiments were carried out at the physics department of the Ludwig-Maximilians-Universität in Garching, making use of a MHz-laser system built by S. Naumov [25]. With these femtosecond electron pulses it is possible to visualize pho-

toemission of electrons from a surface with femtosecond resolution even with the relatively weak laser pulses. The theoretical results are published in [29] and the experimental results are summarized in [30].

Chapter 6: The last chapter is a summary of the results presented in this thesis and contains an outlook on future prospects.

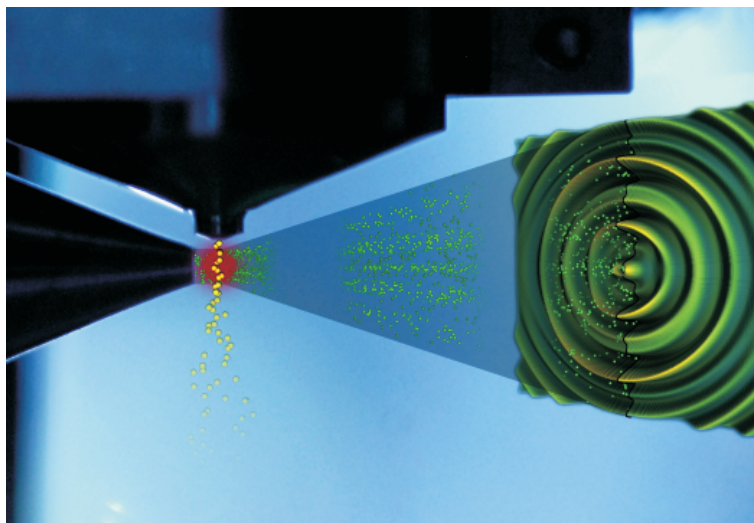


Figure 1.1.: Artist's view into the vacuum chamber housing the experiments on time-resolved electron diffraction: Ultrashort electron pulses (electrons symbolized as green balls) emerging from a small orifice to the left impinge on a molecular gas jet. The jet streams out of a nozzle (gas molecules symbolized as yellow balls). The electrons are scattered from the gas molecules and generate a diffraction image on the detector (schematically displayed in the right part of the picture, rotated towards the observer for better visualization). In the region where the electron pulses and gas jet overlap the UV laser (invisible in reality) is illustrated as a red circular spot. (Photo: Thorsten Naeser; layout: Christian Hackenberger; image taken from MPQ webpage.)

2. Molecular structure and dynamics

The understanding of molecular structure and dynamics is fundamental for the investigation of physical, chemical and biological processes. Molecular energy levels can be determined by measuring absorption or emission of electromagnetic radiation. The intensities of the absorption or emission lines give the probabilities of the transitions and thus information about the symmetry of the energy states and their couplings. The linewidths are correlated with the state lifetimes and with time-resolved measurements molecular dynamics can be investigated.

Spectroscopic techniques cover a large range of the electromagnetic spectrum from Microwave radiation to the hard X-ray regime [31]. Radiation with an energy of only a few meV can be used to induce nuclear spin transitions in Nuclear-magnetic-resonance (NMR) spectroscopy. NMR-spectroscopy is a powerful tool for the determination of large molecular structures of biological interest such as proteins [32] and for medical imaging [33, 34]. Increasing the frequency to the microwave and IR range allows for excitation of molecular rotations and vibrations. To be directly excited by electromagnetic radiation, these transitions require the molecules to have a dipole moment. In the case of missing dipole moments the complementary Raman scattering techniques are used to study rotations and vibrations. The spectroscopic resolution is limited by the width of the absorption or emission lines. At room temperature the line width is usually dominated by the Doppler effect. Several nonlinear methods exist to improve the spectroscopic resolution to the natural width of the lines e.g. Doppler-free cw two-photon spectroscopy [35].

In the visible and the ultra violet range the photon energy is high enough for electronic excitation. When molecules absorb photons with wavelengths ranging from the visible to the ultraviolet, they may undergo electronic transitions redistributing the valence electrons and turning them into excited state molecules. The

excited states are unstable. The redistribution of the energy in the molecule can lead to conformational changes and dissociation.

Increasing the photon energy further, molecules can be ionized (e.g. for water in gas phase if the photon energy exceeds 13 eV [36]). At keV photon energies in the hard X-ray regime, ionization of the inner shell electrons is possible and the excited ions relax through fluorescence or Auger decays to ionic states.

A spectroscopic method using X-rays, is X-ray absorption spectroscopy (XAS). For reviews see [37, 38]. Plotting the X-ray absorption coefficient as a function of the energy, the dominant features are the absorption edges. At certain energies the absorption increases in a step-like manner. These features are unique to a given atom and reflect the excitation energy of inner-shell electrons. Just above the edges, the absorption is modulated by oscillatory structures. Within the first 30 eV - 50 eV the spectrum is dominated by multiple scattering of the ionized photoelectron by its nearest neighbors. This region is termed XANES (X-ray absorption near-edge structure). It contains information about both the electronic and the geometrical structure including bond distances and angles. For higher energies mainly single scattering events dominate, resulting in a weaker oscillatory modulation of the absorption. This region is called EXAFS (extended X-ray absorption fine structure). The EXAFS-region provides information about internuclear distances of the nearest neighbors from the absorbing central atom.

For X-ray radiation elastic scattering enables the use of diffraction techniques to directly probe the atom positions. X-ray diffraction from molecular crystals is the dominant method for the structure determination of large molecules relevant in biology. Famous examples are the determination of the DNA structure [39, 40], the Myoglobin molecule [41] and the Haemoglobin molecule [42]. Today, the majority of the small fraction of those protein structures which are known, is determined by X-ray diffraction. At the end of July 2009 the number is 50864 out of 59227 known protein structures [43]. Due to the large scattering cross section of electrons and atoms and the more favorable ratio of elastic to inelastic scattering cross sections as compared to X-rays [44], electron diffraction has been very successful in determining the structures of isolated molecules in the gas phase [45].

Molecular dynamics can be investigated with ultrashort laser pulses. In the pump-probe scheme, a femtosecond laser pulse (pump-pulse) excites a coherent wavepacket. A weaker pulse (probe-pulse) probes the optical response as a function

of the delay between pump-pulses and probe-pulses. The coherence in the excited levels leads to dynamics which can be directly associated with classical motion [46]. The excited system can be probed e.g. by spectroscopy or mass spectroscopy.

To actually follow a chemical reaction detecting also the intermediate states, femtosecond resolution is required [3]. Observing the passage through the molecular transition state was for the first time demonstrated for the dissociation reaction of ICN [47]. This experiment was one of the first in the field of “Femtochemistry” [48]. Time resolved experiments with femtosecond resolution have been performed within the spectral range from the far infrared to the deep ultraviolet. The recent developments in the field of attosecond physics [1] give the tools to study electronic processes in molecules with sub-femtosecond resolution.

For complex molecular systems, structural information about all nuclear coordinates at a given time can be only revealed by diffraction methods using X-rays or electrons. High flux X-Ray pulses (10^3 to 10^6 photons) have been used with a time resolution of about 100 ps, while the now available femtosecond sources offer significantly lower numbers of photons per pulse (10 to 100 photons) [49]. Therefore, to date most X-Ray diffraction studies have been on solids investigating lattice dynamics, phase transitions and melting [49].

In contrast, in the gas phase, ultrafast electron diffraction (UED) has been very successful in following chemical reactions on a picosecond time-scale [9]. Unlike spectroscopic probe-pulses, the electron pulses are sensitive to all species in their pass and can see structures which are not accessible to spectroscopy. An example which demonstrates the ability of electron pulses to capture the structure of intermediates during a chemical reaction is the two-step dissociation reaction of $C_2F_4I_2$ forming tetrafluoroethylene C_2F_4 . With UED it has been possible to determine the structure of the intermediate C_2F_4I -radical [23, 50].

A new approach for structure determination has been proposed which relies on ultrashort X-ray pulses originating from free-electron X-ray lasers (FEL) [51]. This method aims at three dimensional imaging of large biomolecules. The idea is to take a diffraction image of the single molecule in a single shot making use of the large number of X-ray photons in an FEL-pulse. The pulse is required to be short enough to capture the diffraction image before the molecule is destroyed by Coulomb explosion. Images of molecules which are accidentally aligned are selected by means of a specialized algorithm [52]. Evaluation of images for different angles allows for

the three dimensional reconstruction of the molecule.

In summary, X-ray and electron diffraction offer direct access to structure of physical systems with atomic resolution. Time-resolved electron diffraction is a very powerful technique to study ultrafast molecular processes in the gas phase. The main limitations of ultrafast gas-electron diffraction, the random molecular orientation and the temporal resolution are subjects of this thesis.

3. Real-time observation of optical-field-ionized plasmas

The experiments presented in this chapter are dedicated to the time-resolved investigation of optical-field-ionized (OFI) plasmas. Due to their charge, electrons are sensitive to the electric and magnetic plasma fields. With pump-probe experiments the ultrafast evolution of the plasma fields is investigated with picosecond resolution. This method has been called “electron deflectometry” [26]. The results comprise information which is not accessible to other techniques. Images of a positively charged core of ions and a cloud of electrons expanding farther than expected are recorded.

3.1. Introduction

OFI plasmas are of great interest owing to their unique properties and suit many applications such as the study of nuclear fusion [53], generation of energetic electrons [54, 55, 56, 57] and ions [58, 59], X-ray emission [60, 61], X-ray lasers [62, 63, 64] and XUV attosecond pulse generation [65]. A detailed knowledge of the plasma dynamics can be crucial for optimizing a given application.

The parameters of an OFI plasma can be varied over a wide range: The maximum ionization stage can be set by the intensity of the laser pulse generating the plasma [66], the electron temperature can be controlled by applying linear or circular polarization [67], and by appropriately choosing the backing pressure of the nozzle one can generate cluster plasmas [68]. Various methods have been applied to investigate the parameters of OFI plasmas. The electron temperature has been measured by Thomson scattering [69]. The ionization stage has been determined by

ion spectrometry [70] and by recording the emission of X-rays from the plasma [63]. The time-resolved plasma density profile has been measured by optical interferometry and holography [71, 72]. Moiré deflectometry has been used to determine the density profile in the plasma channel and its lateral expansion [73]. Spectrometry of ions emitted from the plasma has yielded information on the ion velocity and temperature [74]. Radiography using energetic (MeV) protons has been used to diagnose density perturbations and transient fields in high-density plasmas with a temporal resolution of 100 ps [75, 76, 77].

Electron deflectometry makes use of the deflection of charged electrons by the plasma fields. Monoenergetic electrons with an energy of 20 keV are directed onto an OFI nitrogen plasma generated by a 50 fs titanium-sapphire laser pulse. The electrons are deflected by the fields resulting from charge separation, and the resulting distortion of the electron beam yields time-resolved images of the plasma. Pump-probe experiments of the plasma evolution capture changes within a few picoseconds with a spatial resolution of 30 μm . This direct time-resolved imaging of plasma fields reveals features which cannot be observed using methods. Such knowledge can help improving parameters for optimizing particular applications. As an example, X-ray lasers and soft X-ray sources may greatly benefit from a better understanding of the dynamics of laser-generated plasmas. The new technique has the potential to lead to better control of plasma electron- and ion accelerators and improve their features. The high sensitivity of electron deflectometry is due to the fact that even small charge imbalances within the plasma are observable as distortions in the spatial profile of the electron beam. The narrow energy spread and low emittance ($\varepsilon = 1.5 \text{ mRad mm}$) of the electron beam allows for the detection of plasma fields below 10^6 V/m .

3.2. OFI-plasma in gas jets

3.2.1. Experimental setup

The experimental setup is sketched in fig. 3.1. The vacuum system consists of two chambers, the acceleration chamber and the experiment chamber. Without the gas jet the pressure is typically on the order of 10^{-5} mbar. The linearly polarized laser pulses have a central wavelength of 800 nm, a temporal full-width-half-maximum

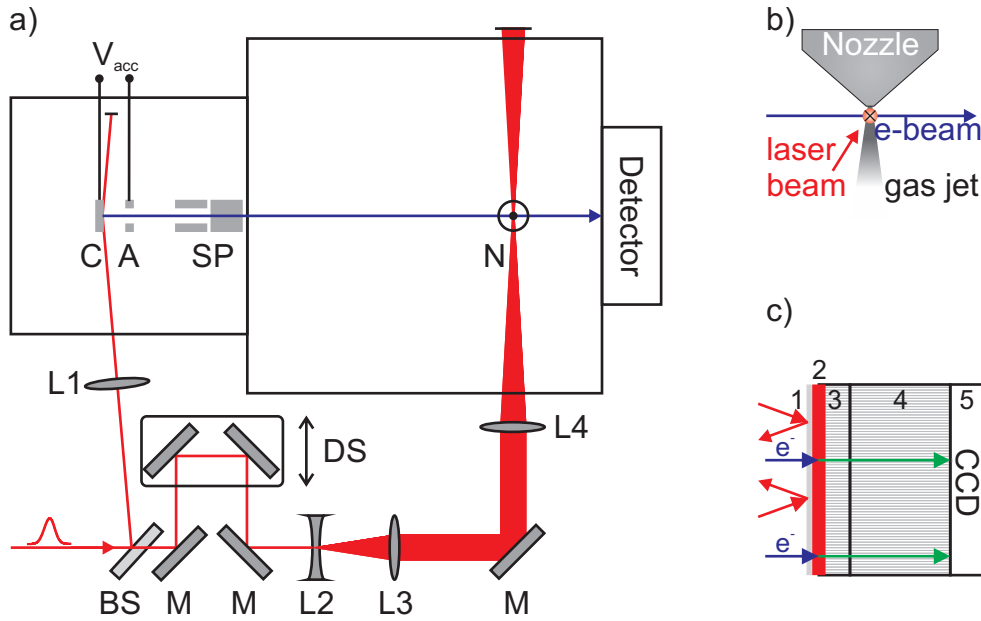


Figure 3.1.: a) Experimental setup: BS: beam splitter; L1: lens ($f = 300$ mm); C: copper cathode; A: copper anode; V_{acc} : acceleration voltage (20 kV); SP: steering plates; N: gas nozzle; Detector: see part c); M: dielectric mirrors reflective for 800 nm; L2: defocusing lens ($f = -100$ mm); L3: focusing lens ($f = 400$ mm); L4: focusing lens ($f = 300$ mm). b) Side view of the experimental geometry. c) Detector: 1: aluminium coating (100 nm); 2: phosphor layer; 3: fiber disk; 4: fiber tube; 5: CCD-chip.

(FWHM) of 50 fs, a repetition rate of 1 kHz and an energy of 1.8 mJ. A small fraction of the laser light is split from the main beam and focused onto the surface of a copper cathode inside the acceleration chamber. Electron pulses are created from the surface via a three-photon photoelectric effect (the photon energy of 1.55 eV is below the work function of copper). The resulting electron pulses are then accelerated by a static voltage of 20 kV over a distance of 11 mm. The direction of the electron pulses is controlled using two pairs of steering plates. The steering plates deflect the electron beam by an adjustable static electric voltage (few hundreds of volts) in the two directions perpendicular to the electron beam path. Traversing a nitrogen gas jet the electron pulses are directed onto the detector (fig. 3.1 b)).

The electron beam is detected by means of a phosphor-coated fiber plate which is fiber coupled to a CCD chip (fig. 3.1 c)). Residual laser light (mainly scattered from

the anode or from the gas nozzle) is rejected by a 100 nm aluminium layer on the phosphor coating. The divergence of the electron beam results in a magnification factor of 1.6. By evaluating the shadow of a sharp edge, the spatial resolution of the imaging system is estimated to be 30 μm .

The electron pulse duration depends on the number of electrons per pulse and the initial energy spread of the electrons at the instant of emission from the photocathode. In the present experiment the pulse duration is mainly determined by the number of electrons per pulse (this can be confirmed using the GPT-code [78], a well-established simulation tool for particle propagation). To determine this number, the electron beam current is measured by means of a Faraday cup coupled to a pico-amperemeter. With this current the number of counts on the detector is calibrated to the number of electrons per pulse. The electron current can be controlled by adjusting the intensity of the laser beam on the cathode.

The main part of the laser beam is expanded and then focused with a 300 mm lens into a nitrogen gas jet to a spot 20 μm in diameter, resulting in a peak intensity of 4×10^{15} W/cm². At the point of plasma generation the gas jet has a density of 2.4×10^{17} /cm³ as measured by evaluating the reduction in electron beam intensity after traversing the jet. The distance between the photocathode and the gas jet is 250 mm and the distance between gas jet and phosphor screen is 60 mm. The temporal delay between the pump laser and electron pulses is adjusted by means of a motorized delay stage.

3.2.2. Experimental results

Figure 3.2 shows pump-probe images of the plasma evolution of a nitrogen OFI-plasma. The images show a global time-scan ranging over about 170 ps. For each image, 1000 electron pulses containing 65000 electrons per pulse are acquired. The corresponding pulse duration is calculated with the GPT-code [78] to 15 ps. An image of the electron beam without the laser beam is used to correct a gradient in the intensity of the electron beam. A background image without the electron beam was used to subtract the residual scattered laser light (mainly light penetrating defects in the aluminium coating).

Initially, a small depleted region appears in the electron beam in the area of the laser focus. This “hole” expands for approximately 80 ps. Then a spot develops

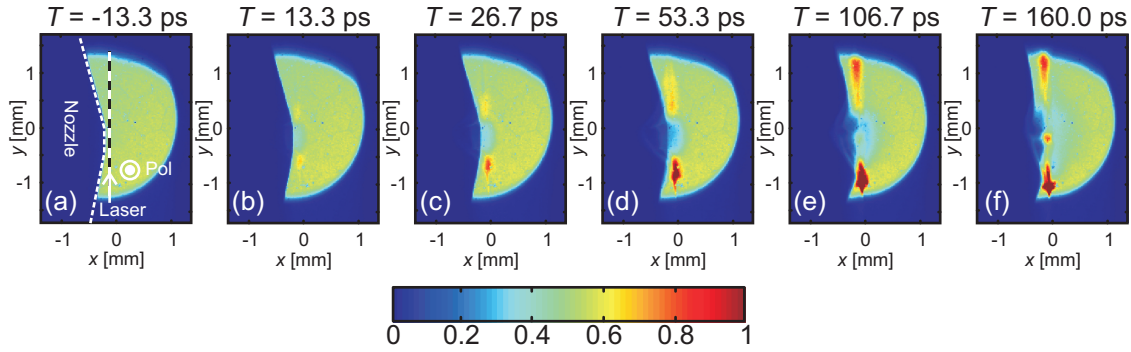


Figure 3.2.: Pump-probe images of the plasma evolution. a)-f) Changes in the electron beam due to the charge distribution in the plasma as a function of the time delay T between the electron and laser pulses. The x - and y - scales of the panels are those of the detector. The dark area in the left part of the images is the shadow of the gas nozzle. The geometry is included as an overlay in part a). The laser is incident from below with a polarization perpendicular to the image plane. The width of the black and white dashed line in panel a) corresponds to the maximum width of the laser beam while traversing the electron beam, and the position of the line corresponds to the path of the laser. The color mapping represents the number of electron counts normalized to the maximum.

in the center (fig. 3.2 e)-f)). The spot becomes brighter than the initial electron beam for a time delay $T > 100$ ps, and its intensity increases up to 200 ps. For later times (not shown in the figure) the brightness of the spot slowly decreases. Simultaneously with the depleted region, two bright “lobes” appear on each side of the plasma region, along the line of laser propagation (vertical in fig. 3.2 and fig. 3.3). These lobes then move away from the focal region in opposite directions. The side-lobes reach the boundary of the electron beam after approximately 100 ps (fig. 3.2 e)) and then remain static. The pattern remained qualitatively unchanged until the maximum delay time in the experiment ($T = 300$ ps), with only a slight decrease in the brightness of the main features.

Figure 3.3 focuses on the initial stages of the plasma expansion. Here the duration of the electron pulses was decreased by reducing the number of electrons per pulse. For the images 3000 electron pulses with 2300 electrons each are recorded. The corresponding pulse duration is calculated using the GPT-code to 2.6 ps. fig. 3.3 a)-d) shows the plasma evolution with a time step of 2.7 ps. The formation of

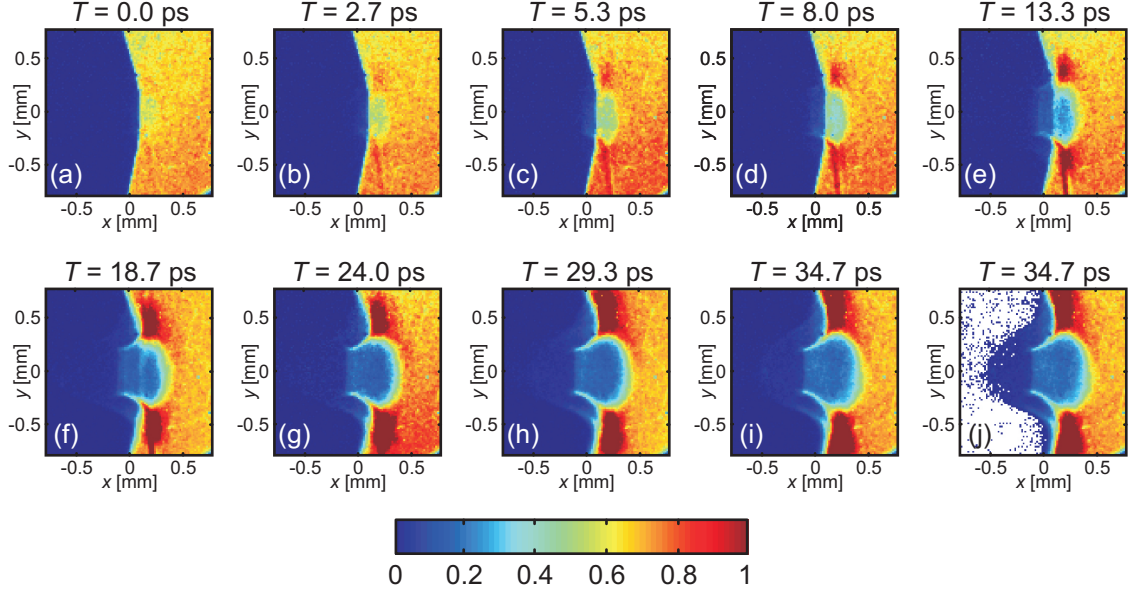


Figure 3.3.: a)-i) Pump-probe images of the plasma evolution with increasing temporal resolution. j), Image for the same time delay ($T = 34.7$ ps) as in i), with the color corresponding to the lowest number of counts (dark blue) removed to highlight the pattern of deflected electrons. The geometry is the same as shown in fig. 3.2 a). The x - and y - scales of the panels are those of the detector. The color mapping represents the number of electron counts normalized to the maximum.

an expanding feature is clearly visible after the first time step. After only 5.3 ps (fig. 3.3c)) there is already a well-defined boundary and deflected electrons appear in the shadow of the nozzle. For $T > 5.3$ ps (fig. 3.3 d)-i)) the hole expands and the number of electrons deflected out of the focal region increases. The side-lobes at the boundary of the plasma appear at 5.3 ps (fig. 3.3 c)), then increase in brightness and move away from the center. At $T = 24$ ps (fig. 3.3 g)) the fraction of electrons deflected reaches its maximum of 80 % and additional deflected electrons are observed in the shadow of the nozzle, with a maximum deflection angle of 8 mrad. Figure 3.3 j) shows the pattern at 34.7 ps with the background color (dark blue) removed to highlight the deflected electrons. Note the sharp boundary on the right side of the plasma, which at 24 ps (fig. 3.3 g)) has a width of about 0.2 mm. For $T > 70$ ps (not shown in fig. 3.3) a bright spot appears in the center of the focal region and the sharp boundary of the expanding region slowly diffuses. The velocity of the expanding feature (moving to the right) calculated from the data is

$v = 4.9 \times 10^6$ m/s. The velocity remained constant from $T = 10$ ps to $T = 70$ ps. Then the boundary is no longer well defined.

The observed features can be interpreted as follows: The depleted region in the electron beam is an effect of strong deflection of the beam electrons by electric fields created between positive charges in the central region and an expanding cloud of hot plasma electrons. The beam electrons are deflected towards the center and go through a focus before reaching the detector. Within the cloud of plasma electrons the field rapidly decreases with increasing radius and vanishes in the region where the electrons fully screen the positive charge (seen as the edge of the depleted region on the detector).

The electron cloud radius is two orders of magnitude larger than the Debye length of the plasma (see below), far beyond what is expected from a simple model of charge separation. Generation of such a charge distribution is only possible if a small fraction of the electrons acquires a significantly higher energy than the bulk of the plasma electrons. Several mechanisms exist through which a small fraction of the electrons may acquire an energy close to or even exceeding the ponderomotive potential of the laser at the focus (250 eV in the experiments). The most important of these are heating of electrons through recollisions [79] and sequential multi-electron emission [80]. For the explanation of the moving side lobes deflection due to a combination of magnetic fields and ionization of the background gas has to be taken into account. This is confirmed by numerical simulations (see below).

3.2.3. Theoretical description

In the following section a theoretical approach is described, which explains the main features observed in the experiments.

The expanding hole

The usual charge separation expected in an OFI-plasma does not result in any fields observable by the experiment. This can be estimated by calculating the Debye length of the plasma given by

$$\Lambda_D = 527.5 \sqrt{\frac{\tau_e}{n}} \quad (\text{cm}), \quad (3.1)$$

where τ_e is the electron temperature in eV and n the electron density in cm^{-3} . For typical electron temperatures (tens of eV) and densities around 10^{17} cm^{-3} this results in submicron charge separation lengths. The electron deflection generating the images has thus to be explained by a fraction of electrons with much higher temperature escaping from the main plasma.

The main experimental feature, viz. the expanding region of electron beam depletion, can be explained by a simple model. Assume a spherical slowly expanding plasma generated with an initial diameter equal to the laser focus. A number Z of “hot” electrons escape the plasma in radial direction. The plasma is thus left with a charge $Z \cdot e$ and generates a radial electric field given by

$$E_r = \frac{Z \cdot e}{4\pi\epsilon_0 r^2} \quad (3.2)$$

where e is the elementary charge, ϵ_0 is the vacuum permeability and r is the distance from center. Within the electron cloud the field rapidly decreases with increasing radius and vanishes in the region where the electrons fully screen the positive charge. The deflection of the beam electrons can be calculated using the Rutherford scattering formula, which predicts deflection towards the plasma by an angle θ given by

$$\tan\left(\frac{\theta}{2}\right) = \frac{Z e^2}{8\pi\epsilon_0 r U_b}, \quad (3.3)$$

where U_b is the energy of the electron pulse in electronvolts. For small distances r from the plasma the beam electrons are strongly deflected towards the axis, resulting in their apparent depletion at early times (“overfocusing”). The charge $Z \cdot e$ can be determined from the radius r_1 of the expanding electron “hole” for which the central focus appears at first time. For this distance from the plasma the beam electrons are focused onto the axis at the detector, i.e.

$$\tan(\theta) = \frac{r_1}{L}, \quad (3.4)$$

where L is the distance from the plasma to the detector. Inserting this condition into eq. 3.3 and using the small-angle approximation one obtains for the number

of charges

$$Z = r_1^2 \frac{4\pi\epsilon_0 U_b}{eL}. \quad (3.5)$$

Inserting the experimental result from the data ($r_1 = 500 \mu\text{m}$ for the radius of the hole at which the focus first appears), a number of charges given by $Z = 5.8 \times 10^7$ is obtained. The model also yields an estimate for the energy U_{el} of the “hot” electrons leaving the plasma. However, here the model is too simple and the resulting energies are unrealistically high. This is due to the fact that the model ignores more complicated mechanisms such as the reflux of electrons being pulled back by the positive ions.

The model outlined above explains the hole in the electron beam at early times as well as the electron focus which appears later. However, to explain the origin of the moving lobes observed on either side of the plasma, ionization of the background gas and the effect of time-dependent magnetic fields have to be taken into account.

The moving side-lobes

This section now concentrates on the moving lobes of higher electron intensity, which are visible first in fig. 3.2 b) on the top and bottom edge of the depleted region. The lobes can be explained by a combination of ionization of the background gas and time-dependent magnetic fields which can be calculated in a quasi-cylindrical symmetry. Beyond the edges of the gas jet the laser intensity is still high enough to ionize the background gas and leave a cylindrical plasma (see section 3.3 below for more detail). Due to the fields created by charge separation the beam electrons are focused creating the lobes on the detector. In the experimental data, the lobes in the lower parts of the panels are brighter than the lobes seen in the corresponding upper parts. This can be explained by the absorption of the laser energy as the laser propagates through the gas jet.

However, to fully explain the lobes including their movement away from the center, the effect of magnetic fields has to be taken into account. According to Maxwell’s equations the temporal variation of the magnetic field B is the curl of

the electric field E :

$$-\frac{\partial \vec{B}}{\partial t} = \vec{\nabla} \times \vec{E}. \quad (3.6)$$

Because of the given experimental parameters a cylindrical geometry along the line of laser propagation (y -direction, compare fig. 3.4) is chosen. Writing the curl operator in cylindrical coordinates, the only non zero contribution in the present experimental configuration reads

$$\vec{\nabla} \times \vec{E} = \left[\frac{\partial E_r}{\partial y} - \frac{\partial E_y}{\partial r} \right] \vec{e}_\phi. \quad (3.7)$$

The dominant component of the E-field in this cylindrical plasma wire is radial (r -direction, see fig. 3.4). Therefore, to a good approximation, eq. 3.7 simplifies to

$$\vec{\nabla} \times \vec{E} \approx \frac{\partial E_r}{\partial y} \vec{e}_\phi. \quad (3.8)$$

Inserting eq. 3.8 into eq. 3.6 yields the expression

$$\frac{\partial \vec{B}}{\partial t} \approx -\frac{\partial E_r}{\partial y} \vec{e}_\phi. \quad (3.9)$$

A variation of the radial electric field along the line of laser propagation results in a time-dependent magnetic field “curled” around the direction of laser propagation. This is the situation on the edges of the gas jet: A steep gradient in the gas density leads to a steep gradient in charge density after ionization and thus to different radial electric field strength. The resulting magnitude of the B-field can thus be calculated according to

$$B(t) = \int_0^t \frac{\partial E_r(\tilde{t})}{\partial y} d\tilde{t}. \quad (3.10)$$

The effect of this time-dependent B-field grows with time. Close to time-zero it is negligible and only for later times it can be observed. This becomes evident in the results of numerical simulations (see below).

In the following chapter numerical simulations are presented which connect the above described theory with the experimental results and allow for the extraction

of the relevant physical parameters such as fields, number of charges and electron temperature.

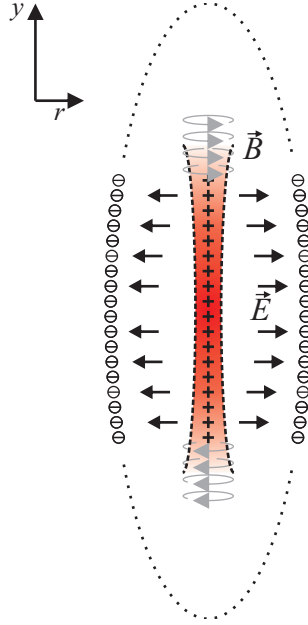


Figure 3.4.: Schematic illustration of the theoretical concepts. The figure shows a 2D-slice through the cylindrically symmetric plasma wire. Along the line of laser propagation a cylindrical plasma wire is created focusing the electron beam. The edges of the gas jet lead to time-dependent magnetic fields which are responsible for the “movement” of the lobes away from the center.

3.2.4. Numerical simulation

For the quantitative analysis of the patterns, the equation of motion for the expanding electrons in their self-generated electric field E was numerically solved in a Lagrangian coordinate system [81]. A quasi-2D cylindrical model is used where the electrons expand only radially, while the number and initial temperature of electrons depends on the axial position y (distance from the focus along the propagation direction of the laser). The corresponding magnetic field B is calculated by the time integral of the curl of the E -field.

The pattern on the detector for a given time-delay was then simulated by propagating a 20 keV electron beam of 5000 electrons through the fields generated by

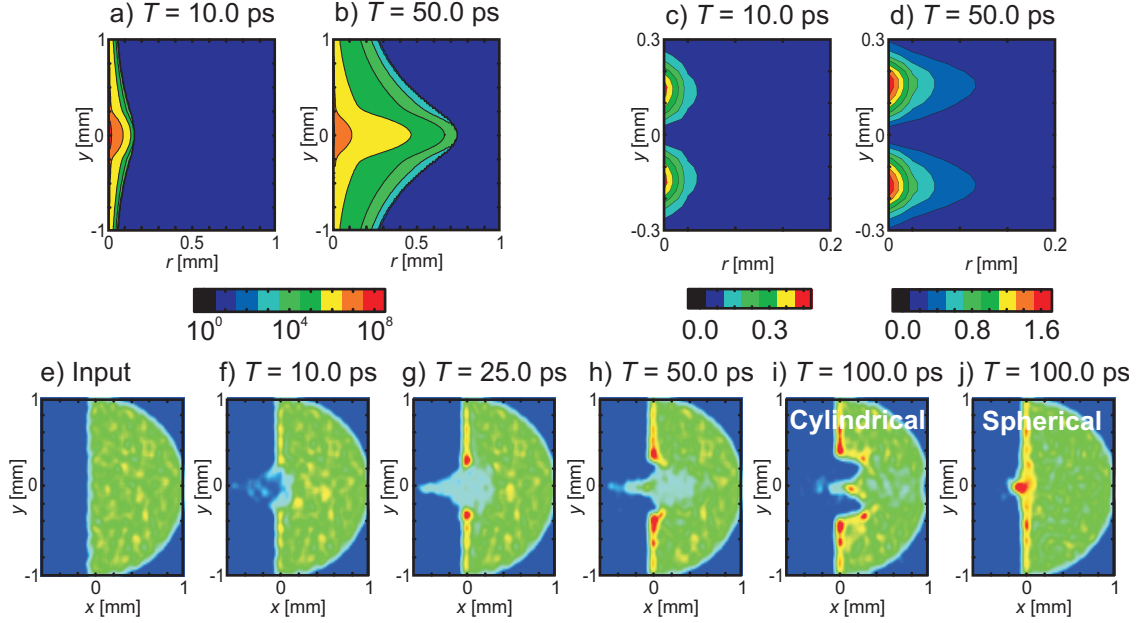


Figure 3.5.: Calculated plasma fields and simulated beam. The x - and y - scale of the panels correspond to the detector. a) ,b) Contours of the radial E-field in a cylindrical geometry for delays of 10 ps in a) and 50 ps in b). The color scale denotes \log_{10} of the field in units of Vm^{-1} . c),d), Azimuthal B-field, in units of tesla for delays of 10 ps in c) and 50 ps in d). e), Input electron beam (diameter 2 mm) used for the simulations. f)-i), Simulated beam pattern at the detector for delays of 10 ps in f), 25 ps in g), 50 ps in h) and 100 ps in i) with a cylindrical symmetry. j), Beam pattern at 100 ps delay applying the simulation with a spherical symmetry.

the simulations of the expanding electron cloud using the GPT-code [78]. To take the nozzle properly into account, a scatterplate was inserted obscuring the beam at $100 \mu\text{m}$ to the left of the center.

The cylindrical geometry is motivated by the experimental parameters: the laser beam (focus diameter $20 \mu\text{m}$ Rayleigh length $600 \mu\text{m}$) generates a thin plasma wire through the gas jet ($150 \mu\text{m}$ radius). A background gas density of 5% is also included in the calculations. The initial plasma density and electron temperature are proportional to the gas density and laser intensity, respectively, both of which depend on the position along the y -axis (see fig. 3.2 a)).

The best agreement between experiment and simulation was achieved for 5×10^7 charges. The hot electrons have an exponential energy distribution with a

temperature of 250 eV. The number corresponds to a fraction of 5×10^{-4} of the total number of electrons in the plasma. The number of charges is in good agreement with the result from the simple model (section 3.2.3). Figure 3.5 a)-b) shows contour plots of the calculated radial E-field for $T = 10$ ps and $T = 50$ ps, in \log_{10} scale. The expanding E-field leads to the expanding depleted region in the electron beam pattern, as more electrons are deflected. The field reaches a value of 10^8 V/m at the center of the gas jet ($y = 0$) where the density is highest and decreases with radial distance from the positive charges. The corresponding B-field (fig. 3.5 c)-d)) is azimuthal due to the cylindrical symmetry, and appears initially in the regions of high density gradient. There is a partial canceling of the deflection due to the azimuthal B-field, with a net deflection along y , away from the regions of high B-field.

Figure 3.5 e)-j) shows the simulated patterns. The left side of the electron beam is blocked to simulate the effect of the nozzle, which allows to see the deflected electrons. Electrons are initially deflected out of the central region by the E-field, with a maximum deflection angle of 9 mrad, in good agreement with the measured value. A weak line is visible along the laser trajectory, which corresponds to expansion of electrons from plasma generated in the background gas.

For $T > 10$ ps (fig. 3.5 g)-j)), the B-field also contributes to the depletion by deflecting electrons along y , which generates the side-lobes. As the fields evolve in time, the side-lobes move away from the center due to the B-field, and the depleted region grows due to the combined effect of the electric and magnetic fields, again in good agreement with experiment. The asymmetry on the brightness of the side-lobes, with the one on the side of the outgoing laser being weaker is possibly due to absorption of the laser across the gas jet. In the simulations the absorption of the laser is not included, thus the asymmetry does not appear. For $T \geq 100$ ps, the expansion is no longer cylindrical, as the electrons have expanded well beyond the initial length of the plasma wire (the diameter of the gas jet), and the experimental pattern (fig. 3.2) shows a combination of cylindrical and spherical features. A full 3D model would be necessary to fully reproduce the experiment in this case. However, the main features are captured by two separate simulations, with cylindrical and spherical symmetry (fig. 3.5 i)-j)). The side-lobes and depleted region are reproduced in the cylindrical case, while the round focused spot in the center appears in the spherical case. The pattern in the case of spherical symmetry

remains relatively unchanged up to 200 ps. The focused spot can best be explained by a positively charged core and a spherical cloud of expanding electrons.

In summary, the simulations capture the main features of the experiment, with good agreement for the early stages and qualitative agreement for the later stages and allow for calculation of the fields, total charge and electron temperature. They confirm the interpretation of the images given at the end of section 3.2.2. The laser separates a positive core of ions and an expanding cloud of electrons. The fraction of the probe electron beam traversing this region is focused towards the beam axis. Initially, this results in an electron beam focus before the detector and a depleted region in the images is observed. As the electron cloud expands the focusing becomes weaker until the focus reaches the detector. A bright spot develops in the center of the depleted region. The expanding lobes on both sides of the depleted region are explained taking into account the magnetic fields and ionization of the background gas along the line of laser propagation. The magnetic fields are due to the variation of the radial electric field along the line of laser propagation.

3.3. Low density OFI-plasma

The above described experiments were performed using a gas jet. However, to explain all experimental features, ionization of the background gas had to be taken into account. In the following section the situation of ionization in the background gas is examined in more detail. Studies of low density OFI-plasmas without a gas jet are presented. The experimental setup is basically the same as described above. The nozzle is moved far away from laser and electron beams and used only to control the pressure of the homogeneous background gas.

3.3.1. Experimental results

Figure 3.6 shows the distortion of the electron beam due to the plasma, at a relative delay of 100 ps between electron and laser pulses. Figures 3.6 a) and 3.6 b) show the electron beam as recorded on the CCD without and with the plasma, for a background gas pressure of 2.6×10^{-4} mbar. The path of the laser beam is visible as a narrow line with increased electron flux, surrounded by a depleted region.

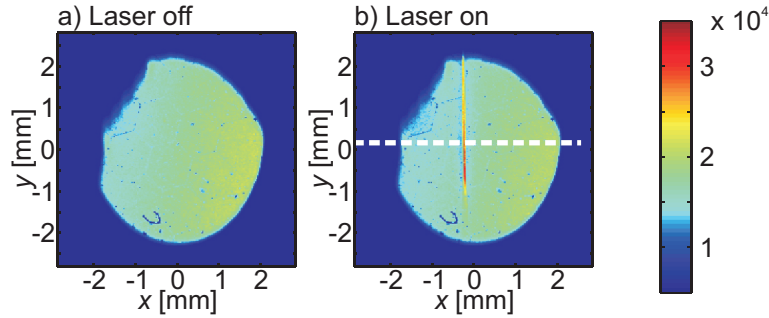


Figure 3.6.: Deflection of electrons owing to plasma fields at a time delay of 100 ps. a), b) Electron-beam pattern recorded on the CCD without plasma and with plasma for a gas pressure of $2.6 \cdot 10^{-4}$ mbar. The scale is the same for both images, and the color bar denotes the number of counts per pixel on the CCD.

Figures 3.7 a)-d) show cross sections of the electron beam (along the dotted line in fig. 3.6 b) for increasing gas pressure (8.6×10^{-5} mbar, 2.6×10^{-4} mbar, 1.1×10^{-3} mbar and 5.3×10^{-3} mbar, respectively). The line can be explained being the effect of focusing of the beam electrons by a positively charged plasma cylinder: The laser ionizes a cylindrical volume as it propagates through the gas. The positive charge at the center is screened by an expanding cloud of electrons, thus only a fraction of the probe electrons are deflected (fig. 3.8). For higher gas density the charge at the center increases, leading to overfocusing of the electron beam (the beam goes through a focus before reaching the CCD). The pattern becomes weaker for lower pressures and is only barely visible for pressures below 5×10^{-5} mbar (not shown).

At an intensity of 4×10^{15} W/cm² the classical over the barrier model [70] predicts 4 electrons being ionized from each nitrogen molecule. The electron energy generated by a linearly polarized laser is relatively low [67] but electrons will still be able to leave the central plasma core and generate electric fields. The effect of the outgoing electrons as a function of time is displayed in fig. 3.9 for a nitrogen pressure of 6.5×10^{-5} mbar. Each vertical line in the figure corresponds to a cross section (same as for fig. 3.7 a)-d)) for a specific time delay. The red line along the center represents increased counts on the detector, while the blue area corresponds to the depleted region (decreased counts) around the focus as seen also in fig. 3.7 a)-d). The boundary of the dark blue expanding region corresponds to the maximum distance from which electrons are deflected towards the center. This

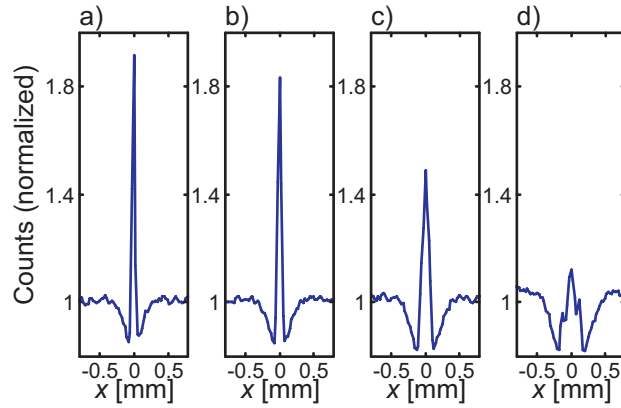


Figure 3.7.: Deflection of electrons owing to plasma fields at a time delay of 100 ps. a)-d) Cross sections of the electron-beam pattern (along the dotted line in fig. 3.6 b)) for gas pressures of $8.6 \cdot 10^{-5}$ mbar, $2.6 \cdot 10^{-4}$ mbar, $1.1 \cdot 10^{-3}$ mbar, and $5.3 \cdot 10^{-3}$ mbar, respectively, normalized to the number of counts on the undisturbed electron beam.

boundary expands with a velocity of 1.1×10^6 m/s, corresponding to an electron energy of 3.4 eV. Therefore, plasma electrons with energy ≥ 3.4 eV can escape from the plasma core.

3.3.2. Theoretical description

Below, a theoretical model of this experiment is presented. From this model the temperature of the plasma electrons is determined. The analysis is carried out in cylindrical geometry. Experimentally, the laser pulses ionize the nitrogen in a cylindrical volume with diameter of $20 \mu\text{m}$ and length on the order of 1 mm. A central charge with a line density of \tilde{Z} ions per meter generates a radial electric field deflecting beam electrons towards the center by an angle

$$\theta = \frac{e\tilde{Z}}{4U_b\varepsilon_0}, \quad (3.11)$$

where U_b is the electron energy in electronvolts, e is the elementary electric charge, and ε_0 the vacuum permittivity. The deflection angle is independent of the distance from the center, similar to a cylindrical biprism [82]. This simple analytical treatment, however, does not take into account that plasma electrons partially screen the central charge. At early times all plasma electrons are still close to the cen-

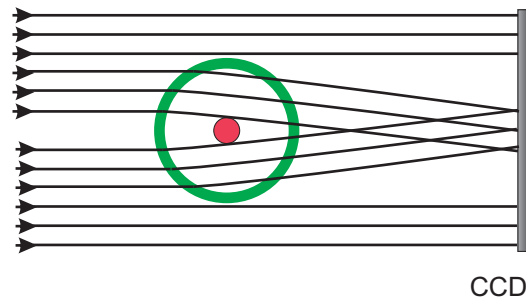


Figure 3.8.: Sketch of a few representative trajectories of the probe beam electrons traversing a plasma with cylindrical symmetry. The red circle in the center represents a positively charged core, and the green ring represents a cloud of electrons escaping from the plasma core. The area outside of the green ring is completely screened from the positive charges; i.e., it is field free. The trajectories shown, generate on the detector a focused line surrounded by a depleted region.

ter and most of the surrounding volume is screened, thus the probe electron beam is depleted only in a region close to the plasma core. The positive ions remain fixed inside the plasma cylinder throughout the duration of the experiment, due to their large mass. As the plasma electrons move away from the center the screening decreases, resulting in the expansion of the depleted region in the probe electron beam and an increase in the intensity of the focused line.

3.3.3. Numerical simulation

On the basis of this model, numerical simulations are carried out coupling the result of a hydrodynamic plasma code [83] (which solves the equations of motion of the electrons in Lagrangian coordinates) to the GPT-code [78] for calculating electron beam propagation. The temporal evolution of the peak intensity of the focused line resulting from the simulation is presented in fig. 3.10. The experimental values are compared with simulations using different electron temperatures of 20 eV, 30 eV and 40 eV. An exponential electron energy distribution with a temperature of 30 eV gave best agreement with experiment. The local minimum in the experimental data around 150 ps is an artefact due to the limited number of pixels that sample the peak. Figure 3.11 shows cross sections of the experimental and simulated electron beam profiles. The simulations accurately reproduce the experimental curves, both

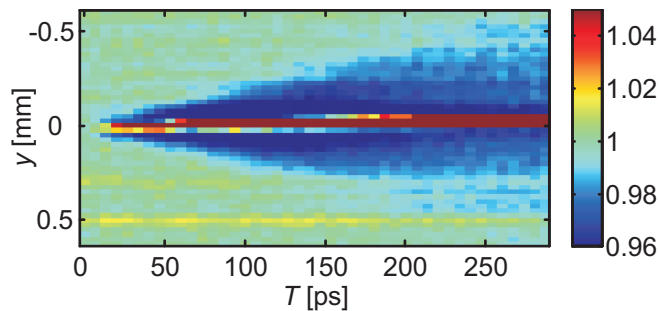


Figure 3.9.: Evolution of the plasma fields. The vertical axis corresponds to a cross section through the plasma line, as shown in Fig 3.6 b). The horizontal axis is the pump-probe delay. The color scale corresponds to the number of counts per pixel on the CCD, normalized to the number of counts on the undisturbed electron beam.

in the temporal evolution and the amplitude of the peaks. The only adjustable parameter in the simulations is the electron temperature. From the simulations it follows that roughly 90% of the ionized electrons escape leaving behind a highly-charged plasma.

3.4. Limitations

The high sensitivity of electron deflectometry is based on the fact that even small charge imbalances within the plasma are observable as distortions in the spatial profile of the electron beam. The main parameter limiting the sensitivity as well as the spatial resolution of the method is the emittance of the electron beam. The minimum field that can be measured in a particular experiment can be estimated by comparing the angular spread

$$\Delta\phi_\varepsilon = \frac{\varepsilon}{r_b} \quad (3.12)$$

of electron trajectories due to the emittance to the deflection angle

$$\Delta\phi_E = \frac{El_p}{2U_b} \quad (3.13)$$

of an electron in an electric field E created by the plasma. In these equations, r_b denotes the radius of the electron beam, l_p the length of the plasma (in direction of

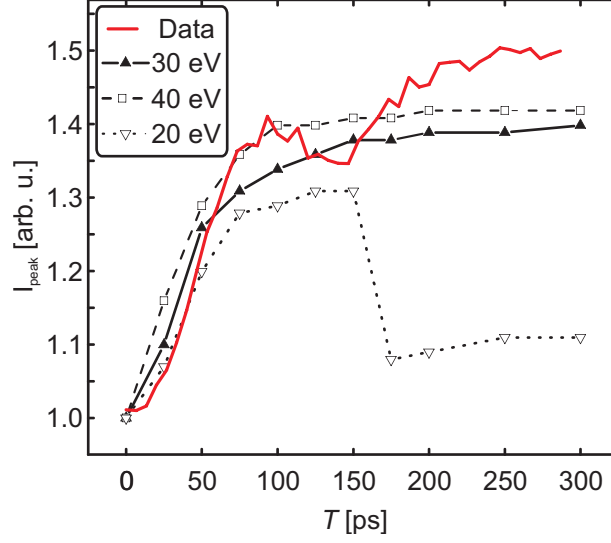


Figure 3.10.: Peak intensity as a function of delay time. The intensity is normalized to the intensity of the undisturbed electron beam. The initial electron density is 10^{13} cm^{-3} . The figure compares experimental data with simulations assuming three different electron temperatures.

the electron beam) and U_b the energy of the beam electrons in eV. The emittance of the electron beam can be determined by evaluating the blurring of the shadow of a sharp aperture, resulting in $\varepsilon = 1.5 \text{ mrad mm}$. Taking $l_p = 50 \text{ }\mu\text{m}$, 20 kV electrons allow fields down to $6.7 \times 10^5 \text{ V/m}$ to be measured. Such a field occurs at a distance of $100\mu\text{m}$ from a charged core with a charge of about a pC.

The spatial resolution is also limited ultimately by the emittance of the electron beam. The blurring of a sharp spatial structure by the beam emittance yields a minimum resolvable distance between two spots $\Delta x = \varepsilon L/r_b$, where L is the distance between the plasma and the detector. The resolution can be improved by using an expanding beam. If M is the magnification achieved at the detector the corresponding relation is $\Delta x = \varepsilon L/Mr_b$. Note the tradeoff between spatial resolution and detectable field: While the spatial resolution increases with decreasing L , the field sensitivity suffers because $\Delta\phi_E L$ decreases and may even become smaller than the minimum resolvable structure on the detector.

The temporal resolution of the experiment may be improved by using a shorter electron pulse, which can be accomplished by using fewer electrons per pulse and reducing the propagation distance to the target. Additionally, the resolution is

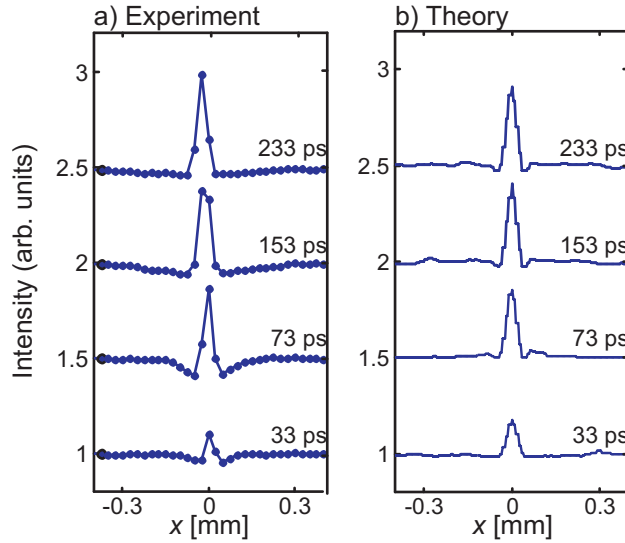


Figure 3.11.: Cross sections through the center of the focused line on the CCD for different time delays. a) Experimental results, with parameters as in Fig. 3.9. b) Results from the simulation. The intensity is normalized to the intensity of the undisturbed electron beam. The plots for different delay times are displaced vertically for visual clarity.

also limited by the velocity mismatch between the laser pulse and the subrelativistic electron pulse. For 20 kV electrons and a $100 \mu\text{m}$ plasma the time difference amounts to 900 fs. By increasing the electron energy this mismatch can be eliminated, however at the cost of field sensitivity.

3.5. Conclusions

In conclusion deflectometry is a new method of imaging OFI-plasmas with picosecond temporal resolution. New features of OFI plasma were observed using this method, such as a cloud of electrons separating from the plasma core far beyond the Debye length in the case presented in section 3.2.1. Additionally the effect of both electric and magnetic fields on the probe electron beam was observed. The relevant physical parameters, such as the fields, number of charges and electron temperature, were calculated numerically and compared with the images resulting from the experiments.

The sensitivity of subrelativistic electrons to relatively small fields makes this

method applicable even to investigate the dynamics of low-density plasmas. In the regime of low density plasmas very different features are measured, most notably, the minimum electron energy required to escape the plasma is much lower, resulting in most of the electrons escaping and leaving behind a positively charged plasma core. As much 90% of the electrons escape for an initial plasma density of $7 \times 10^{12} \text{ cm}^{-3}$ as opposed to the small fraction (5×10^{-4}) of the electrons which are able to escape the plasma in the gas jet. From the experiments a minimum electron escape energy of 3.4 eV was directly measured, and an electron temperature of 30 eV was obtained by comparing the experimental results with simulations.

4. Time-resolved electron diffraction from selectively aligned molecules

In this chapter, electron pulses are used for ultrafast-electron-diffraction (UED, [9]). Since the famous experiments of Davisson in 1927 and Thomson in 1933 [84, 85], who received the Nobel Prize in Physics in the year 1937 for their work on electron diffraction, this method has developed into a powerful tool for structure determination. Advanced into a pump-probe method, namely UED, time-resolved electron diffraction opened the way for studying structural dynamics with picosecond [23] or femtosecond [21] temporal and sub-Angstrom spatial resolution. In the gas phase, however, structure determination is still hampered by the fact that molecules are randomly oriented. Molecular alignment would allow for the retrieval of three dimensional structures of complicated molecules. The experiments presented in this chapter aim to show for the first time the possibility of recording diffraction patterns from transiently aligned molecules.

4.1. Introduction

Determination of structure and dynamics using isolated molecules is important for obtaining accurate information, with the molecules free of external forces and intermolecular interactions. The reason for electron diffraction being very successful in structure determination of gas phase molecules, is the large cross-section of electrons to scatter from atoms [44]. However, due to the random orientation of the molecules in the gas phase only 1D information (the interatomic distances) can be extracted from the diffraction patterns, which limits the size of molecular structures that can be studied.

The technique of X-ray crystallography has been successful in studying larger molecules. For example, the majority of the known protein structures has been determined by X-ray diffraction from crystallized samples [43]. This technique, however, is limited to the fraction of molecules that can be crystallized. Additionally, crystallized molecules are subject to strong fields that constrain their conformation and hamper the study of dynamics. Recently, a strategy was proposed in which a single molecule is exposed to a large enough number of photons within an X-ray laser pulse short enough to capture a diffraction pattern before the molecule is destroyed [51]. Diffraction images of μm and nm-sized objects have been recorded with femtosecond soft-X-ray pulses [86, 87]. However, this approach currently relies on large-scale facilities.

An alternative approach consists in recording a diffraction pattern from an ensemble of aligned molecules in the gas phase. It has been shown theoretically that electron diffraction from aligned molecules in the gas phase reveals not only the interatomic distances but also the corresponding angles [13, 14]. Aligning molecules in helium droplets using powerful CW lasers has been proposed [88], and electron diffraction from adiabatically aligned molecules has been demonstrated experimentally [89]. However, the presence of strong alignment fields can affect the structure and dynamics of the molecules under investigation and prevents the study of field-free molecules. This problem can be overcome using a sample of non-adiabatically aligned molecules in which the alignment field is no longer present at the time the diffraction pattern is recorded.

Molecules can be aligned by means of femtosecond laser pulses either via active laser alignment techniques [15] or selectively through a dissociation reaction [13]. In both cases ultrashort electron pulses are required to record the diffraction pattern before the alignment vanishes due to molecular rotations. UED experiments have been performed with picosecond resolution for gas phase experiments [23] and femtosecond resolution in solid-state experiments [90, 91], but so far the possibility of recording a diffraction pattern from field-free aligned molecules has not been demonstrated experimentally.

The experiments in this chapter aim to show for the first time electron diffraction patterns recorded from a sample of transiently aligned molecules. In the experiments presented here, $\text{C}_2\text{F}_4\text{I}_2$ (1,2-diiidotetrafluoroethane) molecules are aligned selectively using a photoinduced dissociation reaction. The breaking of a molecular

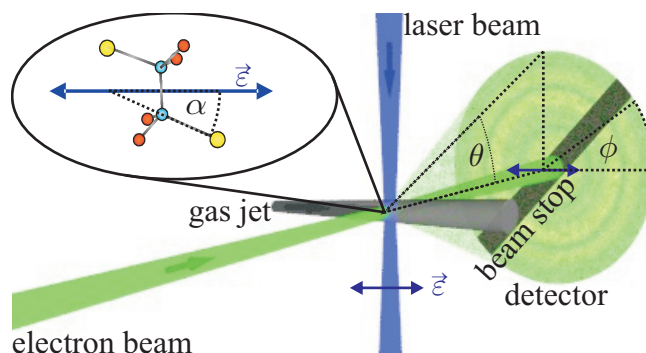
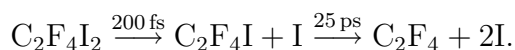


Figure 4.1.: Schematic drawing of a time-resolved gas electron diffraction experiment; θ and ϕ are the scattering angle and the azimuthal detector angle, respectively; $\vec{\epsilon}$ is the laser polarization. The inset shows a $\text{C}_2\text{F}_4\text{I}_2$ -molecule with colored atoms: light blue for C, red for F and yellow for I; α is the angle between the laser polarization and the C-I-bond.

bond gives a clear signal in the time-resolved diffraction patterns, which simplifies the investigation of the transient alignment effect. The molecules are dissociated using a linearly polarized femtosecond laser pulse. The corresponding absorption cross-section is proportional to $\cos^2(\alpha)$, where α is the angle between the laser polarization and the direction of the transition dipole moment (fig. 4.1). For $\text{C}_2\text{F}_4\text{I}_2$ the transition dipole moment of the most intense transition is parallel to the C-I bond, along which the dissociation takes place [92]. Therefore, the $\text{C}_2\text{F}_4\text{I}$ radicals emerge preferentially with the dissociated C–I direction aligned along the laser polarization vector. Due to the rotations of the molecules the alignment decays on a picosecond time scale (see below). Note that using circular polarization an aligned ensemble of un-dissociated molecules is produced.

The time constants of the two-step dissociation reaction have been determined using mass spectrometry [92]:



The first iodine atom breaks off within 200 fs, leading to the intermediate $\text{C}_2\text{F}_4\text{I}$ radical, which subsequently fragments within some 25 ps to yield C_2F_4 . The structure determination of the intermediate $\text{C}_2\text{F}_4\text{I}$ has been one of the first successes of UED [23].

4.2. Theoretical basics for static and time-resolved electron diffraction

4.2.1. Static gas-electron-diffraction (GED)

This section summarizes the basic formulas needed for the theoretical description of GED patterns. In the analysis of the diffraction patterns [45], the diffracted electron intensity (I_{tot}) is written as the sum of two contributions, the ensemble-averaged atomic (I_{at}) and molecular (I_{mol}) scattering intensities:

$$I_{\text{tot}}(s, \phi) = I_{\text{at}}(s, \phi) + I_{\text{mol}}(s, \phi), \quad (4.1)$$

where ϕ is the azimuthal detector angle (compare fig. 4.1). The variable s represents the magnitude of the momentum transfer between incident and diffracted electrons

$$s = \frac{4\pi}{\lambda} \sin\left(\frac{\theta}{2}\right), \quad (4.2)$$

where θ is the scattering angle and λ the electron wavelength:

$$\lambda = \frac{h}{\sqrt{2m_e U_b + U_b^2/c^2}}. \quad (4.3)$$

Here, h is the Planck constant, m_e the electron mass, c the speed of light and U_b the kinetic energy of the electrons. Electrons with an energy of 20 keV have a wavelength of $\lambda = 0.086 \text{ \AA}$ and for electrons with an energy of 29 keV the wavelength is $\lambda = 0.07 \text{ \AA}$.

If the gas molecules consist of N atoms with elastic and inelastic scattering factors f and S , respectively, the atomic scattering intensity I_{at} is written as:

$$I_{\text{at}}(s) = C \sum_{i=1}^N \left(|f_i(s)|^2 + 4 \frac{S_i(s)}{a_0^2 s^4} \right), \quad (4.4)$$

with a_0 being the Bohr radius and C a proportionality constant. It reflects the electron scattering from individual constituent atoms. The atomic scattering intensity is rotationally symmetric with respect to the axis of the electron beam (eq. 4.4 does not depend on the azimuthal detector angle ϕ). For the structural analysis

only the molecular scattering intensity I_{mol} is of interest. Due to the interference of waves scattered from pairs of atoms with an interatomic distance r_{ik} the scattering intensity contains a modulation according to:

$$I_{\text{mol}}(s, \phi) = C \sum_{i=1}^N \sum_{\substack{k=1 \\ k \neq i}}^N |f_i| |f_k| \exp\left(-\frac{1}{2} l_{ik}^2 s^2\right) \cos(\eta_i - \eta_k) F_{ik}(s, \phi), \quad (4.5)$$

where l_{ik} is the mean amplitude of vibration of atom pair $i - k$ and η_i represents the phase shift suffered by the respective scattered wave.

In the case of standard GED, the molecules in the gas jet are randomly oriented. Thus, the molecular scattering intensity I_{mol} is rotationally symmetric (about the axis of beam propagation), and the factor $F_{ik}(s)$ depends only on s :

$$F_{ik}(s) = \frac{\sin(sr_{ik})}{sr_{ik}}. \quad (4.6)$$

Theoretical one-dimensional functions $I_{\text{at}}(s)$ and $I_{\text{mol}}(s)$ are shown in fig. 4.2 a) for the case of the I_2 molecule. (The distance between the iodine atoms is 2.67 Å [14].) The scattering factors are taken from the literature [93].

The scattering factors f_i decrease with the square of s^{-1} , leading to a decrease of the total scattering intensity with s^{-4} multiplied by an additional factor s^{-1} from the F_{ik} -factor. Thus, in total

$$I_{\text{mol}} \propto s^{-5}. \quad (4.7)$$

For revealing the fine details of the electron scattering pattern it is common usage to present the scattering pattern in the form of the so-called modified molecular scattering intensity $sM(s, \phi)$. To highlight the oscillatory behavior due to the interferences, I_{mol} is scaled by the atomic intensity I_{at} and multiplied by s , yielding:

$$sM(s, \phi) = s \frac{I_{\text{mol}}(s, \phi)}{I_{\text{at}}(s)}. \quad (4.8)$$

In the case of isotropic GED azimuthal averaging of the $sM(s, \phi)$ -patterns results in the one-dimensional $sM(s)$ -function. For a diatomic like I_2 this $sM(s)$ -function is a simple sine-function (compare fig. 4.2 b)). The sine Fourier transform of $sM(s)$

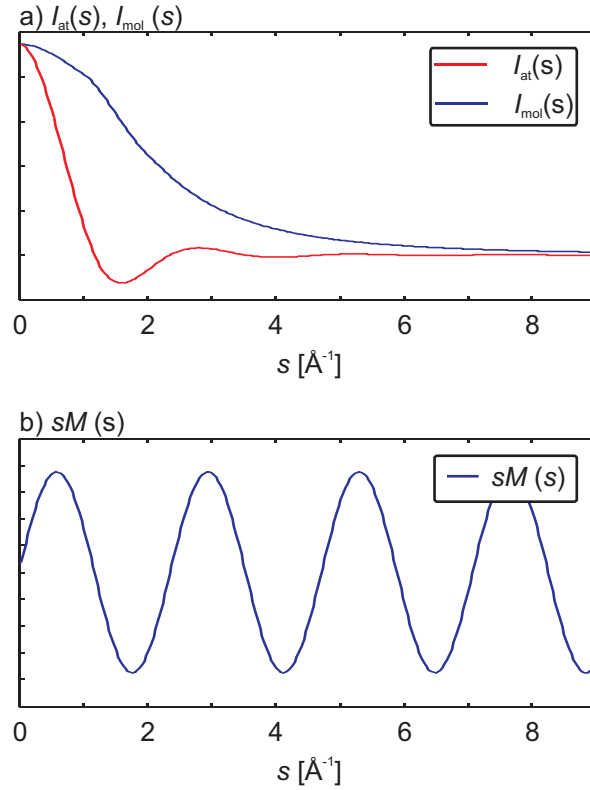


Figure 4.2.: a) Theoretical atomic intensity I_{at} and molecular intensity I_{mol} calculated for the I_2 molecules. The distance between the Iodine atoms is 2.67 \AA in this molecule [14]. b) Theoretical $sM(s)$ -curve for I_2 .

yields the radial distribution function $f(r)$ which peaks at the interatomic distances [45]:

$$f(r) = \int_0^{s_{\text{max}}} sM(s) \exp(-k_d s^2) \sin(sr) ds. \quad (4.9)$$

Because of the finite s -range in the experiment, the integral is truncated at s_{max} and an exponential damping factor has to be introduced to suppress artificial high frequency oscillations. The damping constant k_d has to be determined empirically.

In the general case of anisotropic samples, the diffraction patterns are not rotationally symmetric but depend on the azimuthal detector angle ϕ , which leads to a ϕ -dependence of the F_{ik} -factor in the expression for I_{mol} (eq. 4.5). Particularly, in the case of selective alignment through photodissociation, the molecules in the

gas jet are no longer randomly oriented and F_{ik} reads [14]

$$F_{ik}(s, \phi) = \frac{j_1(sr_{ik})}{sr_{ik}} + \left[\sin^2(\Omega_{ik}) + (2 - 3 \sin^2(\Omega_{ik})) \cos^2\left(\frac{\theta}{2}\right) \cos^2(\phi) \right] \frac{j_2(sr_{ik})}{2}, \quad (4.10)$$

where j_l is the spherical Bessel function of order l , and Ω_{ik} is the angle between r_{ik} and the laser polarization. Equation 4.10 shows how the cosine-square-dependence of dissociation translates into an azimuthal cosine-square dependence of the diffraction pattern.

4.2.2. Time-resolved gas-electron-diffraction

In order to study the reaction dynamics the Diffraction-Difference method is applied [50]. To follow the structural changes two-dimensional diffraction images are recorded for different delays, T , between the laser and electron pulses. Each of these images thus reflects the transient behavior of the molecular structures at the corresponding temporal delay following laser excitation. In contrast to the ground state diffraction pattern, the scattering intensity at time delays following the laser excitation contains contributions not only from one molecular species but as well from the reaction intermediates and products. However, in most cases, the majority of the diffracting molecules still are the parent molecules. Additionally, the molecular scattering intensity from reaction intermediates or products is usually weaker than the corresponding intensity from a parent molecule because it has fewer internuclear pairs. To bring out the diffraction signal originating from the structural changes during the reaction, difference patterns $\Delta[sM(s, \phi, T)]$ are calculated according to

$$\Delta[sM(s, \phi, T)] = sM(s, \phi, T) - sM(s, \phi, t = \tilde{T}). \quad (4.11)$$

The $sM(s, \phi, T)$ -patterns are recorded at a certain time T while a ground state pattern $sM(s, \phi, t = \tilde{T})$ is taken at a time step \tilde{T} before the laser arrival. Now, the $\Delta[sM(s, \phi, T)]$ reflects comparable contributions from the parent and product or intermediate structures in contrast to the original raw data, where the majority of the signal originates from the parent molecules. Additionally, the atomic background, which is unaffected by the reaction is essentially removed by the sub-

traction. Figure 4.3 shows two calculated examples of $\Delta [sM(s, \phi)]$ -patterns, where

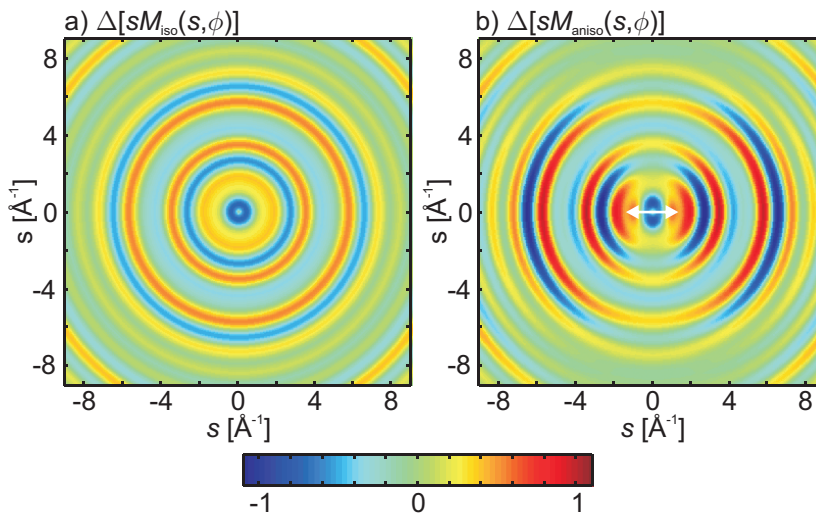


Figure 4.3.: Theoretical $\Delta [sM(s, \phi)]$ -patterns. For the calculation it is assumed that from a sample of $\text{C}_2\text{F}_4\text{I}_2$ -molecules one third is dissociated to $\text{C}_2\text{F}_4\text{I}$. The molecular intensities in pattern a) are calculated using eqs. 4.5 and 4.6, while the molecular intensities for pattern b) are calculated using eqs. 4.5 and 4.10. In part b) a white arrow indicates the direction of the polarization of the dissociation laser.

from a sample of $\text{C}_2\text{F}_4\text{I}_2$ -molecules one third is dissociated into $\text{C}_2\text{F}_4\text{I}$. Part a) is calculated assuming no anisotropy. Both species are randomly oriented. In part b) the product $\text{C}_2\text{F}_4\text{I}$ is assumed to be created with its dissociated C-I-bond in a perfect \cos^2 -distribution parallel to the polarization of the dissociating laser. The direction of laser polarization is indicated as a white arrow in part b). The cosine square dependence of the dissociation translates into a clear anisotropy in the diffraction pattern.

4.3. Experimental methods

4.3.1. Experimental setup

The experimental geometry of the diffraction experiments is shown in fig. 4.4. $\text{C}_2\text{F}_4\text{I}_2$ molecules at a pressure of 30 mbar are seeded in helium at 270 mbar for rotational cooling. Before each experimental run, the gases are mixed for 40 to

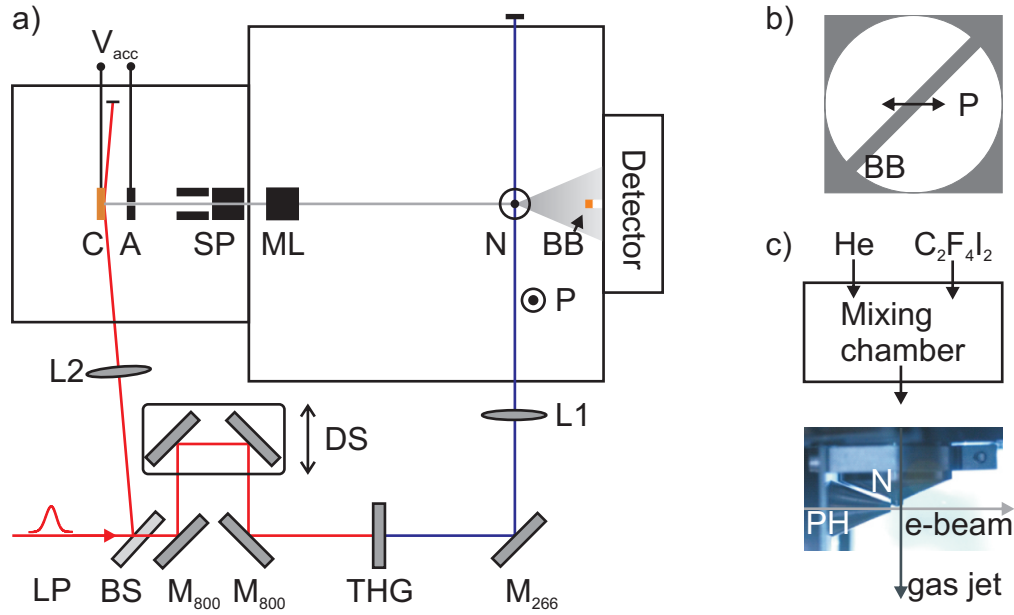


Figure 4.4.: a) Experimental setup: LP: 800 nm, 50 fs laser pulses at 1kHz repetition rate; BS: dielectric beam splitter; M_{800} : 800 nm dielectric mirror; DS: motorized delay stage; THG: two 1 mm BBO crystals for third harmonic generation; M_{266} : 266 nm dielectric mirror; L1: focusing lens ($f = 300$ mm); L2: focusing lens ($f = 300$ mm); C: copper photocathode; A: copper anode with $200 \mu\text{m}$ hole; V_{acc} : static acceleration voltage (29 kV); SP: steering plates; ML: magnetic solenoid lens; N: gas nozzle; BB: copper stripe to block transmitted electron beam; Detector: phosphor screen fiber coupled to CCD camera with 16-bit dynamic range. b) Schematic drawing of the detector geometry: The round area represents the usable area which is fiber connected to the phosphor coating (compare fig. 3.1 c)). The dark stripe (BB) represents the dark area behind the beam stop. The arrow (P) indicates the direction of the laser polarization. c) Gas mixing scheme: Before expanding through the nozzle the $\text{C}_2\text{F}_4\text{I}_2$ -molecules are mixed at 30 mbar with helium at 270 mbar. N: gas nozzle; PH: $200 \mu\text{m}$ pinhole.

60 minutes. After the mixing, the gases are introduced into the vacuum chamber using a de Lavale nozzle of $50 \mu\text{m}$ inner and $150 \mu\text{m}$ opening diameter. The mean backing pressure during the experiments is $P_0 = 175$ mbar. Using P_0 , the rotational temperature of the molecules is calculated using an empirical formula [94]:

$$\tau_{\text{rot}} = p \cdot (P_0 d)^q, \quad (4.12)$$

where $p = 1525$ and $q = -1.17$ are empirical constants and d the inner nozzle diameter in mm and P_0 the backing pressure in Torr. With the experimental parameters the rotational temperature is calculated to be 168 K.

The laser system and the vacuum apparatus are the same as those used for the experiments described in chapter 3, however, modified for the diffraction experiments. For the dissociation reaction of the $C_2F_4I_2$ -molecules UV-laser pulses are required. Therefore, the fundamental pulses are frequency tripled to 267 nm using two 1 mm BBO crystals. To optimize the conversion efficiency, the laser pulses are stretched to 100 - 150 fs before the crystals. The resulting UV pulses with an energy of 100 μ J are focused to a 200- μ m diameter inside the gas jet.

Before the frequency conversion a weak laser beam is split from the main part to create electron pulses as described in chapter 3. The electron beam is aligned onto the gas jet through a 200 μ m pinhole situated 1 mm before the gas jet (see the bottom of fig. 4.4 b)). Using a solenoid lens the electrons are focused such that a small spot on the detector is achieved while still a good fraction ($\approx 1/3$) of electrons passes the pinhole. The diffraction patterns are recorded using a phosphor screen fiber-coupled to a cooled CCD camera with 16-bit dynamic range (see fig. 3.1 c)). The electron beam current is determined using a Faraday cup to calibrate the detector as described in chapter 3. During the experiments the number of electrons per pulse was kept on average at 12000. The duration of the pulses on target was calculated to be 2.3 ps using the GPT-code [78]. Note that here a shorter electron pulse duration is achieved for a larger number of electrons per pulse as compared to the short pulses in chapter 3 (2300 electrons per pulse resulted in 2.6 ps pulse duration). This is an effect of the higher voltage which is applied in the diffraction experiment. The electron pulses are faster and have less time for the broadening.

Including geometrical effects and the pulse duration the temporal resolution of the diffraction experiment is calculated to be effectively 3 ps. The electron beam, laser beam and gas jet are mutually orthogonal. To avoid saturation, the directly transmitted electron beam is blocked using a 2 mm thick copper stripe. The beam stop is oriented diagonally (compare fig. 4.4 b)) because this gives equal weight to the detector directions perpendicularly and parallel with respect to the laser polarization. In this geometry it is possible to compare the two directions and investigate a possible anisotropy due to molecular alignment.

4.3.2. Calculation of the alignment decay time

The transient molecular alignment due to dissociation results in anisotropic diffraction patterns (compare section 4.2). Approximating the decay of this anisotropy exponentially [16] it is possible to estimate how long the transient alignment can be observed in the experiment. The decay time t_d can be calculated according to

$$t_d = \left[\frac{2\pi}{9} \frac{I}{k_B \tau_{rot}} \right]^{\frac{1}{2}}. \quad (4.13)$$

Here, k_B is the Boltzmann constant, τ_{rot} the rotational temperature of the molecules and I the moment of inertia of the molecule. The moment of inertia for $C_2F_4I_2$ is calculated to be approximately $1500 \text{ amu } \text{Å}^2$ using the computer program HyperChem. From the calculations, a decay time $t_d = 2.7 \text{ ps}$ is expected.

4.4. Experimental results

4.4.1. Static electron diffraction

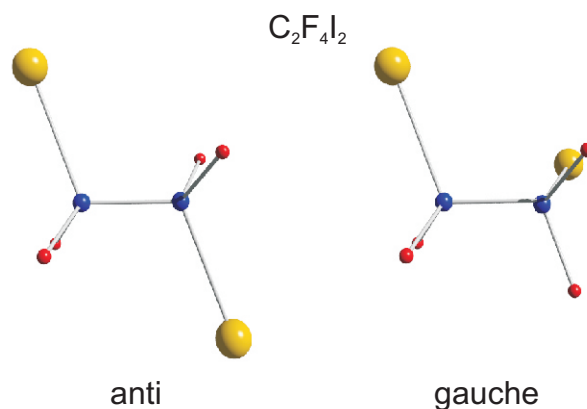


Figure 4.5.: $C_2F_4I_2$ -Molecule. The constituent atoms are color coded, with yellow for iodine, light blue for carbon, and red for fluorine. a) Anti-rotamer; The torsion angle about the C–C-bond is 180° . b) Gauche-rotamer; The torsion angle about the C–C-bond is $\approx 70^\circ$. [95]

The molecule is shown schematically in fig.4.5. It exists as an anti and a gauche rotamer [95]. The two forms differ in the rotation angle of the two CF_2I -groups about the C–C axis, with respect to each other. In the anti-form this angle is 180° ,

while in the gauche-form the angle is $\approx 70^\circ$ [95]. In the calculations a fraction of 19 % gauche is used.

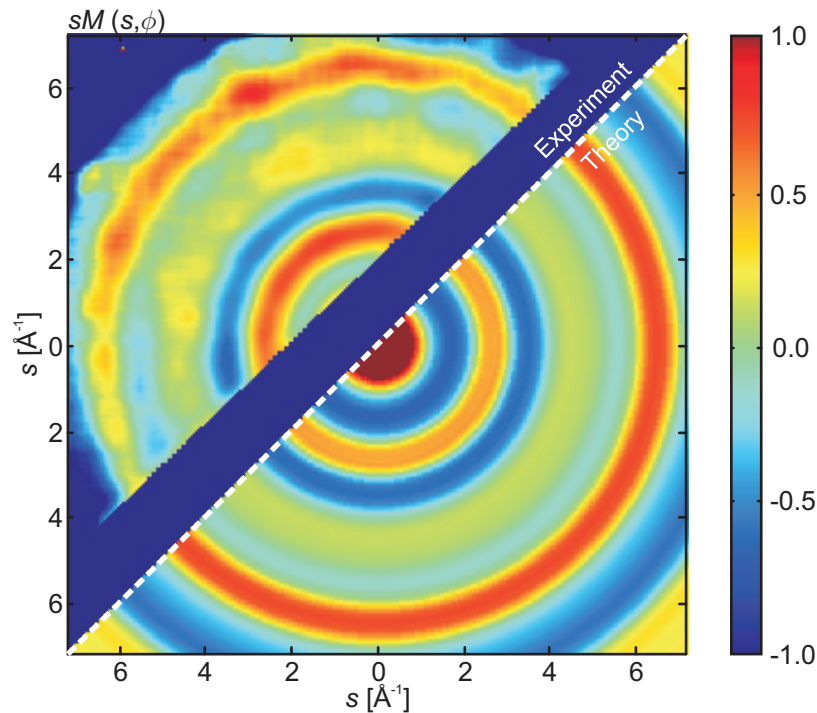


Figure 4.6.: Experimental and theoretical sM for $C_2F_4I_2$. The upper left half of the image displays the experimental data while the lower right half shows the calculated image. The dark region splitting the image is the shadow of the beam stop.

Figure 4.6 shows the two dimensional experimental and theoretical $sM(s, \phi)$ -patterns for $C_2F_4I_2$ (eq. 4.8). The acquisition time to record the experimental pattern was 200 min. The dark area in the experimental part is the shadow of the beam stop (compare fig. 4.4 b)). The experimental part is folded along the image diagonal (left) to be comparable to the theoretical pattern (right). The theoretical part is calculated using the theory presented in section 4.2 with the expression for the isotropic molecular intensity (eq. 4.6). Structural parameters are taken from the literature [95]. As expected, the diffraction pattern is isotropic due to the random orientation of the molecules in the gas jet. To be converted into a one dimensional curve the two dimensional molecular intensity can therefore be

azimuthally averaged according to

$$I_{\text{mol}}(s) = \frac{1}{2\pi s} \int_0^{2\pi} I_{\text{mol}}(s, \phi) d\phi. \quad (4.14)$$

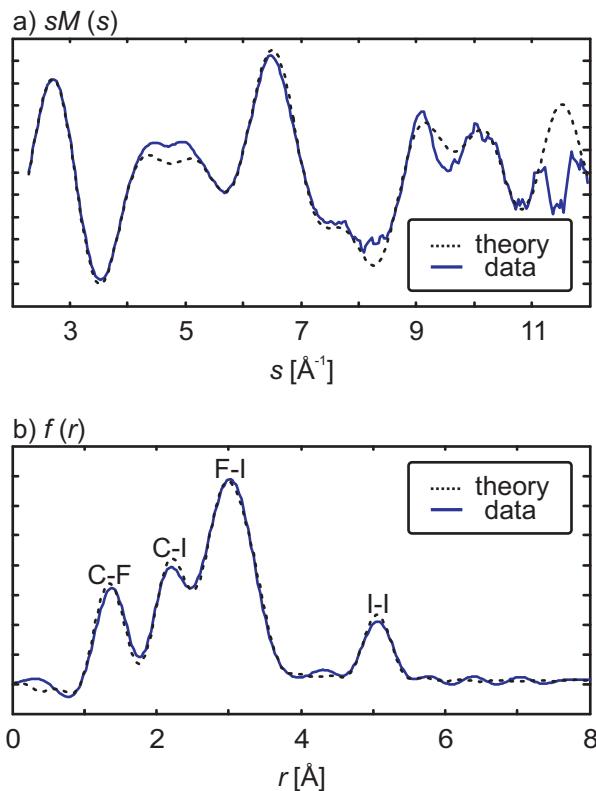


Figure 4.7.: a) Azimuthally averaged sM functions for $\text{C}_2\text{F}_4\text{I}_2$, experimental (blue line) and theoretical (red line). b) Corresponding radial distribution functions $f(r)$, experimental (blue line) and theoretical (red line). The dominant contributions to the peaks are labeled for the theoretical curve.

Figure 4.7 a) shows the azimuthally averaged $sM(s)$ curves. The experimental $sM(s)$ agrees very well with the theoretical prediction (calculated as in fig. 4.6) and results published previously [23, 95] up to a value of $s \approx 11 \text{ \AA}^{-1}$. For larger scattering angles the signal is too weak and drops below the noise level. A higher s -range could be accessed by increasing the sensitivity of the detector.

Figure 4.7 b) shows the radial distribution curve $f(r)$ obtained from the theoretical curve in fig. 4.7 a) using eq. 4.9. For the calculation, the damping constant k_d was set to $k_d = 0.12 \text{ \AA}^2$. Some of the inter-atomic distances which contribute

dominantly to the peaks are indicated, see for example the peak at 5 Å, which corresponds to the I–I distance in the anti-conformer. Due to the finite s -range accessible some of the peaks corresponding to different internuclear distances overlap. These results demonstrate very clearly, that due to the random orientation of the molecules in the gas jet, only 1D information about the molecular structure is accessible. From the reconstructed $f(r)$ function only the inter-atomic distances can be recovered, not the bond angles. This information is sufficient to fully reconstruct simple molecules, but the reconstruction gets more and more difficult with increasing complexity of the molecules.

4.4.2. Time-resolved electron diffraction

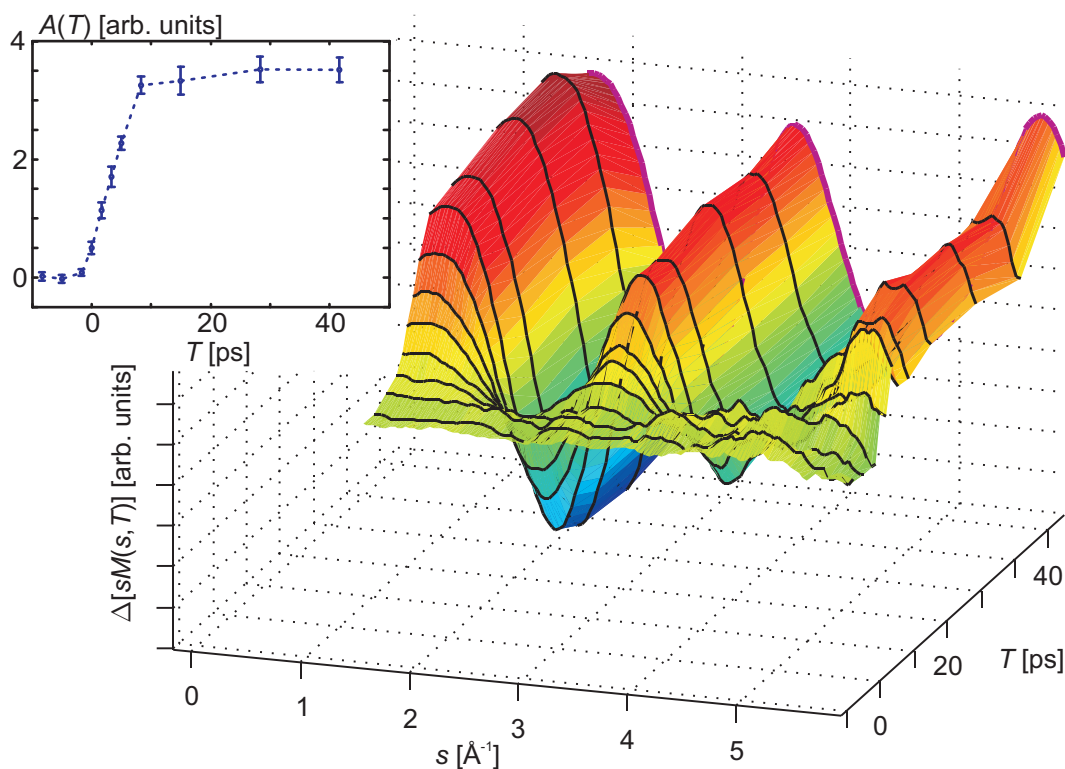


Figure 4.8.: Time resolved azimuthally averaged $\Delta[sM(s, T)]$ -curves. The black curves represent measurements for different time delays. The curve displayed in the back (magenta) is the theoretical $\Delta[sM(T = \infty)]$. Inset: Signal amplitude $A(T)$ versus time. The error bars represent the statistical fluctuations between the different images corresponding to each time step.

In this section the results of the time-resolved diffraction experiments are presented. In the time-resolved experiments diffraction patterns $\Delta [sM(s, \phi, T)]$ for different time delays between the laser and electron pulses are recorded. According to eq. 4.11 a diffraction pattern which is taken before the laser interacted with the molecules is subtracted from the diffraction patterns at certain time delays. For each time-delay 12 to 16 diffraction patterns are recorded with an integration time of 5 minutes each.

To remove the experimental background, background images are recorded interspaced with the diffraction images. These background images are taken under the same conditions as the diffraction images but without the gas jet. The background image is then subtracted from each diffraction image. Unusable pixels are removed from each image, i.e. the area behind the beam stop, the area outside of the fiber taper connected to the CCD-chip and pixels with very high absolute value (pixels that are defective or are hit by background radiation). The resulting images are denoised using a Wiener filter [96].

The two dimensional diffraction patterns ($\Delta [sM(s, \phi, T)]$) can be converted to one dimensional curves ($\Delta [sM(s, T)]$) by azimuthally averaging the whole image according to eq. 4.14. The resulting curves are shown in fig. 4.8. The zero of time is defined as the first time step where changes are observed.

For a quantitative analysis of the temporal evolution the time-dependent azimuthally averaged $\Delta [sM(s, T)]$ -curves are approximated as

$$\Delta [sM(s, T)] = A(T) \times \Delta [sM_{\text{Theory}}(s)]. \quad (4.15)$$

This approximation is used to fit the experimental data for the signal amplitude $A(T)$. The fitting is restricted to a limited range of s ($2.2 < s < 6.2$), where the changes due to the loss of the first and the second iodine atom result in very similar patterns. It is thus a good approximation to capture the temporal evolution with $A(T)$. The inset in fig. 4.8 shows $A(T)$ as a function of time. The error bars show the statistical fluctuations between the different images corresponding to each time step. From the growth of the dissociation signal in the experimental results a time constant of 4 ps is measured for the first step of the reaction, which agrees well with previous UED results [50]. This value is limited by the response time of the instrument, and is close to the calculated value of 3 ps (see section 4.3.1).

The fraction of dissociated molecules in the experiments was found to be 1/3 from best agreement between experiment and theory. The magenta curve in fig. 4.8 is the theoretical $\Delta[sM]$ after the reaction is completed (it is assumed that all the intermediates have been fragmented to C_2F_4). The curve is calculated using eq. 4.11 and the isotropic molecular intensity (using eq. 4.6).

4.4.3. Time-resolved observation of transient alignment

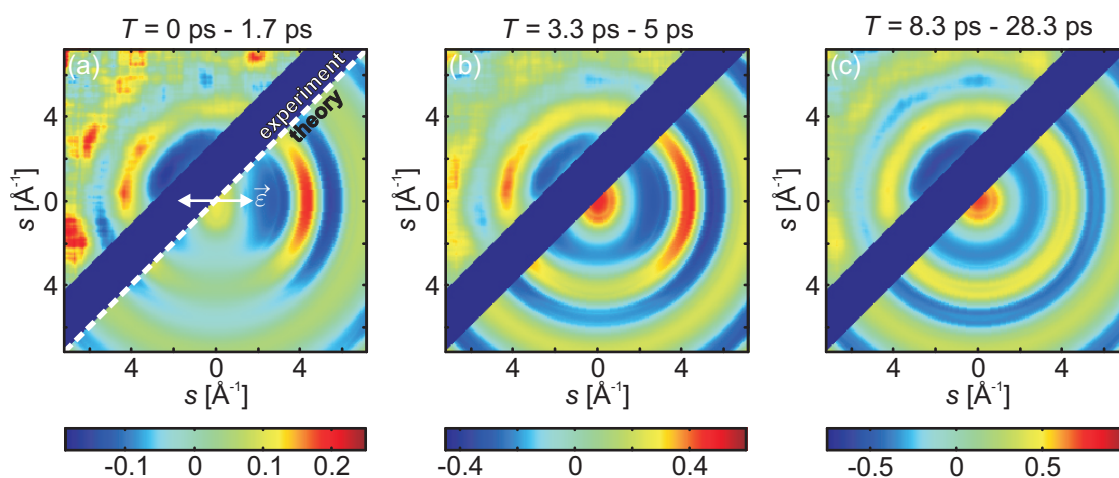


Figure 4.9.: 2D time-resolved diffraction patterns. a) $\Delta[sM(s, \phi, T)]$ close to zero delay of probe: the pattern is the result of averaging patterns recorded within the delay range of $T = 0$ ps and $T = 1.7$ ps. The white arrow indicates the direction of the laser polarization. The upper left half of the image displays the experimental data, while the lower right half shows the theoretical prediction. The dark region splitting the image is the shadow of the beam stop. b) $\Delta[sM(s, \phi, T)]$ averaged between $T = 3.3$ ps and $T = 5$ ps. c) $\Delta[sM(s, \phi, T)]$ averaged between $T = 8.3$ ps and $T = 28.3$ ps. (For larger images see appendix B.)

The following section concentrates on the investigation of the transient molecular alignment which is present in the early steps of the dissociation reaction. Figure 4.9 a) shows the two-dimensional $\Delta[sM(s, \phi, T)]$ close to $T = 0$. At this early time step the difference diffraction signal is small due to the instrument response time; however, the pattern shows significant anisotropy. The intensity of the image is higher along the direction of laser polarization, indicating that the dissociated molecules are aligned, with the missing C–I bond along the direction of laser polarization.

The theoretical part of this figure (calculated with eqs. (4.6) and (4.10) assuming that one-third of the molecules are dissociated to $\text{C}_2\text{F}_4\text{I}$) shows a similar pattern.

Figure 4.9 b) shows results at a later time when the anisotropy is weaker but still clearly visible. The corresponding theoretical pattern was calculated using a weighted average between the anisotropic pattern and the isotropic theory, assuming that $2/3$ of the molecular orientations have randomized. Figure 4.9 c) shows $\Delta[sM(s, \phi, T)]$ for later time steps. The pattern is now isotropic, i.e. the alignment is lost due to the molecular rotations. The theoretical pattern shown in fig. 4.9 c) is generated using the isotropic theory similar to the calculation of the theory curve shown in magenta in fig. 4.8.

To analyze the data quantitatively, the two-dimensional diffraction patterns are again converted into one-dimensional curves. For the investigation of the anisotropy however, the radial averaging (eq. 4.14) has now to be restricted to narrow pairs of cones aligned parallel and perpendicularly to the laser polarization. The averaging is performed in two pairs of cones according to

$$I_{\text{mol},\parallel}(s) = \frac{1}{2\pi s} \int_0^{2\pi} I_{\text{mol}}(s, \phi) \cos^{12}(\phi) d\phi. \quad (4.16)$$

The perpendicular case $I_{\text{mol},\perp}(s)$ is calculated similarly, replacing the cosine function in eq. 4.16 by a sine function. The $\cos^{12}(\phi)$ and $\sin^{12}(\phi)$ terms in the integral define the angular aperture and orientation of the cones and correspond to cones with an angular aperture of 38° . This value is chosen such that sufficient data for a good signal to noise ratio is included, while there is still a significant difference for different orientations. The cone-restricted molecular intensities $I_{\text{mol},\parallel}(s)$ and $I_{\text{mol},\perp}(s)$ yield corresponding $\Delta[sM_{\parallel}(s, T)]$, and $\Delta[sM_{\perp}(s, T)]$ functions. The results are shown in fig. 4.10. To display the noise level of the data the figure contains time steps before the dissociation ($T < 0$) which show no significant difference in the signal diffracted parallel and perpendicular to the laser polarization. The plots recorded within less than 2 ps following excitation clearly reveal a significant difference, indicating the anisotropy. The difference vanishes completely at $T > 8$ ps. The theory curves displayed in 4.10 are calculated from the two dimensional theory patterns shown in fig. 4.9 by the same procedure as the experimental curves.

Now, $\Delta[sM_{\parallel}(s, T)]$, and $\Delta[sM_{\perp}(s, T)]$ are used to determine the temporal evolution of the anisotropy. As an approximation corresponding scattering signal am-

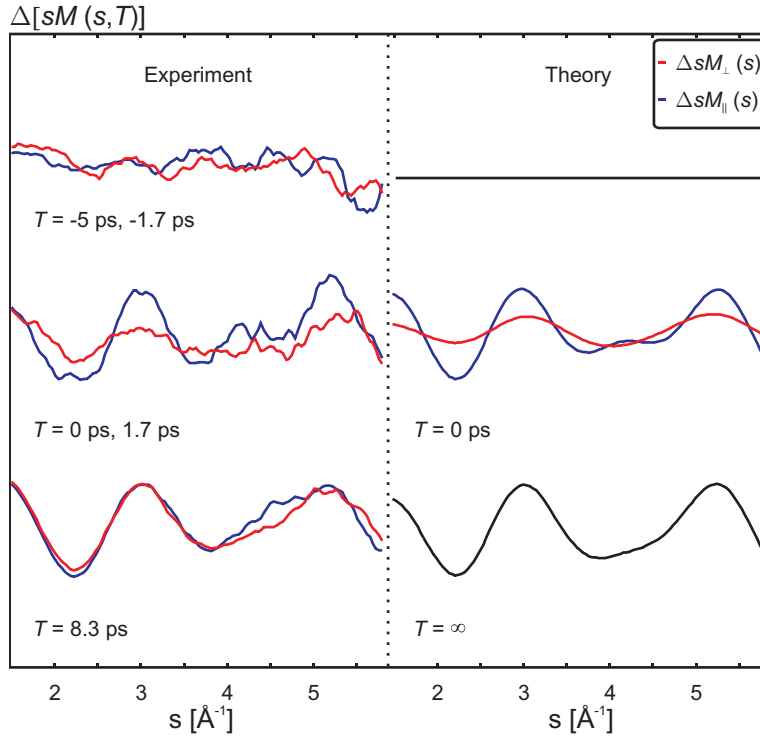


Figure 4.10.: Experiment: $\Delta[sM_{\parallel}(s)]$ and $\Delta[sM_{\perp}(s)]$ before time zero (averaged between $T = -5$ ps and $T = -1.7$ ps), $\Delta[sM_{\parallel}(s)]$ and $\Delta[sM_{\perp}(s)]$ close to time zero (averaged between $T = 0$ ps and $T = 1.7$ ps) and for late time steps (averaged between $T = 8.3$ ps and $T = 28.3$ ps). For visual clarity the curves for $T = -5$ ps, -1.7 ps, and for $T = 0$ ps, 1.7 ps are multiplied by a factor of 2.8. The curve at negative times shows the noise level of the data. Theory: corresponding theory curves

plitudes $A_{\parallel}(T)$ and $A_{\perp}(T)$ are defined within a limited s -range ($2.2 < s < 6.2$) where the s -dependencies of $\Delta[sM_{\parallel}(s, T)]$ and $\Delta[sM_{\perp}(s, T)]$ are similar. The time dependencies of $A_{\parallel}(T)$ and $A_{\perp}(T)$ are shown in fig. 4.11. The error bars shown in this figure display the statistical fluctuations between different images which are recorded for each time step. While the rise time is similar for $A_{\parallel}(T)$ and $A_{\perp}(T)$, there is a clear delay between the two curves, with the signal along the laser polarization ($A_{\parallel}(T)$) appearing first. This is due to the fact that the C_2F_4I radicals remain aligned immediately after the dissociation. Shortly thereafter, the alignment deteriorates due to the molecular rotation. Note that the delay between the two signals can be measured with a resolution well beyond the instrumental response time of 4 ps without deconvolution. After 8 ps, the orientations have fully

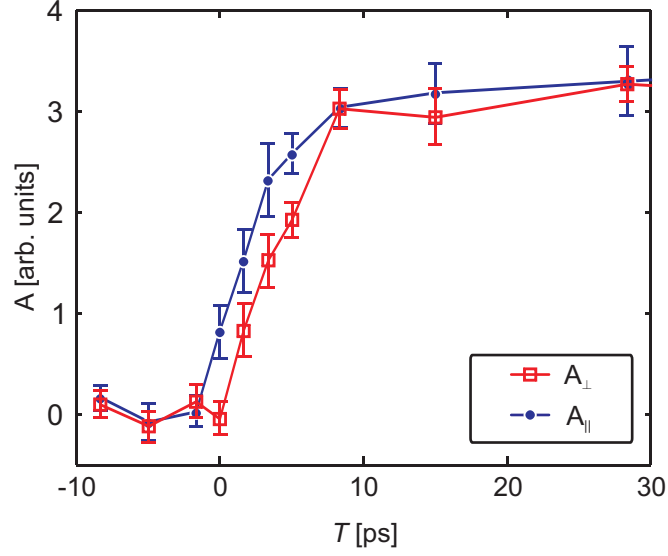


Figure 4.11.: A_{\parallel} and A_{\perp} measured parallel and perpendicular to the laser polarization respectively, as functions of delay time T . The error bars display the statistical fluctuations between different images recorded for each time step.

randomized and the difference between $A_{\parallel}(T)$ and $A_{\perp}(T)$ vanishes.

The anisotropy present in the diffraction patterns for the early time-steps can be additionally demonstrated by measuring the signal amplitude as a function of the azimuthal detector angle ϕ . For this purpose a signal amplitude $A_{\phi}(t, \phi)$ is defined in a single cone. This amplitude is determined similarly as $A_{\parallel}(T)$ and $A_{\perp}(T)$ but now with defining $I_{\text{mol},\phi}(s, \tilde{\phi})$ according to

$$I_{\text{mol},\phi}(s, \tilde{\phi}) = \begin{cases} \frac{1}{2\pi s} \int_0^{2\pi} I_{\text{mol}}(s, \phi) \cos^{19}(\phi - \tilde{\phi}) d\phi, & \text{if } \cos^{19}(\phi - \tilde{\phi}) \geq 0 \\ 0, & \text{else.} \end{cases} \quad (4.17)$$

The odd power of 19 defines a positive and a negative cone with apertures of 31° . By ignoring the negative contribution, the curve $I_{\text{mol},\phi}(s, \tilde{\phi})$ is the result from averaging the diffraction pattern in a single cone (which can be rotated around the diffraction pattern).

Figure 4.12 shows $A_{\phi}(T = 0 - 1.7 \text{ ps}, \phi)$ calculated from the 2D pattern shown in fig. 4.9 a). Again, error bars included in the figure show the statistical fluctuations between different images recorded for each time step. The data is in good agreement with the theoretical $\cos^2(\phi)$ dependence (shown by the black line). The minima of

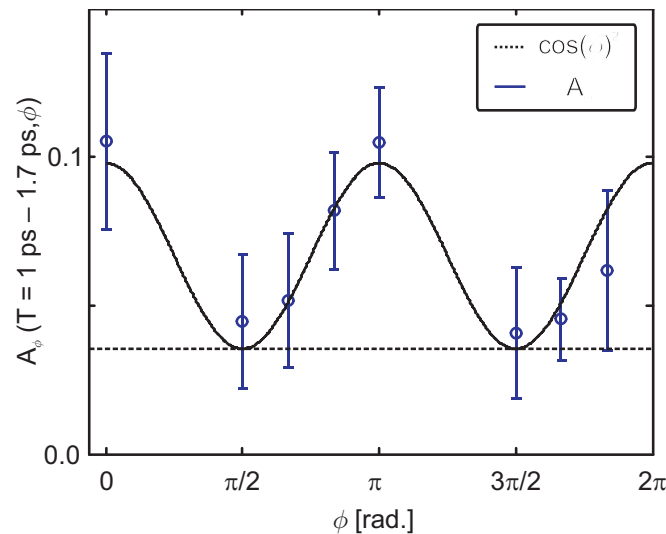


Figure 4.12.: Signal amplitude $A_\phi(T = 1 - 1.7 \text{ ps}, \phi)$ as function of the azimuthal detector angle ϕ . The black line shows a theoretical $\cos(\phi)^2$ -dependence. The gaps in the data are due to the beam block. The minima of A_ϕ do not drop to zero because the orientations of some molecules has already randomized.

A_ϕ do not drop to zero because the orientation of some of the molecules has already randomized.

Finally, the anisotropy is quantified using the following definition (fig. 4.13)):

$$\delta(T) = \frac{A_{\parallel}(T) - A_{\perp}(T)}{A_{\parallel}(T) + A_{\perp}(T)}. \quad (4.18)$$

The time decay of the anisotropy parameter δ is displayed in fig. 4.13. The errorbars are determined as before. From an exponential fit to the data a dephasing time of the alignment of $2.6 \pm 1.2 \text{ ps}$ is measured. This is in good agreement with the value $t_d = 2.7 \text{ ps}$ calculated in section 4.3.2.

4.5. Conclusions

The results of the experiments discussed above demonstrate for the first time the feasibility of recording an UED pattern from transiently aligned molecules. The decay of the alignment was measured on a picosecond time scale. These results are a first important step towards 3D imaging of complicated molecular structures

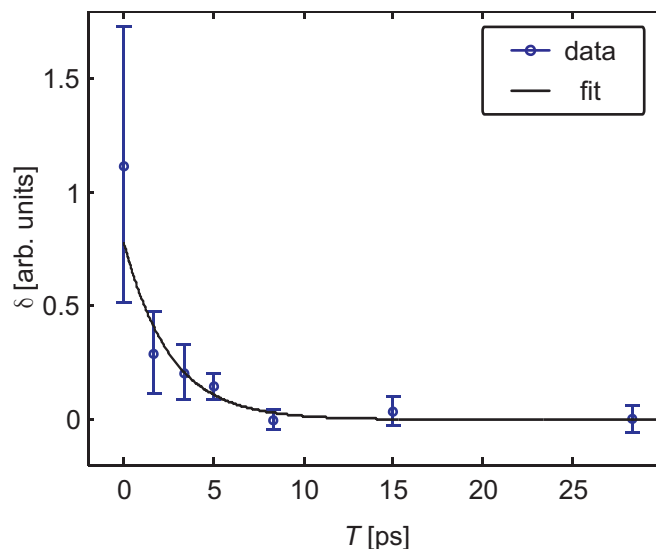


Figure 4.13.: Anisotropy parameter δ as a function of delay time T ; the black line shows an exponential fit to the data.

with electron diffraction or possibly using the new generation hard X-ray sources. Increasing the degree of alignment, combined with diffraction patterns corresponding to different projections of the molecule (using suitable algorithms [97]), will allow full 3D reconstruction of the structure even for more complex molecules. The method could also be applied to investigate ultrafast molecular dynamics in a field-free environment. Improving transient molecular alignment may be pursued by saturating the dissociation [98] or with active 1D [99] and even 3D alignment techniques [100, 101]. The temporal resolution could be further improved by compressing the electron pulses to few fs [102, 103]. This is necessary to make use of the optimum alignment which is present only at the instant of dissociation. The issue of shortening electron pulses is discussed in detail in the following chapter.

5. Single-electron source – from picoseconds to femtoseconds

One of the experimental limitations in the experiments presented in chapter 4 is the picosecond temporal resolution. With femtosecond resolution it would be possible to resolve the structural changes of the two step dissociation reaction in more detail. The molecular alignment which is strongest at the instant of dissociation could be observed closer to the optimum.

However, thousands of electrons per pulse have to be used for the acquisition of the diffraction patterns. At kHz repetition rate, this is the lower limit to achieve realistic acquisition times. Because of the mutual repulsion (“space charge”) of the electrons in each pulse, the electron pulse durations in these experiments is limited to the ps-range.

The following chapter presents an approach reducing the electron pulse duration by eliminating space charge. The idea is to use only a few electrons or single electrons at MHz repetition rate instead of thousands of electrons at kHz repetition rate [20]. For this purpose the standard kHz femtosecond laser system is replaced by a high energy long cavity oscillator [25] operating at 2.7 MHz providing pulses with an energy of roughly half a microjoule.

When space charge is eliminated the main factor leading to temporal pulse broadening is the initial energy spread of the electrons at the moment of emission from the cathode. Due to this initial energy spread the electron pulse duration is given by [104]

$$\tau_e = 2.34 \frac{\sqrt{\Delta U_i}}{E_{acc}} \text{ ps.} \quad (5.1)$$

In this equation, ΔU_i is the initial energy spread of the electrons in eV and E_{acc} is the acceleration field in kV/mm. The initial energy spread can be reduced by tuning the laser photon energy to the bandgap of the photocathode material. Experiments using three different laser wavelengths to create the electron pulses indicate that femtosecond pulses are well achievable [105] using the third harmonic of a Ti:Sa laser at 267 nm. Experiments investigating the energy dependence of the photoemission continuously varying the laser wavelength are in preparation [106].

From eq. 5.1 it is seen that the electron pulse duration can be reduced by increasing the acceleration field. Static acceleration fields as strong as 10 kV/mm have been demonstrated [107]. However, to achieve very high acceleration fields and to prevent vacuum breakdown, it is necessary to house the electron source in an ultra-high vacuum system. For the experiments presented in this chapter, a suitable system was designed and constructed (see appendix A).

5.1. Proposed method for measuring the duration of electron pulses by attosecond streaking

A key problem is to measure the duration of ultrashort electron pulses. Several methods have been investigated and applied for this purpose including streak cameras [108], interferometry of coherent transition radiation [108, 109], radio-frequency zero phasing [110], terahertz radiation diagnostics [111], electro-optic encoding [112] and ponderomotive interaction of a laser with the electron pulse [113]. None of these methods, however, has proved to be applicable in a wide range of parameters: Streak cameras and radio-frequency zero phasing cannot be used for pulses shorter than a few hundred fs. Coherent transition radiation, as well as terahertz radiation and electro-optic methods require a large number of electrons per pulse to provide sufficient signal, while the ponderomotive interaction requires high laser intensities and is limited by the duration of intense laser pulses. In this chapter a new method for measuring the duration of electron pulses is presented which holds promise for being applicable to an unprecedentedly broad range of parameters: from femtoseconds to attoseconds, from electron volts to mega-electron volts, and from millions of electrons per bunch to single-electron pulses. It is similar to that known as the “attosecond-streak camera” [114, 115], an ingenious tool for investigating ultrafast

processes. So far, attosecond streaking has been used for measurement of soft X-ray pulses, characterizing laser fields and investigating ultrafast processes in atoms [1, 116].

5.1.1. Theoretical basics

The underlying idea is based on the fact that an electron pulse impinging on a solid target will generate, through impact ionization, a pulse of Auger electrons with duration equal to that of the incident pulse convolved with the duration of the Auger decay. As discussed below, Auger decay can be much faster than the duration of the pulses and is easily accounted for. The energy of an Auger electron created in the presence of a laser field is altered by the field. The energy shift ΔU depends on the phase ϕ of the electric field $E = E_0 \sin(\phi)$ at which the electron is released and the initial energy U_0 of the Auger electron, according to the classical formula [114]

$$\Delta U = \sqrt{8U_0U_p} \cos(\phi) \cos(\Theta). \quad (5.2)$$

In this equation, Θ is the angle between the velocity of the emitted electrons and the laser polarization and $U_p = E_0^2/4\omega_L^2$ is the ponderomotive potential (here given in atomic units) of the laser field, where E_0 is the maximum amplitude and ω_L the frequency of the laser field, respectively. Equation 5.2 applies to linearly polarized laser pulses; it shows that even with relatively low laser intensity (corresponding to a small ponderomotive potential) one can obtain quite appreciable energy shifts, which for $U_0 > U_p$ can be much larger than the laser ponderomotive potential. Calculation of the spectra following a quantum-mechanical approach yields side bands spaced by the laser photon energy, with a maximal energy shift given by eq. 5.2. Such spectra have been seen in the so-called laser-assisted Auger decay [117]. The expected spectrum can be calculated within a quantum mechanical model similar to the one describing laser-assisted Auger decay initiated by the absorption of an energetic photon [5, 118]. First, only those collisions of electrons with atoms that occurred at a certain moment t are considered. Without the streaking field,

the energy distribution of Auger electrons is given by [119, 81]

$$\tilde{I}(U, t) \propto \frac{1}{\sqrt{U}} \left| \int_t^\infty M(\sqrt{2U}) \exp \left[- \int_t^{t'} \left(\frac{\Gamma}{2} + i(U - U_0) \right) d\tau \right] dt' \right|^2, \quad (5.3)$$

where Γ is the rate of the Auger decay and $M(p)$ is the bound-continuum coupling matrix element as a function of the free electron momentum $p = \sqrt{2U}$. This model neglects the post-collision interactions, as well as the interaction of the Auger electron with the field created by the electron pulse. Here it is also assumed that the collision time t is well-defined, which is a valid assumption as long as the interaction time between a projectile and an atom is much smaller than the Auger decay time $1/\Gamma$. Under these assumptions, the interaction of a free electron with a homogeneous time-dependent streaking field can be described as [115]

$$\begin{aligned} \tilde{I}(U, t) \propto \frac{1}{\sqrt{U}} & \left| \int_t^\infty M(\sqrt{2U} + A(t')) \right. \\ & \left. \exp \left[-\frac{\Gamma}{2}(t' - t) - iU_0 t' + \frac{i}{2} \int_0^{t'} [\sqrt{2U} + A(\tau)]^2 d\tau \right] dt' \right|^2. \end{aligned} \quad (5.4)$$

Here, $A(\tau)$ is defined as

$$A(\tau) = \int_\tau^\infty E(\tau') d\tau' \quad (5.5)$$

and it is assumed that the interaction of the streaking field with bound electrons does not affect Auger spectra. So far, a single electron hitting an atom at a moment t has been considered. To evaluate the Auger spectrum formed by a pulse of electrons with a finite duration, it is now assumed that the probability to initiate the Auger decay in a given atom is proportional to the instantaneous flux in the electron pulse $I_e(t)$. Denoting the relative delay between the laser and the electron pulses as T , the final expression for Auger spectra dressed by the streaking field is obtained as

$$I(U, T) \propto \int_{-\infty}^\infty I_e(t - T) \tilde{I}(U, t) dt. \quad (5.6)$$

Different atoms – hit by different electrons, emit Auger wave packets independently. Therefore, deriving eq. 5.6, contributions from atoms that experienced collisions at different moments are added incoherently.

5.1.2. Proposed experiment

The above described change in the Auger line in the presence of the laser field can be used for measuring electron pulse duration in an arrangement conceptually shown in fig. 5.1: The ultrashort electron pulse impinges on a suitable material generating

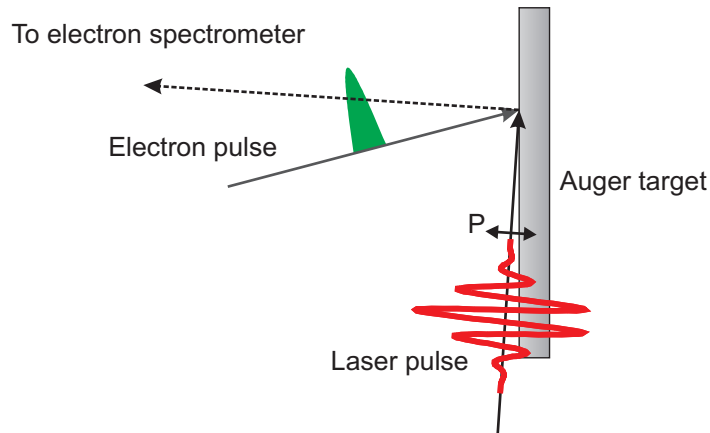


Figure 5.1.: Basic arrangement of electron pulse duration measurement. P indicates the direction of polarization of the laser pulse.

Auger electrons. A short laser pulse is then focused at grazing incidence on the surface of the solid, its polarization direction being coincident with the direction in which the Auger electrons escaping from the target are detected. An appropriate choice of the angles of the electron and laser beams with respect to the surface prevents a deterioration of the temporal resolution due to geometrical effects. The angles must be chosen such that the relative delay between the pulses is constant along the target surface; for example, for relativistic electrons, a collinear geometry is optimal, while for 20 keV electrons the optimum angle is approximately 15° with respect to the surface normal (for grazing incidence of the laser). A time-of-flight electron spectrometer then records electron spectra for different time delays between laser and electron pulses. Overlaying a sufficient number of spectra with different delays generates a “streaked” spectrum from which the electron pulse duration can be deduced.

5.1.3. Numerical results

In the following, results of the calculations for two different cases, viz., relatively long laser and electron pulses (of order 100 fs), and very short pulses, viz., a few-cycle laser pulse with an as electron pulse are presented. These very different parameter ranges illustrate the broad applicability of the method. In the long-pulse case (electron pulse duration longer than the laser cycle), the electron spectrum at any particular delay will be broadened, since the electron energies are swept through a large number of laser cycles. In the short-pulse regime (electron pulse duration shorter than laser cycle), the electron spectrum will be broadened and shifted. Note that an Auger line with an appropriate decay time must be chosen for optimum results in the two regimes. The spectrum is independent of the energy of the incident electron pulse. The energy does, however, affect the cross section for generating Auger electrons, as discussed below in more detail.

The following parameters were used for the calculation of the long-pulse case: Electron pulse duration 100 fs, laser pulse duration 50 fs. Both pulses were assumed to be Gaussian in time. For the Auger transition, the oxygen KLL line with an energy of 500 eV is chosen. The natural width of this line is 0.15 eV corresponding to a decay time of 4.4 fs. The laser intensity is assumed to be 1.6×10^{12} W/cm² at a wavelength of 800 nm, corresponding to a ponderomotive potential $U_p = 0.1$ eV. The maximum energy shift, calculated from eq. 5.2, is 20 eV. Figure 5.2 shows the oxygen line and its broadening calculated using eq. 5.2 and eq. 5.6. The electron spectrum is seen to be substantially altered during the period in which the two pulses overlap: according to the quantum mechanical formula (5.6) the intensity of the main Auger line is reduced to 14% and side bands spaced by the photon energy appear on both sides, extending up to the maximum energy shift, while the classical calculation predicts a decrease of the main peak to 5% along with a continuous broadening of the line. Even though the main Auger line is still quite prominent in the spectrum, measurement of the number of the energy-shifted electrons should be readily feasible, yielding the cross-correlation signal between the envelopes of the laser and the electron pulses. Apart from the expected side bands, the quantum mechanical approach also shows a modulation in the amplitude of the side bands. The modulation arises from interference between different components of the electron wave packet emitted with the same energy at the rising and falling

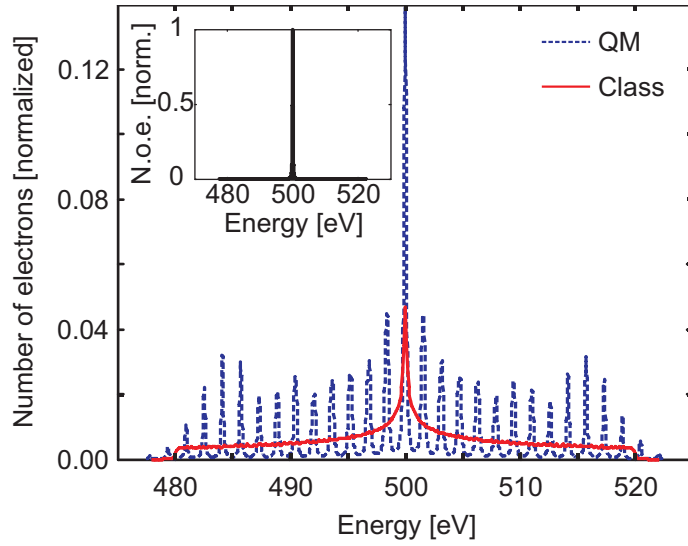


Figure 5.2.: Electron spectra for a long-pulse case at delay time $T = 0$, i.e., when electron and laser pulse maxima coincide. The dashed blue curve (QM) shows the result of a quantum mechanical calculation following eq. 5.6, while the red solid curve (Class) shows the spectrum calculated (classically) using eq. 5.2. The inset shows the original line without laser. The total number of electrons is the same for all curves.

part of the laser cycle. The streaked spectrum, generated by plotting the spectra as functions of delay between laser and electron pulse, is shown in fig. 5.3 a). As the overlap between the two pulses increases, more and more side bands appear on both sides of the main Auger line. From such a correlation measurement, the duration of the electron pulse can easily be retrieved if the laser pulse envelope is known. 5.6.

The short-pulse case (fig. 5.3 b)) is calculated with the following parameters: electron pulse duration 500 as, a few-cycle cosine-laser pulse with duration of 4 fs at a wavelength of 800 nm. Again, a laser intensity of 1.6×10^{12} W/cm², i.e. $U_p = 0.1$ eV, was assumed. Note that the laser pulse must be carrier-envelope stabilized, otherwise the temporal resolution would only be given by its pulse duration. For the Auger transition, the titanium KLL Auger line at 4.06 keV with a natural width of 0.94 eV and correspondingly a decay time of 702 as is chosen. Equation 5.2 predicts for the maximum energy shift of the electrons a value of 57 eV. Features quite different from the long-pulse case are now observed: The main change in the spectrum is an energy shift which occurs in synchronism with the laser vector

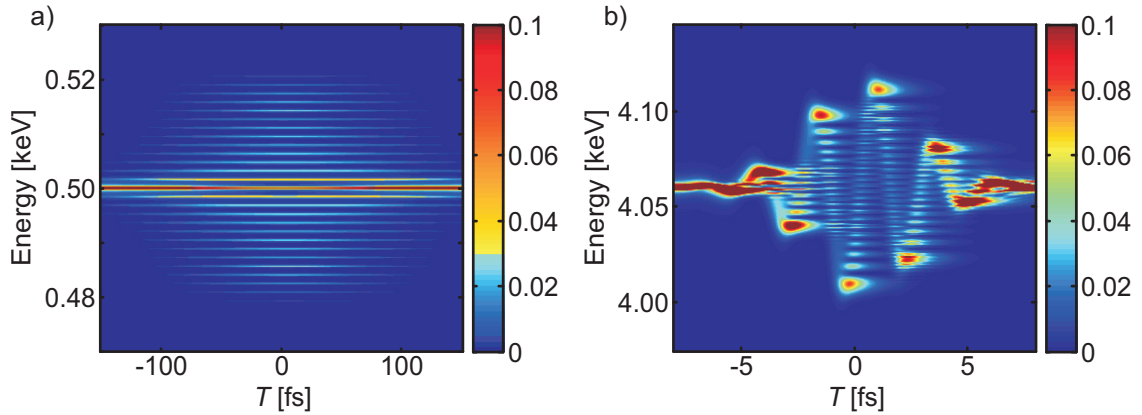


Figure 5.3.: Calculated electron spectra. a) Spectrum for long-pulse conditions. Electron pulse duration 100 fs; laser pulse duration 50 fs. Auger line applied oxygen KLL at 500 eV. b) Spectrum for short-pulse conditions as a function of time delay. Electron pulse duration 500 as; laser pulse duration 5 fs. Auger line Ti KLL at 4.06 keV. Time zero is defined as the temporal delay at which both pulse maxima coincide. The color scale is normalized to the intensity of the original Auger line.

potential. Slight broadening results from the combined smearing of electron pulse duration and Auger decay time over the laser cycle.

5.1.4. Experimental considerations

For successful realization of the experiment, the number of Auger electrons generated must be high enough to produce a spectrum in an appreciable amount of time. The electron yield η_{el} , defined as the number of Auger electrons per pulse electron can be calculated by the expression

$$\eta_{el} = (1 - \eta_f)\sigma_K N_0 d_{esc} \quad (5.7)$$

where η_f is the fluorescence yield of the Auger line, σ_K is the cross-section for K-hole generation by the incoming electrons, N_0 is the number density of the solid and d_{esc} is the escape depth of the Auger electrons from the solid. The fluorescence yields for oxygen and titanium are given by 0.0083 and 0.214, respectively [120]. For nonrelativistic electrons, the calculated cross-section for generating a K hole are $2.6 \times 10^{-20} \text{ cm}^2$ and $1.06 \times 10^{-21} \text{ cm}^2$ for oxygen and titanium respectively

[121]. The escape depth can be taken from the universal mean-free-path curve for solids (see, for example, [122]), and is 0.9 nm at 500 eV and about 3 nm at 4 keV. Using these parameters we obtain $\eta_{el,O} = 1.7 \times 10^{-4}$ and $\eta_{el,Ti} = 1.4 \times 10^{-5}$. For the calculation of $\eta_{el,O}$, the number density of oxygen in sapphire was used. These numbers show that with an electron source running at 1,000 electrons per pulse at a kHz repetition rate or with 1 electron per pulse at a MHz repetition rate, and an electron spectrometer with an acceptance angle of about 1 sterad, a complete spectrum covering a range of $U_0 \pm \Delta U$ can be recorded in less than an hour (although for cross-correlation experiment a smaller range could be sufficient).

In order for the method to work over a wide range of electron energies, the cross-section for generating a K hole must be sufficiently large. In the energy range between keV and GeV, the cross-section has a minimum around MeV energies [123, 124]. Even at the lowest value the cross-section is comparable to the value used in the above example, thus the method is expected to work from keV to GeV energies. The minimum energy for the electron pulse is given by the energy necessary to create the K hole (just slightly above the energy of the chosen Auger line). For the limits of temporal resolution also the effect of the finite escape depth has been considered, but is not expected to be significant, given that the escape time (over 1 mean free path) will be below 100 as.

5.2. The MHz-electron source

In order to implement the measurement scheme described in the previous section, an ultra-high vacuum chamber was designed and constructed (appendix A). The ultra-high vacuum (typically $\approx 10^{-9}$ mbar in the present chamber) is required to reach the maximum possible static field strength to accelerate the electron bunches (see eq. 5.1). Additionally, to allow for more stable operation under high field conditions, a special design for the cathode is used: Instead of a flat quartz window a quartz lens is coated with a 40 nm gold layer. In this configuration only a small area is subject to the highest field strength and especially the edges of the cathode are farther away from the anode preventing vacuum breakdown. In the present system it was already possible to achieve a field strength of 8 kV/mm. This is already close to the maximum value of 10 kV/mm which has been demonstrated

[107].

To perform the pulse duration measurement it is important to find a feasible experimental method to overlap laser and electron pulses spatially and temporally. This is more difficult for the MHz-laser system as compared to the kHz-laser system used in chapters 3 and 4 because of the low laser pulse energy in the case of the MHz-laser system ($U_{\text{Pulse}}^{\text{max}} \approx 400$ nJ). The difference in the velocities of light and electron pulses adds another complication. In the experiments presented below, a moderate acceleration voltage of 8 kV is used, resulting in a factor ≈ 6 in pulse velocities. The following section addresses the experimental alignment of the spatio-temporal pulse overlap of the electron and laser pulses.

5.3. Time-resolved visualization of photoemission from a solid

In this section a method is demonstrated to experimentally establish the spatial and temporal overlap of electron and laser pulses. The presented method is based on the deflection of the beam electrons by fields generated by a cloud of electrons photo-emitted from a copper surface. Additionally these experiments allow to study the photoemission process itself. Images of the photoemitted electron cloud can be recorded in pump-probe experiments with a resolution of only a few hundreds of femtoseconds.

Intense generation of photoelectrons can occur in 1-, 2- or multiphoton photoemission [125]. The study of these effects allows extending the knowledge of ultrafast changes of surface states and gaining new insight in the dynamics of electron motion. Quite a number of studies have already addressed various aspects of photoemission with fs laser pulses. The propagation dynamics of femtosecond electron packets has been studied theoretically [126, 127] and experimentally [128]. Above threshold photoemission in solids has been demonstrated [129]. Light phase sensitive photoemission has been reported [130] and this effect has been predicted to make possible the determination of the carrier-envelope phase of few-fs laser pulses [131]. Moreover the emission of sub-keV electron pulses mediated by surface plasmons has been reported and control of this effect by the carrier envelope phase has been predicted [132, 133]. Electrons emitted from nanoparticles have been used as a tool

for the investigation of optical near fields [134]. The laser-assisted photoelectric effect has been demonstrated [135] and used to study ultrafast electronic processes at surfaces [136, 137]. Finally, using soft X-rays, photoemission from inner shells has been studied on an attosecond time scale [6].

The main technique used in all of the above studies has been electron spectroscopy. The experiments presented in this section constitute a new method of investigation, capable of directly visualizing the dynamics of electrons emitted from a solid by their effect on a high-energy electron pulse.

A beam of 8 keV electrons in a pulse with a duration of about 300 fs is passed over the electron cloud photoemitted by a 50 fs laser pulse. The electric fields generated by this charge deflect electrons in the beam and thus project the distribution of charge on the detector. The short laser and electron pulse durations allow observing the emission of the electrons and their subsequent motion on a fs time scale.

The technique is similar to the investigation of the OFI-plasmas of chapter 3. However, the present study utilizes laser energies which are about an order of magnitude below the threshold for plasma formation. The temporal evolution of photoelectrons is seen to occur on a sub-ps time scale in contrast to plasma dynamics which involves a time scale of a few ps.

5.3.1. Experimental setup

The experimental setup is shown in fig. 5.4. The laser pulses are generated using a long cavity oscillator [25]. They have a central wavelength of 800 nm, duration of 100 fs, an energy of 260 nJ at a repetition rate of 2.7 MHz. A dielectric beam splitter is used to separate a weaker beam from the main laser path. This beam is converted into the third harmonic centered at 266 nm. The resulting UV-beam passes a motorized delay stage, after which it is expanded and then focused into a vacuum chamber at the surface of a gold photocathode. The cathode consists of a 40 nm gold layer coated on a 1 mm thick quartz lens ($f=100$ mm, plano-convex). Electron pulses are created via the photoelectric effect and accelerated by a static voltage ($U_{\text{acc}} = 8$ kV over 2 mm) towards a grounded copper anode with a 200 μm hole. By means of a magnetic solenoid lens they are focused to a 20 μm spot before the target. To facilitate locating the region of photoemission a thin copper foil with a 100 μm hole was used as the target. After expanding through the hole the pulses

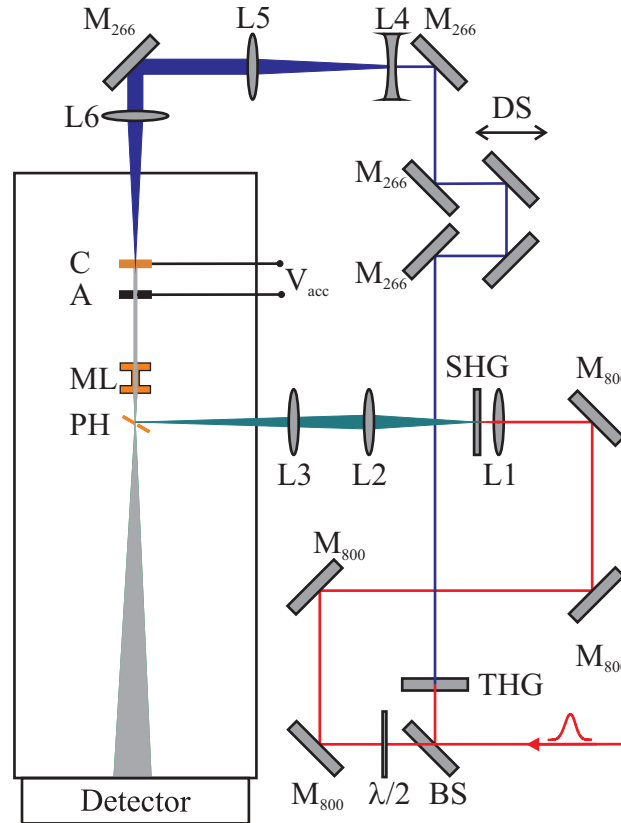


Figure 5.4.: Experimental setup: BS: beam splitter; M_{800} : dielectric mirror for 800 nm; THG: third harmonic generation; L1: lens ($f = 100$ mm); SHG: second harmonic generation (residual fundamental light is suppressed with a 1 mm BG39 color filter); L2 lens ($f = 400$ mm); L3 lens ($f = 300$ mm); M_{266} : dielectric mirror for 266 nm; DS: motorized delay stage; L4: lens ($f = 50$ mm); L5: lens ($f = 200$ mm); L6: lens ($f = 500$ mm); C: gold photocathode; V_{acc} : acceleration voltage (8 kV); A: copper anode with $100 \mu\text{m}$ hole; ML: magnetic lens; PH: copper pinhole ($100 \mu\text{m}$); Detector: multi channel plate detector (MCP) fiber coupled to CCD chip.

propagate by 23.9 cm to the detector. The detector is a multi channel plate (MCP) detector, which is fiber coupled to a CCD chip. Due to the expanding electron beam the image of the hole is magnified by a factor of 60 on the detector. This magnification is a key feature of the experiment because it allows for the detection of spatially small effects.

Because of the high sensitivity of the MCP-detector it is possible to detect single-

electrons. Therefore the MCP-detector can be calibrated directly to the number of electrons per pulse (at an energy of 8 keV, an electron generates on average ≈ 580 counts on the detector).

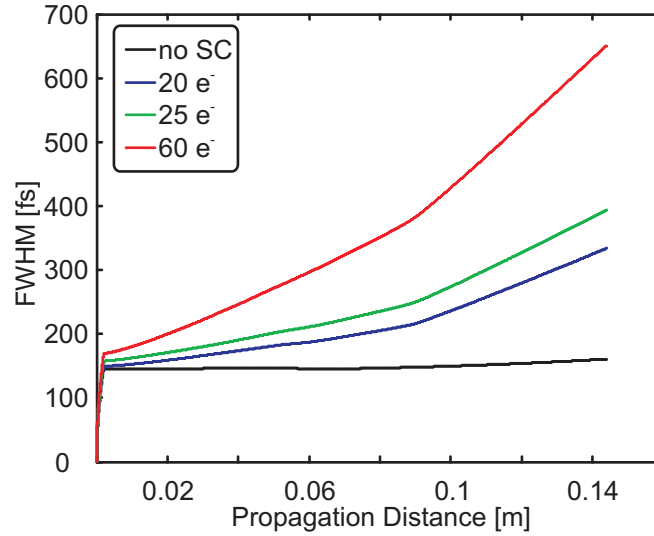


Figure 5.5.: GPT [78] calculations for the current experiment: An initial energy spread of 0.1 eV is assumed. The acceleration field is 4 kV/mm. The laser pulse duration is 100 fs and the spot on the cathode is 10 μm . The magnetic lens was included in the calculation. The abrupt change in the graphs just before 0.1 m is a temporal broadening caused by path differences which are introduced by the magnetic lens.

Figure 5.5 shows results of GPT-simulations of the electron pulse duration as a function of the propagation distance. The simulation is based on the experimental parameters of the present experimental system. An initial energy of the electrons emitted from the photocathode of 0.1 eV was taken into account. This energy is in good agreement with results of previous experiments [105, 108]. The acceleration field was included as 4 kV/mm, the laser pulse duration on the photocathode is 100 fs and the laser spot on the cathode is 10 μm . The solenoid lens to focus the electrons onto the target is taken into account as well. Due to different pathes which are introduced by the magnetic lens the pulse duration broadens more strongly. This is seen as an abrupt change in the graphs just before 0.1 m. The simulations show that even for the present quite relaxed experimental conditions, such as a relatively weak acceleration field and few tens of electrons per pulse, the pulse duration is well in the femtosecond regime.

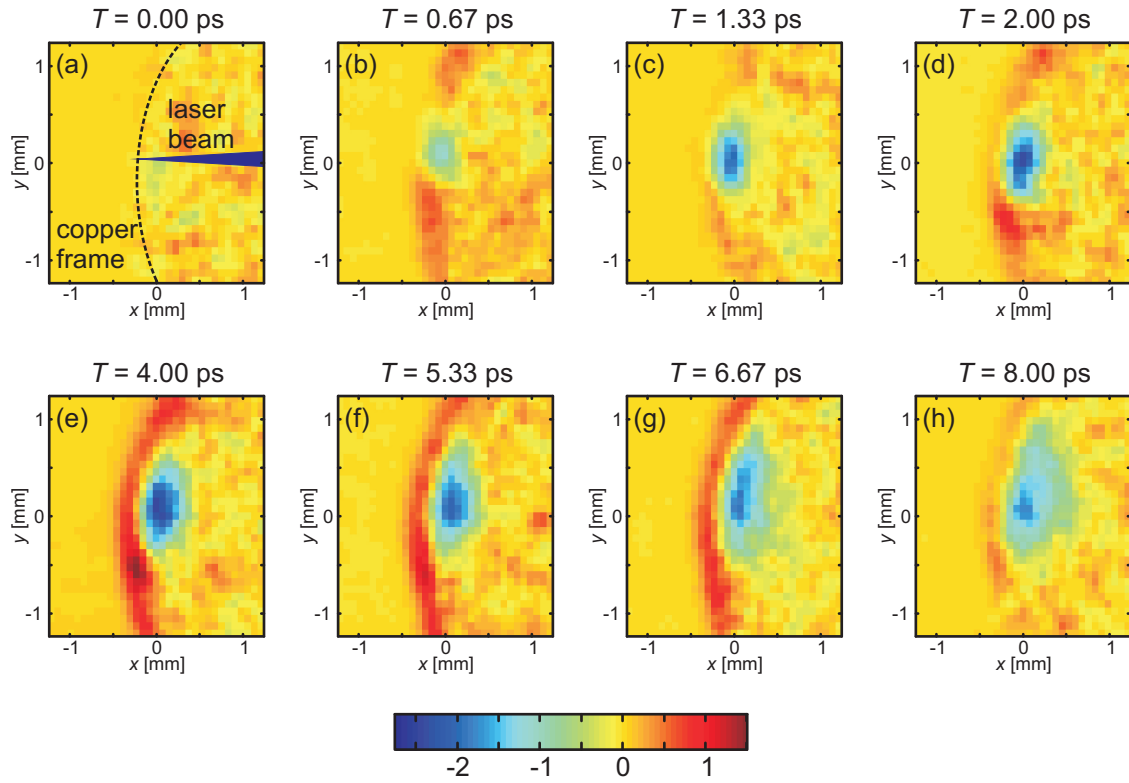


Figure 5.6.: Pump-probe images tracking the photoelectrons expanding from the surface. a)-h): Changes in the probe-electron beam due to changing photoelectron distribution as a function of the time delay T between the electron and laser pulses. The geometry is shown as an overlay in a). The laser is incident from the right with a polarization perpendicular to the image plane. The color mapping represents the number of electron counts in arbitrary units. The pump-laser wavelength is 400 nm.

The laser pulses traversing the beam splitter are converted into the second harmonic centered at 400 nm. They are expanded by a telescope and then focused onto the edge of the hole in the copper frame (see fig. 5.6a)). The calculated diameter of the beam on the target surface is 10 μm . During the experiments the laser pulse energy is varied using neutral density filters and the polarization is rotated by means of a half wave plate. In part of the experiments the fundamental laser wavelength is used (see fig. 5.7)

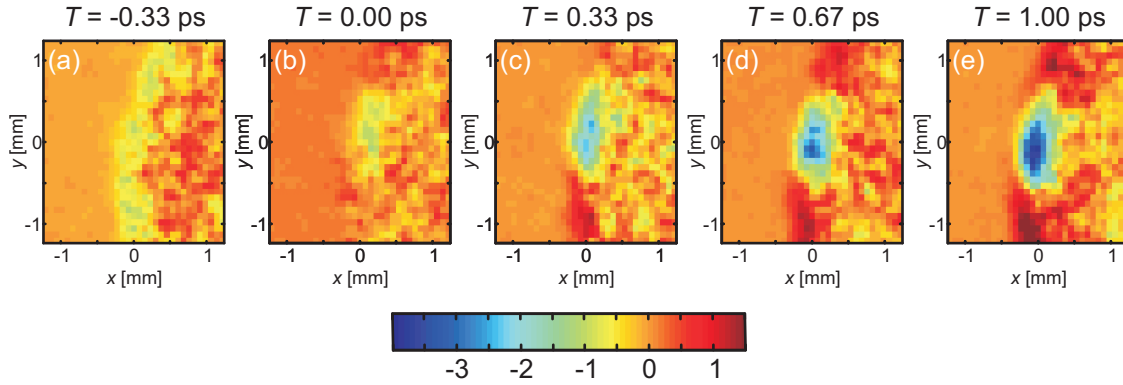


Figure 5.7.: Pump-probe images tracking the photoelectrons expanding from the surface for a pump wavelength of 800 nm. The pump-laser polarization is linear, perpendicular to the plane of the detector. The pump-laser wavelength is 800 nm.

5.3.2. Experimental results

Figure 5.6 shows images for different time delays T between electron and laser pulses. For these runs the laser pulse energy is 37 nJ, and the pulses were linearly polarized with the polarization direction perpendicular to the plane of the detector. The pump-laser wavelength is 400 nm. Figure 5.6 a) displays the geometry of the experiment. The edge of the copper hole is shown as a dashed line. The laser is incident from the right of the image and focused onto the edge. The delay $T = 0$ between laser and electron pulses is defined as the delay where first small changes become visible. Figures 5.6 a)-d) show results for a time step of 660 fs.

Figure 5.6 e)-h) shows results for bigger time steps of 2 ps. All images are difference images using recordings at negative time delay T (i.e. electron pulse ahead of the laser pulse) as a reference. The exposure time for each time step is 10 s.

The photoemitted electron cloud has the effect of generating a hole in the interrogating beam. This is due to the deflection of the beam electrons by the fields of the cloud. It is seen that for short time delay the hole in the electron beam rapidly develops indicating the fast expansion of the photoemitted electron cloud. With increasing delay the hole generated by the cloud is seen to become more shallow. The fraction of deflected electrons increases to a maximum of 36 % around $T = 3.5$ ps and then decreases again while the depleted region keeps expanding. The

expansion velocity can be measured from the images. It is 9×10^5 m/s.

Figure 5.7 shows results with the fundamental laser pulses at 800 nm focused on the copper frame. The laser intensity is 4.4×10^{11} W/cm². The laser polarization is the same as in fig. 5.6, i.e. perpendicular to the plane of the detector. In this case significant changes were observed for time steps as small as 330 fs. The number of beam electrons per pulse in this experiment is 30. Using the GPT-code [78], the electron pulse duration is calculated to be 390 fs. The measured expansion velocity of the edge is 8×10^5 m/s and the maximum electron depletion of 33.4 % is reached after 3.5 ps.

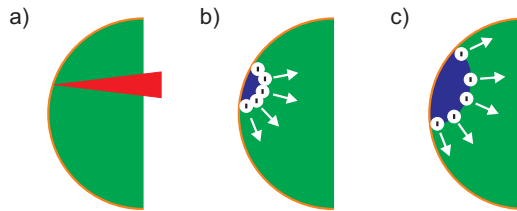


Figure 5.8.: Schematic illustration of the experimental results.

Figure 5.8 illustrates an interpretation of the experimental results. At a time delay $T = 0$ the laser impinges the target (the copper frame). Photoelectrons are emitted either via a three-photon process in the case of the fundamental laser (fig. 5.7) or a two-photon process in the case of the second harmonic (fig. 5.6). The photoelectrons expand away from the copper frame and the beam electrons are deflected in the resulting fields.

A question of fundamental interest to be addressed is if the image charge of the expanding electron cloud has to be taken into account to describe the features observed in the experiments. Ongoing numerical simulations address this question [30].

5.4. Conclusions

The experiments presented in the previous section are the first important step towards implementation of the pulse duration measurement using the streaking of the Auger line as presented in section 5.1. Additionally they have interesting physical implications. With the deflection of the probe electron beam it is possible

to directly visualize the process of photoemission. From the data it is possible to directly infer properties as the expansion velocity and the electron energy. By comparing the data to numerical simulations the underlying physical processes can be investigated quantitatively [30].

The presented experiments have a time-resolution well in the femtosecond range. Within steps smaller than 400 fs significant changes in the data are visible. This temporal resolution is in good agreement with an electron pulse duration calculated using the GPT-code [78]. The simulations (fig. 5.5) show that in the current experimental system an electron pulse duration of about 150 fs can be reached by using single-electron pulses even applying a moderate acceleration field of only 4 kV/mm.

Formula 5.1 and the simulations (see fig. 5.5) show that by increasing the acceleration voltage and using single electron-pulses in the present system experiments with 100 fs electron pulses are possible.

Ongoing experiments aim at decreasing the pulse duration to the few femtosecond regime. Tuning the laser wavelength precisely to the cathode work function can reduce the initial energy spread of the photoemitted electrons [106]. By introducing a radio frequency cavity [102, 138] it is possible to compress the electron pulses further (“temporal lens”). In this approach jitter problems between the laser oscillator and the radio frequency cavity become severe [103] and limit the achievable time-resolution. However, synchronizing two oscillators better than 10 fs has been demonstrated [139].

6. Conclusions and outlook

Electron diffraction is a very powerful technique for the determination of the structures of various systems ranging from isolated molecules to solids. Due to their short de Broglie wavelength electrons allow investigation of physical systems with atomic resolution. Advanced to a time-resolved pump-probe method, namely UED, this atomic spatial resolution can be combined with ultrahigh time-resolution. In the gas phase experiments have been performed with picosecond resolution [9], while in solid-state experiments already femtosecond resolution has been demonstrated [90, 21]. Electron pulses offer yet another attractive possibility. Due to their charge they can respond very sensitively to electric and magnetic fields. This allows for the real-time investigation of electric and magnetic fields in OFI-plasmas [26] or to visualize photoemission process [30] using the method of electron deflectometry.

In the course of this thesis three experiments using picosecond and femtosecond electron pulses have been presented. The first set of experiments uses the method of electron deflectometry to investigate OFI-plasmas in gas jets and low-density OFI-plasmas. Deflectometry is a new method of imaging OFI-plasmas with picosecond temporal resolution. New features of OFI-plasma were observed using this method, such as a cloud of electrons separating from the plasma core far beyond the Debye length. Additionally, the effect of both electric and magnetic fields on the probe-electron beam has been investigated. The relevant physical quantities, such as the fields, number of charges and electron temperature, were calculated numerically. The sensitivity of subrelativistic electrons to relatively small fields makes this method applicable to the investigation of the dynamics of low density plasmas.

In the case of low density plasmas, a cloud of electrons expanding away from a positively charged plasma, with as much as 90% of the electrons escaping was observed (for a plasma density of $7 \times 10^{12} \text{ cm}^{-3}$). In contrast, in the high density

case for plasma densities of 10^{18} cm^{-3} only a small fraction (5×10^{-4}) of the electrons can escape the plasma. From the experiments a minimum electron escape energy of 3.4 eV was directly measured, and an electron temperature of 30 eV was obtained by comparing the experimental results with simulations.

In the second part, electron pulses were used as the probe-pulses in UED experiments. Pump-probe diffraction experiments were carried out, following the two-step dissociation reaction of $\text{C}_2\text{F}_4\text{I}_2$. The dissociation of the $\text{C}_2\text{F}_4\text{I}_2$ -molecules leads to transient selective alignment which could be clearly resolved in the diffraction patterns. The results demonstrate for the first time the feasibility of recording a UED pattern from transiently aligned molecules. The decay of the alignment was measured on a picosecond time scale. However, the limitation due to the picosecond-duration of the electron pulses becomes evident. Advanced to the femtosecond-regime, the electron pulses could probe the molecules while they are still close to the optimum alignment. In this case it would be possible to get access to three dimensional structure information. In addition to the bond-distances, the bond-angles could be retrieved [14]. The alignment could be further improved using active alignment techniques [100, 101]. Taking diffraction patterns corresponding to different projections of the molecule (using suitable algorithms [97]) will then allow full 3D measurement of the molecular structure. This method could also be applied to improve investigations of ultrafast molecular dynamics in a field-free environment. The experiments are a first important step on the route towards 3D imaging of complicated molecular structures with electron diffraction or possibly using the new generation of X-ray sources.

The duration of electron pulses used in chapter 4 was limited to the picosecond regime mainly by the mutual repulsion of the pulse electrons. To acquire diffraction patterns at kHz repetition rate thousands of electrons in each pulse are required. This limitation can be overcome by using single electron pulses at MHz repetition rate [20]. The last part of the thesis is dedicated to the development of a femtosecond electron diffraction apparatus based on this idea.

For single-electron pulses the main factor broadening the duration is the initial energy spread of the electrons in the moment of emission from the photocathode. According to eq. 5.1, for 0.1 electronvolt (as approximately expected for gold and 266 nm laser wavelength [105]) and the maximum demonstrated static acceleration field of 10 kV/mm [107], a duration below 100 fs is possible for single-electron

pulses. The initial energy spread can be reduced by tuning the laser wavelength to the bandgap of the photocathode [106].

To finally prove the short pulse duration a measurement method is required. Within the last part of the thesis, a new very general method is proposed and analyzed theoretically. A new ultrahigh-vacuum chamber was designed and constructed to allow for high static acceleration fields which are necessary to produce the shortest electron pulses. Using a MHz long-cavity laser system [25] first pump-probe experiments were carried out, which constitute a method to routinely establish the spatiotemporal overlap of electron and laser pulses even for the case of very low pulse energies (sub 100 nJ). Additionally, these experiments are a new method to visualize photoemission from a solid. Magnified by an expanding electron beam, a cloud of photoemitted electrons was observed. The pump-probe images show significant differences with time-steps of only 300 fs. This is in agreement with GPT-simulations of the electron pulse duration. Ongoing simulations address the underlying physical parameters.

In conclusion the experiments show the wide applicability of ultrashort electron pulses. The current limitation to the picosecond temporal regime in UED experiments using molecules in the gas phase can be overcome using single-electron pulses. To reduce the electron pulse duration further to the few femtosecond regime it has been proposed to compress the electron pulses by means of a radiofrequency cavity [102, 103].

In this approach the radio frequency cavity changes the electron energy inducing an appropriate “chirp” on the pulse to establish a temporal focus where the pulse duration is minimized. The main limitation to this approach is the jitter between the laser and the radio frequency cavity because after entering the RF-cavity the electron pulse is locked to the microwave oscillations rather than to the fs laser pulse [103]. However, synchronization of passively mode-locked laser oscillators to an RF-source has been demonstrated with a timing-jitter of less than 10 fs.

It has been proposed to generate even sub-femtosecond electron pulses by ponderomotive deflection and compression [140, 141, 142]. With such high time-resolution ultrafast electronic motion could be resolved in real-time with atomic resolution. Ultrafast electron diffraction combined with few femtosecond or even sub femtosecond time-resolution will be an ideal table-top tool to investigate various physical systems with atomic spatial resolution and the necessary temporal

resolution.

A. Chamber for MHz-experiments

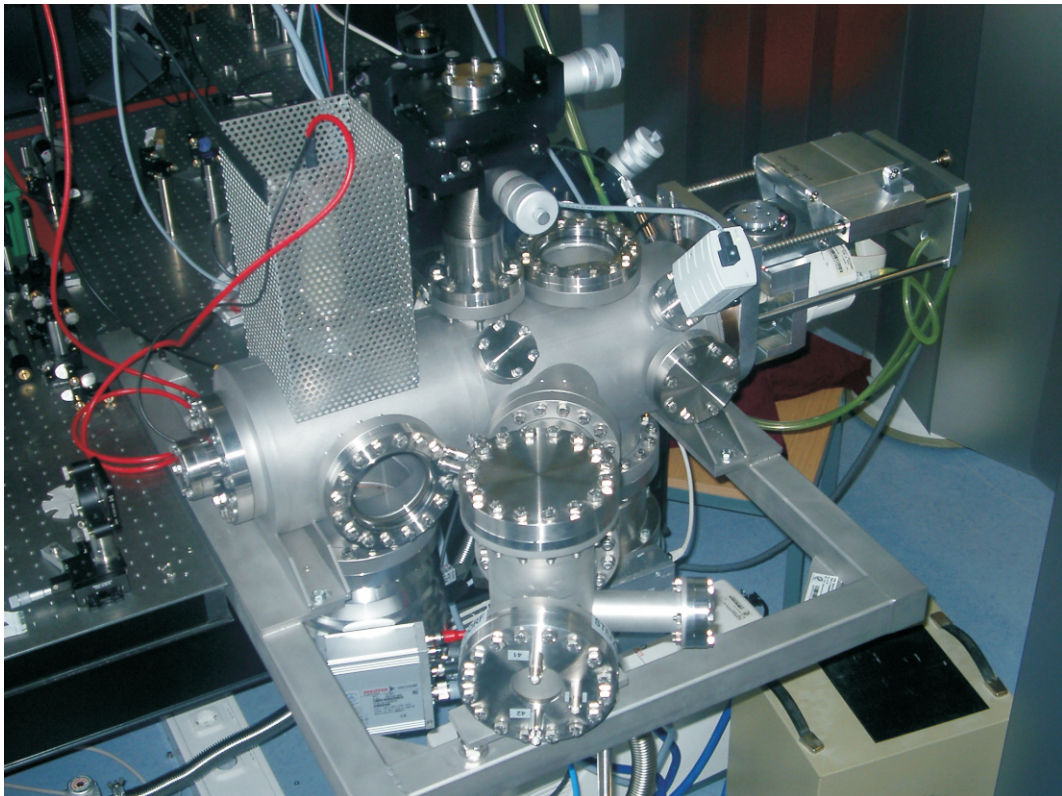
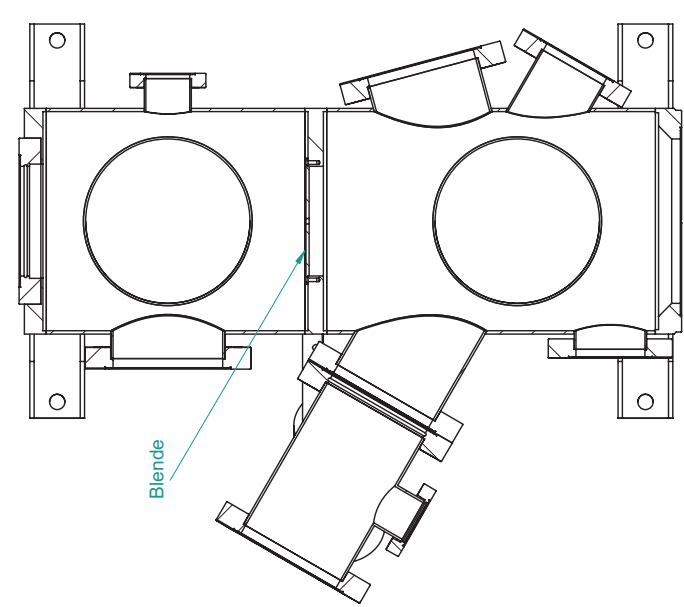
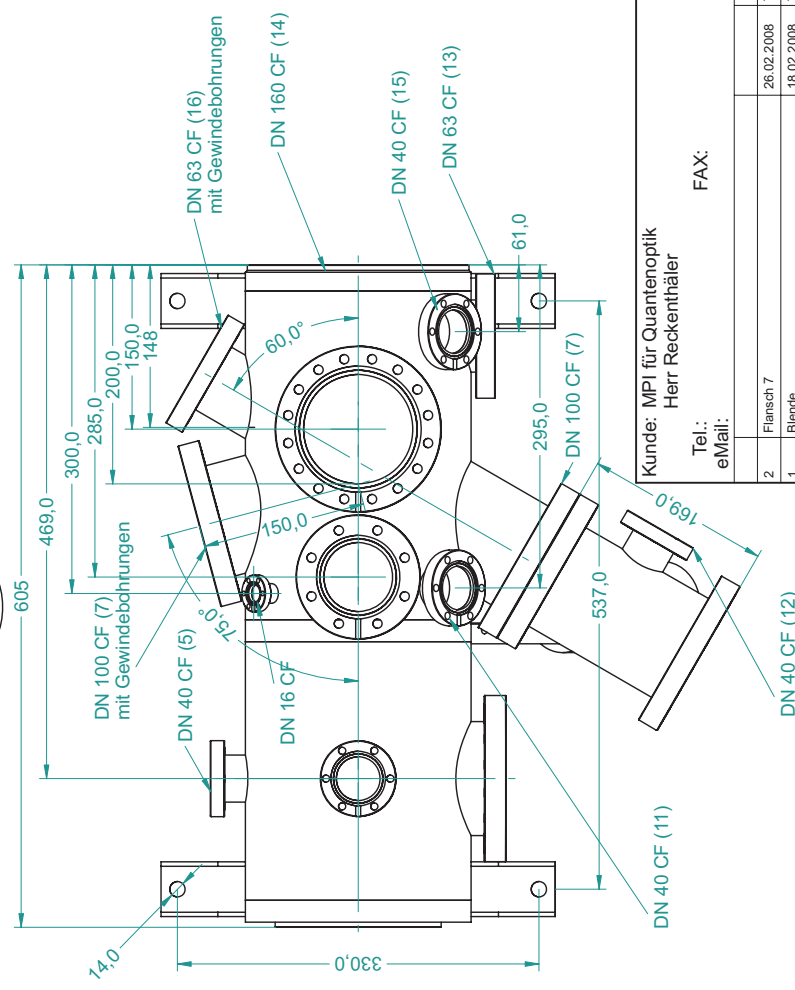
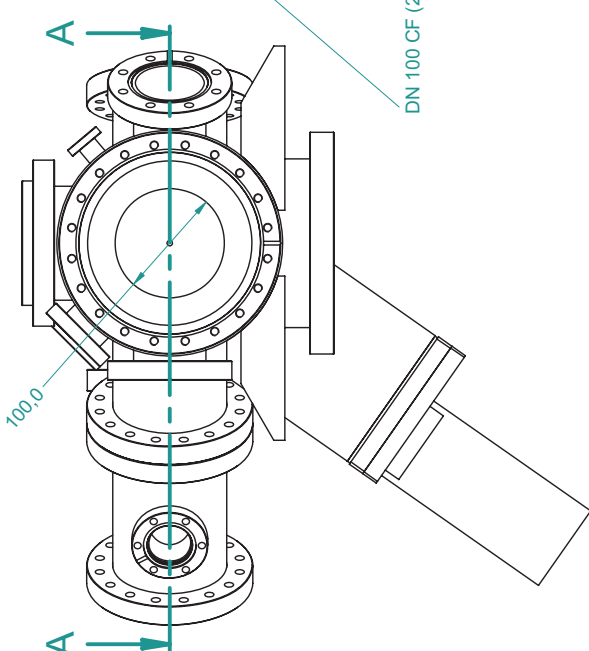
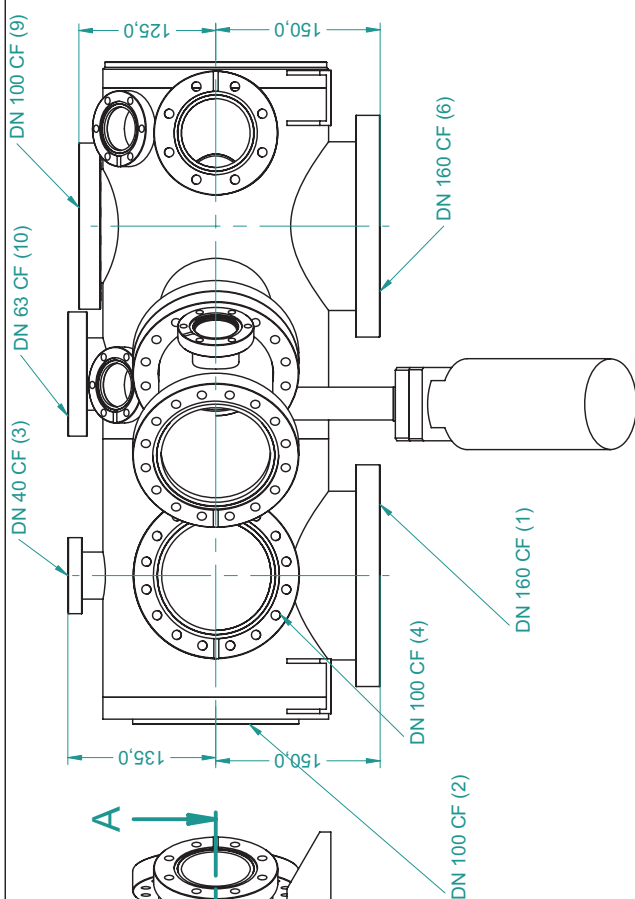
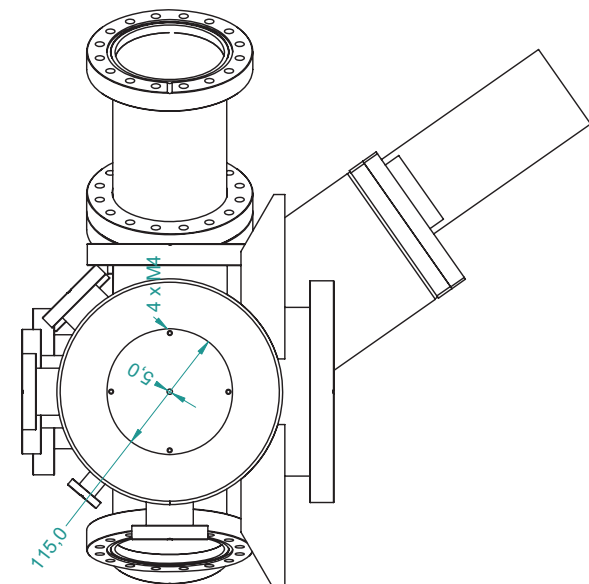


Figure A.1.: Photograph of the ultra-high vacuum chamber. On the backside a technical drawing of the UHV chamber is included which is printed with the kind permission of VAb Vakuum-Anlagenbau GmbH.



Schnitt A-A

Kunde: MPI für Quantenoptik Herr Reckenthaler		Maßstab: 1:5 in A2	Toleranzen nach DIN 2768 m
Tel.: eMail:		Material: Gewicht: 5373,9 kg	
FAX:		VAB	
2	Flansch 7	26.02.2008	To
1	Blende	18.02.2008	To
Nr.	Änderungen	Datum	Name
Genehmigung zum Druck in Doktorarbeit erteilt		geprüft	To
		bearbeitet	A.D.
		04.02.2008	To
		26.02.2008	A.D.
E:\CAD-Kunde\MPI Quantenoptik\Ventikammer\Ventikammer DN300.dft			
E:\CAD-Kunde\MPI Quantenoptik\Ventikammer\Ventikammer DN300.asm			

VAB
Vab Vakuum-Anlagenbau GmbH
 D-25337 Elmshorn - Marie-Curie-Str. Tel.: 04121 - 730 95
UHV-Kammer DN 200
 Ventikammer DN300.asm

B. Diffraction patterns

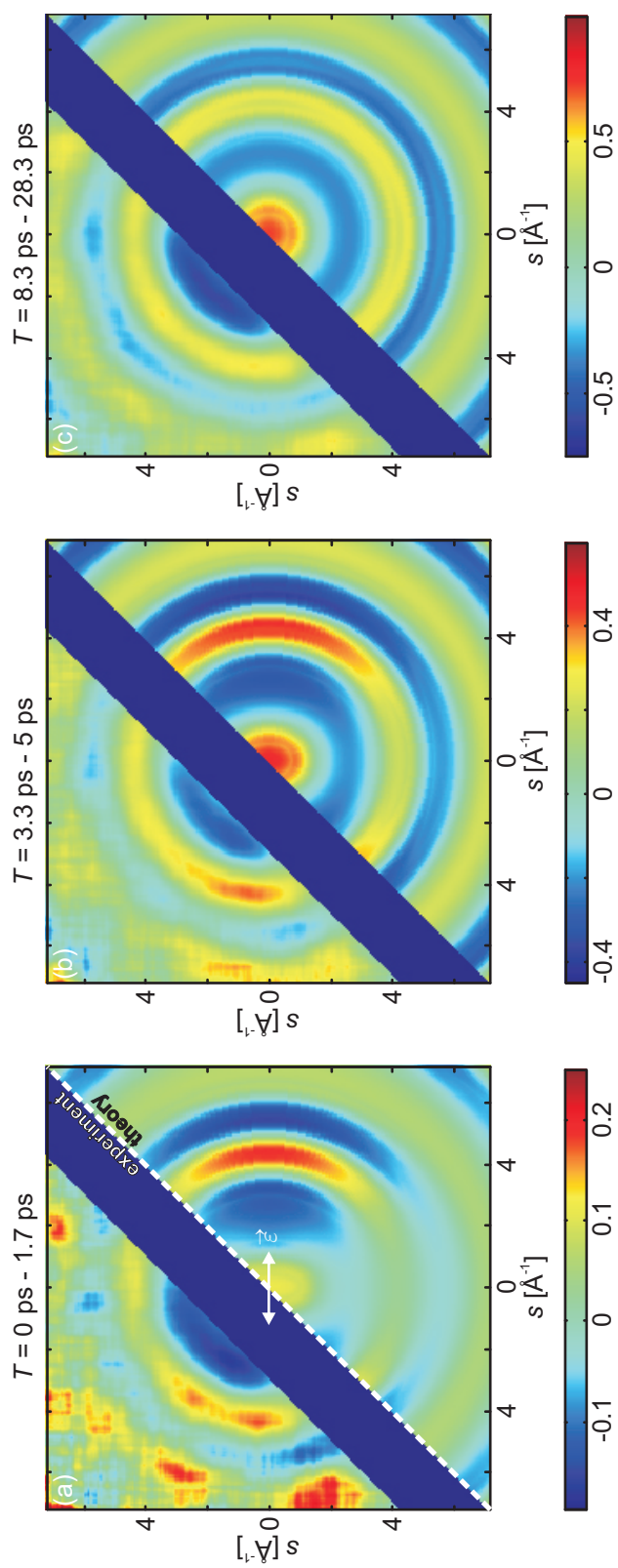


Figure B.1.: For the figure description see chapter 4.

Bibliography

- [1] F. Krausz and M. Ivanov. Attosecond physics. *Rev. Mod. Phys.*, **81** 163 (2009).
- [2] T. Brabec and F. Krausz. Intense few-cycle laser fields: Frontiers of nonlinear optics. *Rev. Mod. Phys.*, **72** 545 (2000).
- [3] A. Zewail. Femtochemistry: Atomic-scale dynamics of the chemical bond. *J. Phys. Chem. A*, **104** 5660 (2000).
- [4] E. Goulielmakis, M. Schultze, M. Hofstetter, V. S. Yakovlev, J. Gagnon, M. Uiberacker, A. L. Aquila, E. M. Gullikson, D. T. Attwood, R. Kienberger, F. Krausz, and U. Kleineberg. Single-cycle nonlinear optics. *Science*, **320** 1614 (2008).
- [5] M. Drescher, M. Hentschel, R. Kienberger, M. Uiberacker, V. Yakovlev, A. Scrinzi, T. Westerwalbesloh, U. Kleineberg, U. Heinzmann, and F. Krausz. Time-resolved atomic inner-shell spectroscopy. *Nature*, **419** 803 (2002).
- [6] A. L. Cavalieri, N. Mueller, T. Uphues, V. S. Yakovlev, A. Baltuska, B. Horvath, B. Schmidt, L. Bluemel, R. Holzwarth, S. Hendel, M. Drescher, U. Kleineberg, P. M. Echenique, R. Kienberger, F. Krausz, and U. Heinzmann. Attosecond spectroscopy in condensed matter. *Nature*, **449** 1029 (2007).
- [7] E. Goulielmakis, M. Uiberacker, R. Kienberger, A. Baltuska, V. Yakovlev, A. Scrinzi, T. Westerwalbesloh, U. Kleineberg, U. Heinzmann, M. Drescher, and F. Krausz. Direct measurement of light waves. *Science*, **305** 1267 (2004).

-
- [8] J. Itatani, J. Levesque, D. Zeidler, H. Niikura, H. Pepin, J. Kieffer, P. Corkum, and D. Villeneuve. Tomographic imaging of molecular orbitals. *Nature*, **432** 867 (2004).
- [9] A. H. Zewail. 4D ultrafast electron diffraction, crystallography, and microscopy. *Annu. Rev. Phys. Chem.*, **57** 65 (2006).
- [10] A. Almenningen, S. P. Arnesen, O. Bastiansen, H. M. Seip, and R. Seip. The effect of temperature variation on the amplitudes of vibration and shrinkage effects in carbon suboxide studied by gas electron diffraction. *Chem. Phys. Lett.*, **1** 569 (1968).
- [11] S. Hinchley, D. Wann, and D. Rankin. Structure by theory and experiment: one nationality, two languages. *International Journal of Quantum Chemistry*, **101** 32 (2005).
- [12] S. Hinchley, C. Morrison, D. Rankin, C. Macdonald, R. Wiacek, A. Cowley, M. Lappert, G. Gundersen, J. Clyburne, and P. Power. Persistent phosphinyl radicals from a bulky diphosphine: an example of a molecular jack-in-the-box. *Chem. Commun.*, **20** 2045 (2000).
- [13] J. Williamson and A. Zewail. Ultrafast electron-diffraction .4. Molecular-structures and coherent dynamics. *J. Phys. Chem.*, **98** 2766 (1994).
- [14] J. Baskin and A. Zewail. Ultrafast electron diffraction: Oriented molecular structures in space and time. *ChemPhysChem*, **6** 2261 (2005).
- [15] H. Stapelfeldt and T. Seideman. Colloquium: Aligning molecules with strong laser pulses. *Rev. Mod. Phys.*, **75** 543 (2003).
- [16] W. Fuss, T. Schikarski, W. Schmid, S. Trushin, P. Hering, and L. Kompa. Spectroscopy and ultrafast dynamics of the 2A(1) state of Z-hexatriene in gas phase. *J. Chem. Phys.*, **106** 2205 (1997).
- [17] F. Rosca-Pruna and M. Vrakking. Experimental observation of revival structures in picosecond laser-induced alignment of I-2. *Phys. Rev. Lett.*, **87** 153902 (2001).

-
- [18] P. Dooley, I. Litvinyuk, K. Lee, D. Rayner, M. Spanner, D. Villeneuve, and P. Corkum. Direct imaging of rotational wave-packet dynamics of diatomic molecules. *Phys. Rev. A*, **68** 023406 (2003).
- [19] J. Dwyer, C. Hebeisen, R. Ernstorfer, M. Harb, V. Deyirmenjian, R. Jordan, and R. Miller. Femtosecond electron diffraction: ‘making the molecular movie’. *Philos. Trans. R. Soc. A-Math. Phys. Eng. Sci.*, **364** 741 (2006).
- [20] V. Lobastov, R. Srinivasan, and A. Zewail. Four-dimensional ultrafast electron microscopy. *Proc. Natl. Acad. Sci. U. S. A.*, **102** 7069 (2005).
- [21] P. Baum, D.-S. Yang, and A. H. Zewail. 4D visualization of transitional structures in phase transformations by electron diffraction. *Science*, **318** 788 (2007).
- [22] R. Ernstorfer, M. Harb, C. T. Hebeisen, G. Sciaini, T. Dartigalongue, and R. J. D. Miller. The formation of warm dense matter: experimental evidence for electronic bond hardening in gold. *Science*, **323** 1033 (2009).
- [23] H. Ihee, V. Lobastov, U. Gomez, B. Goodson, R. Srinivasan, C. Ruan, and A. Zewail. Direct imaging of transient molecular structures with ultrafast diffraction. *Science*, **291** 458 (2001).
- [24] P. B. Corkum. Laser-generated plasmas - Probing plasma dynamics. *Nat. Photonics*, **2** 272 (2008).
- [25] S. Naumov, A. Fernandez, R. Graf, P. Dombi, F. Krausz, and A. Apolonski. Approaching the microjoule frontier with femtosecond laser oscillators. *New J. Phys.*, **7** (2005).
- [26] M. Centurion, P. Reckenthaeler, S. A. Trushin, F. Krausz, and E. E. Fill. Picosecond electron deflectometry of optical-field ionized plasmas. *Nat. Photon.*, **2** 315 (2008).
- [27] M. Centurion, P. Reckenthaeler, F. Krausz, and E. E. Fill. Picosecond imaging of low-density plasmas by electron deflectometry. *Opt. Lett.*, **34** 539 (2008).

- [28] P.Reckenthaeler, M. Centurion, W. Fuß, S. A. Trushin, F. Krausz, and E. E. Fill. Time-resolved electron diffraction from selectively aligned molecules. *Phys. Rev. Lett.*, **102** 213001 (2009).
- [29] P.Reckenthaeler, M. Centurion, V. S. Yakovlev, M. Lezius, F. Krausz, and E. E. Fill. Proposed method for measuring the duration of electron pulses by attosecond streaking. *Phys. Rev. A*, **77** 042902 (2008).
- [30] P.Reckenthaeler, M. Centurion, R. Graf, A. Apolonski, F. Krausz, and E. E. Fill. Time-resolved visualization of photoemission from a solid with ultrafast electron deflectometry. *in preparation* (2009).
- [31] M. Fink, R. D. Heuer, H. Kleinpoppen, K. P. Lieb, N. Risch, and P. Schmüser. *Bergmann Schaefer Lehrbuch der Experimentalphysik Band 4 – Bestandteile der Materie* (Walter de Gruyter & Co.KG , 2003).
- [32] K. Wuthrich. NMR - This other method for protein and nucleic-acid structure determination. *Acta Crystallogr. Sect. D-Biol. Crystallogr.*, **51** 249 (1995).
- [33] P. C. Lauterbu. Image formation by induced local interactions - Examples employing nuclear magnetic-resonance. *Nature*, **242** 190 (1973).
- [34] M. E. Raichle. A brief history of human brain mapping. *Trends Neurosci.*, **32** 118 (2009).
- [35] E. Riedle, H. Neusser, and E. Schlag. Electronic-spectra of polyatomic-molecules with resolved individual rotational transitions - benzene. *J. Chem. Phys.*, **75** 4231 (1981).
- [36] H. Barton and J. Bartlett. The positive ray analysis of water vapor ionized by impact of slow electrons. *Phys. Rev.*, **31** 0822 (1928).
- [37] J. Rehr and R. Albers. Theoretical approaches to x-ray absorption fine structure. *Rev. Mod. Phys.*, **72**, 3 621 (2000).
- [38] C. Bressler and M. Chergui. Ultrafast X-ray absorption spectroscopy. *Chem. Rev.*, **104** 1781 (2004).

- [39] R. Franklin and R. Gosling. Molecular configuration in sodium thymonucleate. *Nature*, **171** 740 (1953).
- [40] J. Watson and F. Crick. Molecular structure of nucleic acids - a structure for deoxyribose nucleic acid. *Nature*, **171** 737 (1953).
- [41] J. Kendrew, G. Bodo, H. Dintzis, R. Parrish, H. Wyckoff, and D. Phillips. 3-Dimensional model of the myoglobin molecule obtained by X-ray analysis. *Nature*, **181** 662 (1958).
- [42] M. Perutz, M. Rossmann, A. Cullis, H. Muirhead, G. Will, and A. North. Structure of haemoglobin - 3-dimensional fourier synthesis at 5.5-Å resolution, obtained by X-ray analysis. *Nature*, **185** 416 (1960).
- [43] H. Berman, T. Battistuz, T. Bhat, W. Bluhm, P. Bourne, K. Burkhardt, L. Iype, S. Jain, P. Fagan, J. Marvin, D. Padilla, V. Ravichandran, B. Schneider, N. Thanki, H. Weissig, J. Westbrook, and C. Zardecki. The protein data bank. *Acta Crystallogr. Sect. D-Biol. Crystallogr.*, **58** 899 (2002).
- [44] R. Henderson. The potential and limitations of neutrons, electrons and X-rays for atomic-resolution microscopy of unstained biological molecules. *Q. Rev. Biophys.*, **28** 171 (1995).
- [45] L. Schafer. Electron-diffraction as a tool of structural chemistry. *Appl. Spectrosc.*, **30** 123 (1976).
- [46] A. Zewail. Chemistry at the uncertainty limit. *Angew. Chem.-Int. Edit.*, **40** 4371 (2001).
- [47] M. Rosker, M. Dantus, and A. Zewail. Femtosecond clocking of the chemical bond. *Science*, **241** 1200 (1988).
- [48] A. Zewail. Laser femtochemistry. *Science*, **242** 1645 (1988).
- [49] M. Chergui and A. H. Zewail. Electron and X-ray methods of ultrafast structural dynamics: advances and applications. *ChemPhysChem*, **10** 28 (2009).
- [50] H. Ihee, B. Goodson, R. Srinivasan, V. Lobastov, and A. Zewail. Ultrafast electron diffraction and structural dynamics: Transient intermediates in the elimination reaction of C₂F₄I₂. *J. Phys. Chem. A*, **106** 4087 (2002).

- [51] R. Neutze, R. Wouts, D. van der Spoel, E. Weckert, and J. Hajdu. Potential for biomolecular imaging with femtosecond X-ray pulses. *Nature*, **406** 752 (2000).
- [52] G. Huldt, A. Szoke, and J. Hajdu. Diffraction imaging of single particles and biomolecules. *J. Struct. Biol.*, **144** 219 (2003).
- [53] T. Ditmire, J. Zweiback, V. P. Yanovsky, T. E. Cowan, G. Hays, and K. B. Wharton. Nuclear fusion from explosions of femtosecond laser-heated deuterium clusters. *Nature*, **398** 489 (1999).
- [54] S. D. Baton, J. J. Santos, F. Amiranoff, H. Popescu, L. Gremillet, M. Koenig, E. Martinolli, O. Guilbaud, C. Rousseaux, M. Rabec Le Gloahec, T. Hall, D. Batani, E. Perelli, F. Scianitti, and T. E. Cowan. Evidence of ultrashort electron bunches in laser-plasma interactions at relativistic intensities. *Phys. Rev. Lett.*, **91** 105001 (2003).
- [55] J. R. Davies, A. R. Bell, and M. Tatarakis. Magnetic focusing and trapping of high-intensity laser-generated fast electrons at the rear of solid targets. *Phys. Rev. E*, **59** 6032 (1999).
- [56] C. G. R. Geddes, C. Toth, J. van Tilborg, E. Esarey, C. B. Schroeder, D. Bruhwiler, C. Nieter, J. Cary, and W. P. Leemans. High-quality electron beams from a laser wakefield accelerator using plasma-channel guiding. *Nature*, **431** 538 (2004).
- [57] S. C. Wilks, W. L. Kruer, M. Tabak, and A. B. Langdon. Absorption of ultra-intense laser pulses. *Phys. Rev. Lett.*, **69** 1383 (1992).
- [58] T. Ditmire, J. W. G. Tisch, E. Springate, M. B. Mason, R. A. Hay, N. Smith, J. Marangos, and M. H. R. Hutchinson. High-energy ions produced in explosions of superheated atomic clusters. *Nature*, **386** 54 (1997).
- [59] M. S. Wei, S. P. D. Mangles, Z. Najmudin, B. Walton, A. Gopal, M. Tatarakis, A. E. Dangor, E. L. Clark, R. G. Evans, S. Fritzler, R. J. Clarke, C. Hernandez-Gomez, D. Neely, W. Mori, M. Tzoufras, and K. Krushelnick. Ion acceleration by collisionless shocks in high-intensity-laser–underdense-plasma interaction. *Phys. Rev. Lett.*, **93** 155003 (2004).

- [60] E. Fill, S. Borgström, J. Larsson, T. Starczewski, C. G. Wahlström, and S. Svanberg. XUV spectra of optical-field-ionized plasmas. *Phys. Rev. E*, **51** 6016 (1995).
- [61] A. McPherson, T. S. Luk, B. D. Thompson, K. Boyer, and C. K. Rhodes. Multiphoton-induced X-ray-emission and amplification from clusters. *Appl. Phys. B*, **57** 337 (1993).
- [62] P. Amendt, D. C. Eder, and S. C. Wilks. X-ray lasing by optical-field-induced ionization. *Phys. Rev. Lett.*, **66** 2589 (1991).
- [63] B. E. Lemoff, G. Y. Yin, C. L. Gordon III, C. P. J. Barty, and S. E. Harris. Demonstration of a 10-Hz femtosecond-pulse-driven XUV laser at 41.8 nm in Xe IX. *Phys. Rev. Lett.*, **74** 1574 (1995).
- [64] Y. Nagata, K. Midorikawa, S. Kubodera, M. Obara, H. Tashiro, and K. Toyoda. Soft-x-ray amplification of the Lyman-alpha transition by optical-field-induced ionization. *Phys. Rev. Lett.*, **71** 3774 (1993).
- [65] A. D. Bandrauk, S. Chelkowski, and H. S. Nguyen. Nonlinear photon processes in molecules at high intensities-route to XUV- attosecond pulse generation. *J. Mol. Structure*, **735** 203 (2005).
- [66] S. Augst, D. Strickland, D. D. Meyerhofer, S. L. Chin, and J. H. Eberly. Tunneling ionization of noble gases in a high-intensity laser field. *Phys. Rev. Lett.*, **63** 2212 (1989).
- [67] P. B. Corkum, N. H. Burnett, and F. Brunel. Above-threshold ionization in the long-wavelength limit. *Phys. Rev. Lett.*, **62** 1259 (1989).
- [68] J. Zweiback, T. Ditmire, and M. D. Perry. Femtosecond time-resolved studies of the dynamics of noble-gas cluster explosions. *Phys. Rev. A*, **59** R3166 (1999).
- [69] T. E. Glover, T. D. Donnelly, E. A. Lipman, A. Sullivan, and R. W. Falcone. Subpicosecond Thomson scattering measurements of optically ionized helium plasmas. *Phys. Rev. Lett.*, **73** 78 (1994).

- [70] S. Augst, D. D. Meyerhofer, D. Strickland, and S. L. Chint. Laser ionization of noble gases by Coulomb-barrier suppression. *J. Opt. Soc. Am. B*, **8** 858 (1991).
- [71] S. Tzortzakis, B. Prade, M. Franco, and A. Mysyrowicz. Time-evolution of the plasma channel at the trail of a self-guided IR femtosecond laser pulse in air. *Opt. Commun.*, **181** 123 (2000).
- [72] M. Centurion, Y. Pu, Z. Liu, D. Psaltis, and T. W. Hänsch. Holographic recording of laser-induced plasma. *Opt. Lett.*, **29** 772 (2004).
- [73] M. Dunne, T. Afshar-Rad, J. Edwards, A. J. MacKinnon, S. M. Viana, O. Willi, and G. Pert. Experimental observations of the expansion of an optical-field-induced ionization channel in a gas jet target. *Phys. Rev. Lett.*, **72** 1024 (1994).
- [74] L. J. Frasinski, K. Codling, P. Hatherly, J. Barr, I. N. Ross, and W. T. Toner. Femtosecond dynamics of multielectron dissociative ionization by use of a picosecond laser. *Phys. Rev. Lett.*, **58** 2424 (1987).
- [75] A. J. Mackinnon, P. K. Patel, R. P. Town, M. J. Edwards, T. Phillips, S. C. Lerner, D. W. Price, D. Hicks, M. H. Key, S. Hatchett, S. C. Wilks, M. Borghesi, L. Romagnani, S. Kar, T. Toncian, G. Pretzler, O. Willi, M. Koenig, E. Martinolli, S. Lepape, A. Benuzzi-Mounaix, P. Audebert, J. C. Gauthier, J. King, R. Snavely, R. R. Freeman, and T. Boehlly. Proton radiography as an electromagnetic field and density perturbation diagnostic (invited). *Rev. Scient. Instrum.*, **75** 3531 (2004).
- [76] C. K. Li, F. H. Seguin, J. A. Frenje, J. R. Rygg, R. D. Petrasso, R. P. J. Town, P. A. Amendt, S. P. Hatchett, O. L. Landen, A. J. Mackinnon, P. K. Patel, V. A. Smalyuk, T. C. Sangster, and J. P. Knauer. Measuring E and B fields in laser-produced plasmas with monoenergetic proton radiography. *Phys. Rev. Lett.*, **97** 135003 (2006).
- [77] A. J. Mackinnon, P. K. Patel, M. Borghesi, R. C. Clarke, R. R. Freeman, H. Habara, S. P. Hatchett, D. Hey, D. G. Hicks, S. Kar, M. H. Key, J. A. King, K. Lancaster, D. Neely, A. Nikkro, P. A. Norreys, M. M. Notley, T. W.

- Phillips, L. Romagnani, R. A. Snavely, R. B. Stephens, and R. P. J. Town. Proton radiography of a laser-driven implosion. *Phys. Rev. Lett.*, **97** 045001 (2006).
- [78] <http://www.pulsar.nl.net>.
- [79] P. B. Corkum. Plasma perspective on strong field multiphoton ionization. *Phys. Rev. Lett.*, **71** 1994 (1993).
- [80] P. B. Lerner and J. S. Cohen. Formation of hot electrons in noble gases by intense-field ionization: A quasistatic tunneling, independent-electron model. *Phys. Rev. A*, **51** 1464 (1995).
- [81] R. Barrachina and J. Macek. Theory of emission-angle-dependent auger transitions in ion atom collisions. *J. Phys. B-At. Mol. Opt. Phys.*, **22** 2151 (1989).
- [82] A. Tonomura. *Electron Holography* (Springer, Berlin, 1993).
- [83] E. Fill. Ultrashort-pulse laser plasmas: Fraction of hot electrons escaping from the target and electron spectra in planar and spherical geometry. *Phys. Plasmas*, **12** 052704 (2005).
- [84] C. Davisson and L. Germer. The scattering of electrons by a single crystal of nickel. *Nature*, **119** 558 (1927).
- [85] G. Thomson, N. Stuart, and C. Murison. The crystalline state of thin spluttered films of platinum. *Proc. Phys. Soc*, **45** 381 (1933).
- [86] H. N. Chapman, A. Barty, M. J. Bogan, S. Boutet, M. Frank, S. P. Hau-Riege, S. Marchesini, B. W. Woods, S. Bajt, H. Benner, R. A. London, E. Ploenjes, M. Kuhlmann, R. Treusch, S. Duesterer, T. Tschentscher, J. R. Schneider, E. Spiller, T. Moeller, C. Bostedt, M. Hoener, D. A. Shapiro, K. O. Hodgson, D. Van der Spoel, F. Burmeister, M. Bergh, C. Caleman, G. Huldt, M. M. Seibert, F. R. N. C. Maia, R. W. Lee, A. Szoeké, N. Timneanu, and J. Hajdu. Femtosecond diffractive imaging with a soft-X-ray free-electron laser. *Nat. Phys.*, **2** 839 (2006).

- [87] M. J. Bogan, W. H. Benner, S. Boutet, U. Rohner, M. Frank, A. Barty, M. M. Seibert, F. Maia, S. Marchesini, S. Bajt, B. Woods, V. Riot, S. P. Hau-Riege, M. Svenda, E. Marklund, E. Spiller, J. Hajdu, and H. N. Chapman. Single particle X-ray diffractive imaging. *Nano Lett.*, **8** 310 (2008).
- [88] J. Spence and R. Doak. Single molecule diffraction. *Phys. Rev. Lett.*, **92** (2004).
- [89] K. Hoshina, K. Yamanouchi, T. Ohshima, Y. Ose, and H. Todokoro. Alignment of CS₂ in intense nanosecond laser fields probed by pulsed gas electron diffraction. *J. Chem. Phys.*, **118** 6211 (2003).
- [90] B. Siwick, J. Dwyer, R. Jordan, and R. Miller. An atomic-level view of melting using femtosecond electron diffraction. *Science*, **302** 1382 (2003).
- [91] S. Nie, X. Wang, H. Park, R. Clinite, and J. Cao. Measurement of the electronic Gruneisen constant using femtosecond electron diffraction. *Phys. Rev. Lett.*, **96** (2006).
- [92] D. Zhong, S. Ahmad, and A. Zewail. Femtosecond elimination reaction dynamics. *J. Am. Chem. Soc.*, **119** 5978 (1997).
- [93] *International tables for crystallography*, volume C (Kluwer Academic Publishers, 2004), third edition.
- [94] D. Pullman, B. Friedrich, and D. Herschbach. Facile alignment of molecular rotation in supersonic beams. *J. Chem. Phys.*, **93** 3224 (1990).
- [95] H. Thomassen, S. Samdal, and K. Hedberg. Conformational-analysis. 15. 1,2-dibromotetrafluoroethane and 1,2-diiodotetrafluoroethane - electron-diffraction investigations of the molecular-structures, compositions, and anti-gauche energy and entropy differences. *J. Am. Chem. Soc.*, **114** 2810 (1992).
- [96] B. Widrow, J. Glover, J. Mccool, J. Kaunitz, C. Williams, R. Hearn, J. Zeidler, E. Dong, and R. Goodlin. Adaptive noise cancelling - principles and application . *Proc. IEEE*, **63** 1692 (1975).
- [97] J. Fienup. Phase retrieval algorithms - a comparison. *Appl. Optics*, **21** 2758 (1982).

-
- [98] D. Magde. Photoselection with intense laser-pulses. *J. Chem. Phys.*, **68** 3717 (1978).
- [99] L. Holmegaard, J. H. Nielsen, I. Nevo, H. Stapelfeldt, F. Filsinger, J. Kuepper, and G. Meijer. laser-induced alignment and orientation of quantum-state-selected large molecules. *Phys. Rev. Lett.*, **102** (2009).
- [100] K. F. Lee, D. M. Villeneuve, P. B. Corkum, A. Stolow, and J. G. Underwood. Field-free three-dimensional alignment of polyatomic molecules. *Phys. Rev. Lett.*, **97** (2006).
- [101] J. Larsen, K. Hald, N. Bjerre, H. Stapelfeldt, and T. Seideman. Three dimensional alignment of molecules using elliptically polarized laser fields. *Phys. Rev. Lett.*, **85** 2470 (2000).
- [102] E. Fill, L. Veisz, A. Apolonski, and F. Krausz. Sub-fs electron pulses for ultrafast electron diffraction. *New J. Phys.*, **8** 272 (2006).
- [103] L. Veisz, G. Kurkin, K. Chernov, V. Tarnetsky, A. Apolonski, F. Krausz, and E. Fill. Hybrid dc-ac electron gun for fs-electron pulse generation. *New J. Phys.*, **9** 451 (2007).
- [104] M. Schelev, R. MC, and A. Alcock. Image-converter streak camera with picosecond resolution. *Appl. Phys. Lett.*, **18** 354 (1971).
- [105] D. Wytrykus, M. Centurion, P. Reckenthaeler, F. Krausz, A. Apolonski, and E. Fill. Ultrashort pulse electron gun with a MHz repetition rate. *Appl. Phys. B-Lasers Opt.*, **96** 309 (2009).
- [106] M. Aidelsburger and P. Baum. *private communication*.
- [107] B. Siwick, J. Dwyer, R. Jordan, and R. Miller. Femtosecond electron diffraction studies of strongly driven structural phase transitions. *Chem. Phys.*, **299** 285 (2004).
- [108] T. Watanabe, M. Uesaka, J. Sugahara, T. Ueda, K. Yoshii, Y. Shibata, F. Sakai, S. Kondo, M. Kando, H. Kotaki, and K. Nakajima. Subpicosecond electron single-beam diagnostics by a coherent transition radiation in-

- terferometer and a streak camera. *Nucl. Instrum. Methods Phys. Res. Sect. A-Accel. Spectrom. Dect. Assoc. Equip.*, **437** 1 (1999).
- [109] H. Lihn, P. Kung, C. Settakorn, H. Wiedemann, and D. Bocek. Measurement of subpicosecond electron pulses. *Phys. Rev. E*, **53** 6413 (1996).
- [110] D. Wang, G. Krafft, and C. Sinclair. Measurement of femtosecond electron bunches using a RF zero-phasing method. *Phys. Rev. E*, **57** 2283 (1998).
- [111] J. van Tilborg, C. Schroeder, C. Filip, C. Toth, C. Geddes, G. Fubiani, E. Esarey, and W. Leemans. Terahertz radiation as a bunch diagnostic for laser-wakefield-accelerated electron bunches. *Phys. Plasmas*, **13** 056704 (2006).
- [112] I. Wilke, A. MacLeod, W. Gillespie, G. Berden, G. Knippels, and A. van der Meer. Single-shot electron-beam bunch length measurements. *Phys. Rev. Lett.*, **88** 124801 (2002).
- [113] C. T. Hebeisen, R. Ernstorfer, M. Harb, T. Dartigalongue, R. E. Jordan, and R. J. D. Miller. Femtosecond electron pulse characterization using laser ponderomotive scattering. *Opt. Lett.*, **31** 3517 (2006).
- [114] J. Itatani, F. Quere, G. Yudin, M. Ivanov, F. Krausz, and P. Corkum. Attosecond streak camera. *Phys. Rev. Lett.*, **88** 173903 (2002).
- [115] M. Kitzler, N. Milosevic, A. Scrinzi, F. Krausz, and T. Brabec. Quantum theory of attosecond XUV pulse measurement by laser dressed photoionization. *Phys. Rev. Lett.*, **88** 173904 (2002).
- [116] G. Sansone, E. Benedetti, F. Calegari, C. Vozzi, L. Avaldi, R. Flammini, L. Poletto, P. Villoresi, C. Altucci, R. Velotta, S. Stagira, S. De Silvestri, and M. Nisoli. Isolated single-cycle attosecond pulses. *Science*, **314** 443 (2006).
- [117] J. Schins, P. Breger, P. Agostini, R. Constantinescu, H. Muller, G. Grillon, A. Antonetti, and A. Mysyrowicz. Observation of laser-assisted Auger decay in argon. *Phys. Rev. Lett.*, **73** 2180 (1994).
- [118] O. Smirnova, V. Yakovlev, and A. Scrinzi. Quantum coherence in the time-resolved Auger measurement. *Phys. Rev. Lett.*, **91** 253001 (2003).

-
- [119] U. Fano. Effects of configuration interaction on intensities and phase shifts. *Phys. Rev.*, **124** 1866 (1961).
- [120] M. Krause. Atomic radiative and radiationless yields for K-Shells and L-Shells. *J. Phys. Chem. Ref. Data*, **8** 307 (1979).
- [121] D. B. Brown. *Handbook of spectroscopy*, volume I (CRC Press, Inc., Boca Baton, , 1979).
- [122] A. Zangwill. *Physics at surfaces* (Cambridge University Press, Cambridge, 1990).
- [123] J. H. Scofield. K-shell and L-shell ionization of atoms by relativistic electrons. *Phys. Rev. A*, **18** 963 (1978).
- [124] D. H. H. Hoffmann, C. Brendel, H. Genz, W. Löw, S. Müller, and A. Richter. Inner-shell ionization by relativistic electron-impact. *Z. Physik A*, **293** 18 (1979).
- [125] M. Aeschlimann, C. Schmuttenmaer, H. Elsayedali, R. Miller, J. Cao, Y. Gao, and D. Mantell. Observation of surface-enhanced multiphoton photoemission from metal-surfaces in the short-pulse limit. *J. Chem. Phys.*, **102** 8606 (1995).
- [126] B. Qian and H. Elsayed-Ali. Electron pulse broadening due to space charge effects in a photoelectron gun for electron diffraction and streak camera systems. *J. Appl. Phys.*, **91** 462 (2002).
- [127] B. Siwick, J. Dwyer, R. Jordan, and R. Miller. Ultrafast electron optics: Propagation dynamics of femtosecond electron packets. *J. Appl. Phys.*, **92** 1643 (2002).
- [128] S. Passlack, S. Mathias, O. Andreyev, D. Mittnacht, M. Aeschlimann, and M. Bauer. Space charge effects in photoemission with a low repetition, high intensity femtosecond laser source. *J. Appl. Phys.*, **100** (2006).
- [129] F. Banfi, C. Giannetti, G. Ferrini, G. Galimberti, S. Pagliara, D. Fausti, and F. Parmigiani. Experimental evidence of above-threshold photoemission in solids. *Phys. Rev. Lett.*, **94** 037601 (2005).

-
- [130] A. Apolonski, P. Dombi, G. Paulus, M. Kakehata, R. Holzwarth, T. Udem, C. Lemell, K. Torizuka, J. Burgdorfer, T. Hansch, and F. Krausz. Observation of light-phase-sensitive photoemission from a metal. *Phys. Rev. Lett.*, **92** 073902 (2004).
- [131] C. Lemell, X. Tong, F. Krausz, and J. Burgdorfer. Electron emission from metal surfaces by ultrashort pulses: Determination of the carrier-envelope phase. *Phys. Rev. Lett.*, **90** 076403 (2003).
- [132] S. Irvine, A. Dechant, and A. Elezzabi. Generation of 0.4-keV femtosecond electron pulses using impulsively excited surface plasmons. *Phys. Rev. Lett.*, **93** 184801 (2004).
- [133] S. Irvine, P. Dombi, G. Farkas, and A. Elezzabi. Influence of the carrier-envelope phase of few-cycle pulses on ponderomotive surface-plasmon electron acceleration. *Phys. Rev. Lett.*, **97** 146801 (2006).
- [134] M. Cinchetti, A. Gloskovskii, S. Nepjiko, G. Schonhense, H. Rochholz, and M. Kreiter. Photoemission electron microscopy as a tool for the investigation of optical near fields. *Phys. Rev. Lett.*, **95** 047601 (2005).
- [135] L. Miaja-Avila, C. Lei, M. Aeschlimann, J. Gland, M. Murnane, H. Kapteyn, and G. Saathoff. Laser-assisted photoelectric effect from surfaces. *Phys. Rev. Lett.*, **97** 113604 (2006).
- [136] L. Miaja-Avila, J. Yin, S. Backus, G. Saathoff, M. Aeschlimann, M. M. Murnane, and H. C. Kapteyn. Ultrafast studies of electronic processes at surfaces using the laser-assisted photoelectric effect with long-wavelength dressing light. *Phys. Rev. A*, **79** (2009).
- [137] L. Miaja-Avila, G. Saathoff, S. Mathias, J. Yin, C. La-o vorakiat, M. Bauer, M. Aeschlimann, M. Murnane, and H. Kapteyn. Direct measurement of core-level relaxation dynamics on a surface-adsorbate system. *Phys. Rev. Lett.*, **101** 046101 (2008).
- [138] M. Monastyrskiy, S. Andreev, D. Greenfield, G. Bryukhnevich, V. Tarasov, and M. Schelev. *High-speed photography and Photonics* (B. J. Thompson, 2005).

- [139] L. Ma, R. Shelton, H. Kapteyn, M. Murnane, and J. Ye. Sub-10-femtosecond active synchronization of two passively mode-locked Ti : sapphire oscillators. *Phys. Rev. A*, **64** 021802 (2001).
- [140] P. Baum and A. H. Zewail. Breaking resolution limits in ultrafast electron diffraction and microscopy. *Proc. Natl. Acad. Sci. U. S. A.*, **103** 16105 (2006).
- [141] P. Baum and A. H. Zewail. Attosecond electron pulses for 4D diffraction and microscopy. *Proc. Natl. Acad. Sci. U. S. A.*, **104** 18409 (2007).
- [142] P. Baum and A. H. Zewail. 4D attosecond imaging with free electrons: Diffraction methods and potential applications. *Chem. Phys.*, **in press** (2009).

Danksagung

An dieser Stelle möchte ich mich bei den Menschen bedanken, die mich während der Zeit meiner Doktorarbeit unterstützt haben.

An erster Stelle möchte ich mich bei meinem Doktorvater Herrn Prof. Dr. Ferenc Krausz für sein Vertrauen bedanken, mich in seine Arbeitsgruppe aufzunehmen und mir eine Arbeit in einem hochspannenden Gebiet zu ermöglichen. Sein unerschütterlicher Enthusiasmus ist mir eine stetige Motivation.

Mein ganz besonderer Dank gilt meinem Betreuer Herrn Dr. Ernst Fill. Mit seinem unerschöpflichen Wissen hat er mich jederzeit unterstützt und mir geholfen die Experimente kontinuierlich weiterzubringen. Ganz besonders möchte ich mich auch bei meinem Kollegen Herrn Dr. Martin Centurion bedanken, mit dem ich alle Experimente gemeinschaftlich durchgeführt habe. Seine experimentellen Fähigkeiten und sein physikalisches Wissen haben mich stets motiviert. Gerne denke ich an die gemeinsamen Mittagessen mit Dr. Fill und Martin zurück, in denen die wesentlichen Ideen dieser Experimente entstanden sind.

Bei Herrn Prof. Dr. Eberhard Riedle möchte ich mich für die freundliche Übernahme des Koreferats meiner Doktorarbeit bedanken.

Bei Herrn Prof. Dr. Karl-Ludwig Kompa bedanke ich mich für die Erlaubnis, die Experimente zu den OFI-Plasmen und zur zeitaufgelösten Elektronenbeugung in einem seiner Labors durchführen zu dürfen. Ich bedanke mich besonders für die Unterstützung von Herrn Dr. Sergei Trushin, der uns jederzeit geholfen hat, den Laser zu bedienen. Mit Freude denke ich an die zahlreichen Gespräche über Themen der Physik und Chemie mit Herrn Dr. Werner Fuß und Herrn Dr. Hartmut Schröder.

Die Experimente mit der MHz-Elektronenquelle haben im Physikdepartment der LMU in der Gruppe von Herrn Dr. Alexander Apolonskiy stattgefunden. Ich be-

danke mich bei Dr. Apolonskiy für die stetige Unterstützung, die er mir während dieser Zeit hat zukommen lassen. Es hat viel Spaß gemacht, in seiner Gruppe zu arbeiten. Ich möchte mich herzlich bei Herrn Dr. Volodymyr Pervak bedanken. Die von ihm beschichteten Goldkathoden haben die Experimente erst möglich gemacht. Bei Frau Roswitha Graf bedanke ich mich für Ihre stetige und kompetente Unterstützung mit dem MHz-Lasersystem. Besonders möchte ich mich auch bei Herrn Dr. Peter Baum bedanken der meine Sicht der Physik mit immer neuen Aspekten bereichert. Bei Herrn Friedrich Kirchner und Herrn Thomas Ganz bedanke ich mich für die zahlreichen Gespräche über die Physik und das Lesen meiner Arbeit. Bei der ganzen Gruppe an der LMU möchte ich mich für die tolle Atmosphäre bedanken.

Bei Herrn Dr. Vladislav Yakovlev bedanke ich mich herzlich für den quantenmechanischen Teil der Rechnungen zum vorgeschlagenen Experiment zur Elektronenpulsdauer. Bei den Gesprächen über dieses Thema konnte ich sehr viel lernen.

Die Experimente sind tatkräftig durch die kompetenten Techniker des MPQ und der LMU unterstützt worden. Ich möchte mich besonders bei Herrn Walter Ritt für seine unermüdliche Unterstützung bei den Experimenten am MPQ bedanken. Auch gilt mein Dank Herrn Alois Böswald, Herrn Manfred Fischer, Herrn Harald Haas, Herrn Hans Peter Schönauer und Herrn Axel Raufer am MPQ sowie Herrn Siegfried Herbst an der LMU für ihre stetige Hilfe mit Rat und Tat. Die hervorragende Arbeit der Werkstätten des MPQ und der LMU haben dazu beigetragen, die Experimente schnell und mit hoher Qualität durchzuführen. Dafür möchte ich mich besonders bedanken.

Während der Zeit meiner Arbeit bin ich von der “International Max-Planck Research School of Advanced Photon Science” unterstützt worden. Mein besonderer Dank gilt Herrn Dr. Tobias Schätz, Herrn Dr. Matthias Kling und Frau Monika Wild. Ich denke gerne an die gemeinschaftlichen Aktivitäten im Rahmen dieses Programms zurück.

Von ganzem Herzen danke ich meinen Eltern. Sie haben mich mein Leben lang mit Geduld und Liebe unterstützt und gefördert.

Curriculum Vitae

Geburtsdatum 20.04.1980

Geburtsort Trier

Staatsangehörigkeit Deutsch

Adresse Aberlestrasse 43
81371 München

Email p.reckenthaeler@gmx.de



Ausbildung

Seit September 2006 Doktorarbeit

International Max Planck Research School on Advanced Photon Science
Max-Planck-Institut für Quantenoptik, Garching bei München
Ludwig-Maximilians-Universität, München

Doktorvater: Prof. Dr. Ferenc Krausz, Direktor des Max-Planck-Instituts für
Quantenoptik, Garching bei München, Lehrstuhl für Physik an der Ludwig-
Maximilians-Universität, München

Titel: Electron Pulses probing Plasma Dynamics and aligned Molecules

Juli 2006 Diplom in Physik

August 2005 - Juli 2006 Diplomarbeit in Physik

Rheinische Friedrich-Wilhelms-Universität, Bonn

Heinrich-Hertz-Stiftungslehrstuhl der Deutschen Telekom AG

Betreuer der Diplomarbeit: Prof. Dr. Karsten Buse, Inhaber des Heinrich-Hertz-Stiftungslehrstuhles der Deutschen Telekom AG

Titel: Ultraschnelle Absorptionsprozesse in Lithiumniobat-Kristallen

September 2000 - Juli 2005 Studium der Physik

Rheinische Friedrich-Wilhelms-Universität, Bonn

September 2002 - Juli 2003 Studium der Physik (Erasmusstipendium)

Universidad Autónoma de Madrid, Madrid, Spanien

Juli 1999 - Juni 2000 Zivildienst

Caritasverband für die Region Trier e.V., Sozialstation am Dom, Trier

Juni 1999 Abitur

Friedrich-Wilhelm-Gymnasium, Trier

Auszeichnungen

2006 Promotionsstipendium der Max-Planck-Gesellschaft im Rahmen der International Max Planck Research School on Advanced Photon Sciences**1999** Auszeichnung der Dr. Rudolf-Centner-Stiftung für die Facharbeit im Fach Physik während der Oberstufenzeit des Gymnasiums

Lehrtätigkeiten während des Studiums

WiSe 2005/2006 Tutor, Experimentalphysik I,

Rheinische Friedrich-Wilhelms-Universität, Bonn

SoSe 2005 Tutor, Experimentalphysik II,

Rheinische Friedrich-Wilhelms-Universität, Bonn

WiSe 2004/2005 Tutor, Theoretische Physik III (Fortgeschrittene Quantenmechanik), Rheinische Friedrich-Wilhelms-Universität, Bonn

WiSe 2003/2004 Tutor, Theoretische Physik I (Theoretische Mechanik), Rheinische Friedrich-Wilhelms-Universität, Bonn

Sonstige Tätigkeiten während des Studiums

Februar 2004 - Juli 2004 Studentische Hilfskraft, Max-Planck-Institut für Radioastronomie, Bonn (“Infrared Interferometry and Image Processing”)

September 2004 Sommerpraktikum am Heinrich Hertz-Stiftungslehrstuhl der Deutschen Telekom AG, Universität Bonn (“Herstellung optischer Wellenleiter in photoadressierbaren Polymeren durch Beleuchtung mit weißem Licht”)

Wissenschaftliche Veröffentlichungen

- P. Reckenthaeler, M. Centurion, A. Apolonski, F. Krausz, and E. E. Fill. Time-resolved visualization of photoemission from a solid with ultrafast electron deflectometry. *in preparation*
- D. Wytrykus, M. Centurion, P. Reckenthaeler, F. Krausz, A. Apolonski, and E. Fill. Ultrashort pulse electron gun with a MHz repetition rate. *Appl. Phys. B-Lasers Opt.*, **96**, 309 (2009).
- P. Reckenthaeler, M. Centurion, W. Fuß, S. A. Trushin, F. Krausz, and E. E. Fill. Time-Resolved Electron Diffraction from Selectively Aligned Molecules. *Phys. Rev. Lett.*, **102**, 213001 (2009).
- M. Centurion, P. Reckenthaeler, F. Krausz, and E. E. Fill. Picosecond imaging of low-density plasmas by electron deflectometry. *Opt. Lett.*, **34**, 539 (2009).
- D. Maxein, S. Kratz, P. Reckenthaeler, J. Bueckers, D. Haertle, Th. Woike, and K. Buse. Polarons in magnesium-doped lithium niobate crystals induced by femtosecond light pulses. *Appl. Phys. B-Lasers Opt.*, **92**, 543 (2008).

- M. Centurion, P. Reckenthaeler, S. A. Trushin, F. Krausz, and E. E. Fill. Picosecond electron deflectometry of optical-field ionized plasmas. *Nat. Photonics*, **2**, 315 (2008).
- P. Reckenthaeler, M. Centurion, V. S. Yakovlev, M. Lezius F. Krausz, and E. E. Fill. Proposed method for measuring the duration of electron pulses by attosecond streaking. *Phys. Rev. A*, **77**, 042902 (2008).
- P. Reckenthaeler, D. Maxein, Th. Woike, K. Buse, and B. Sturman. Separation of optical Kerr and free-carrier nonlinear responses with femtosecond light pulses in LiNbO₃ crystals. *Phys. Rev. B* **76**, 195117 (2007).

Konferenzbeiträge

- Fachvortrag: P. Reckenthäler, M. Centurion, W. Fuß, A. Apolonski, F. Krausz und E. Fill. “Pikosekunden-Elektronenbeugung von selektiv ausgerichteten Molekülen”, Tagung der Deutschen Physikalischen Gesellschaft, Hamburg, 2.-6. März, 2009.
- P. Reckenthaeler, M. Centurion, V.S. Yakovlev, M. Lezius, F. Krausz and E.E. Fill, “Measurement of Electron Pulse Duration by Attosecond Streaking”, Poster und Proceedings, UP 2008, International Conference on Ultrafast Phenomena, Stresa, Italien, 9.-13. Juni 2008.
- P. Reckenthaeler, M. Centurion, W. Fuß, F. Krausz, A. Apolonski and E.E. Fill, “Time Resolved Electron Diffraction From Aligned Molecules”, Structural Dynamics: Methods And Applications, Poster, Sommerschule der European Science Foundation, Vilamoura, Portugal, 5.-8. Juni 2008.
- P. Reckenthaeler, M. Centurion, E. Fill, L. Veisz, S. Trushin, A. Apolonski, S. Naumov and F. Krausz, “Femtosecond Electron Diffraction”, Poster, DPG Physics School 2007 : Attosecond Physics, Bad Honnef, 20.-25. Mai, 2007.
- M. Centurion, P. Reckenthaeler, E. Fill, L. Veisz, S. Trushin, A. Apolonski, S. Naumov, F. Krausz, “Femtosecond Electron Diffraction”, VI. Research Course on New X-Ray Sciences, X-Ray Investigation of Ultrafast Processes, Poster, DESY, Hamburg, 27. Februar - 2. März, 2007.

-
- P. Reckenthäler, D. Maxein, O. Beyer, B. Sturman, and K. Buse. “Holographic Investigation of Lithium Niobate Crystals with Femtosecond Laser Pulses”, Tagung der Deutschen Physikalischen Gesellschaft, Dresden, 27-31 März, 2005.